

UNIVERSITÀ DEGLI STUDI DI SALERNO

DIPARTIMENTO DI MATEMATICA



Dottorato in Matematica, Fisica e applicazioni

XXXV Ciclo

Curriculum: Fisica

Advanced Modeling of Microlensing Events

Supervisor:

Prof.

Valerio Bozza



Coordinatore:

Prof.ssa

Patrizia Longobardi



Candidato:

Paolo Rota

Mat. 8800200060



ANNO ACCADEMICO 2021/2022

*Alla mia famiglia,
ad Ylenia,
ai miei amici più cari,
al Centro Astronomico Neil Armstrong*

CONTENTS

1	An introduction to microlensing	7
1.1	Gravitational microlensing: a brief history	7
1.2	The basics of gravitational microlensing	9
1.2.1	Magnification	12
1.2.2	Paczynski's curve	15
1.2.3	Optical Depth and Event Rate	15
1.2.4	Finite source effects	16
1.3	The binary lens	18
1.3.1	Binary lens: planetary configuration	20
1.4	High order effects	21
1.4.1	Parallax	21
1.4.2	Orbital motion	24
1.4.3	Binary source	26
1.4.4	Xallarap	26
1.5	Degeneracies in microlensing	27
1.6	Why is microlensing important?	29
2	Modelling a microlensing event	33
2.1	Observations	33
2.1.1	OGLE	34

CONTENTS

2.1.2	MOA	35
2.1.3	KMTNet	36
2.1.4	Satellite microlensing	37
2.1.5	High resolution imaging: Hubble and Keck	41
2.1.6	Follow-up	42
2.2	Lightcurve computation	44
2.2.1	Inverse Ray Shooting	44
2.2.2	Contour Integration	45
2.3	Modelling	46
2.3.1	VBBinaryLensing	46
2.3.2	RTModel	50
2.3.3	Levenberg-Marquardt algorithm	50
2.3.4	Markov Chain	53
3	Xallarap as contaminant in planetary microlensing: the case of MOA-2006-BLG-074	56
3.1	Motivations	56
3.2	Observations	58
3.3	Modeling	59
3.4	Source Analysis	66
3.5	Physical Constraints	68
3.5.1	Constraint on the $2LO$ model	69
3.5.2	Constraints on 1L2SX model	70
3.6	Discussion	72
4	Precision measurement of a brown dwarf mass in a binary system: the case of OGLE-2019-BLG-0033	74
4.1	Motivations	74
4.2	Observations	76
4.3	Modeling	78
4.3.1	Detailed modeling procedure	79
4.4	Source analysis	86

CONTENTS

4.5	Lens system properties	90
4.5.1	Mass and distance	90
4.5.2	Orbital motion	91
4.5.3	Lens kinematics	92
4.6	Discussion	93
5	Microlensing in the Gaia era: Gaia20bof and Gaia21blx	97
5.1	Gaia20bof	98
5.1.1	Observations	98
5.1.2	Modeling	98
5.1.3	Source analysis	100
5.1.4	Constraint on the lens and discussion	102
5.2	Gaia21blx	105
5.2.1	Observations	105
5.2.2	Modeling	105
5.2.3	Constraint on the lens and discussion	107
6	Conclusions	113
	References	115
	List of Tables	141
	List of Figures	148

ABSTRACT

The search for exoplanets is one of the most exciting challenges. From the first exoplanets discovered around the pulsar PSR B1 257+12 back in 1992 until today there are over 5200 exoplanets discovered. And the number will continue to rise in the coming years with the advent of the latest generation telescopes. There are various techniques for finding exoplanets such as transit, radial velocity, pulsar timing, direct imaging etc. But among these, gravitational microlensing is one of the most fascinating. Gravitational microlensing is a particular technique to detect exoplanets otherwise unavailable with other techniques such as transits or radial velocity. We have a microlensing event when the light from a distant source is deflected by a lens passing through the source and the observer. The result, in the simplest case, is a bell-shaped peak in the light curve. Planets can be detected studying the anomalies in the lightcurve (additional peaks or dips, longer distortions, etc.). But microlensing is not important only for exoplanets. The fact that with this technique it is possible to reach distances of the order of the galactic center allows us to discover objects ranging from the disk to the bulge allowing us to have a much more complete overview of the study of the stellar populations of our galaxy. And in particular with the study of binary systems we can detect faint objects that are impossible to reveal with other techniques, such as brown dwarfs, mysterious objects of which little is known yet and which are presumed to

CONTENTS

populate our galaxy in great abundance. Microlensing is undoubtedly the best method to discover these objects, since having extremely low luminosities they are difficult to see with telescopes except when they play the role of lens. Moreover, in some cases the orbital motions of the system can also be detected, allowing us to study their dynamics in more detail. The typology of microlensing events is enormous and in this thesis we will analyze some of the cases that can occur. In the first part we focus on the fundamental concepts of microlensing theory for the exoplanets search. The second part is dedicated to the modeling of microlensing events, which is based on the `VBinaryLensing` code. In the third part we analyze some microlensing events, each with certain characteristics, to highlight how vast the case history of these events is. Finally there will be the conclusions where the results achieved and future prospects are discussed.

CHAPTER 1

AN INTRODUCTION TO MICROLENSING

1.1 Gravitational microlensing: a brief history

Even before the formulation of the theory of relativity, the concept of curvature of light was in vogue. Newton himself in 1704 assumed that light was deflected in the presence of a gravitational field. In 1801 Soldner tried to calculate the deflection of light with the Newtonian mechanics, obtaining half the relativistic result. We have to wait until 1915 when Einstein, thanks to the theory of general relativity he elaborated, calculated the angle of deflection. The theory of relativity was then confirmed by Dyson and Eddington in 1919 when, during a solar eclipse which took place in South Africa, they managed to measure the angle of deflection caused by the Sun against a star which was behind it. This theory was applied to the study of distant galaxies: in 1937 Zwicky assumed that galaxies can be gravitational lenses that can act on other more distant galaxies: in this way it was possible to obtain distance and mass of the lens. The first proof of this assumption occurred in 1979 when Walsh, Carswell and Weymann found the first gravitational lens in doubly imaged

1. AN INTRODUCTION TO MICROLENSING

quasar (see Figure 1.1).

The origin of the term microlensing derives from the description of those

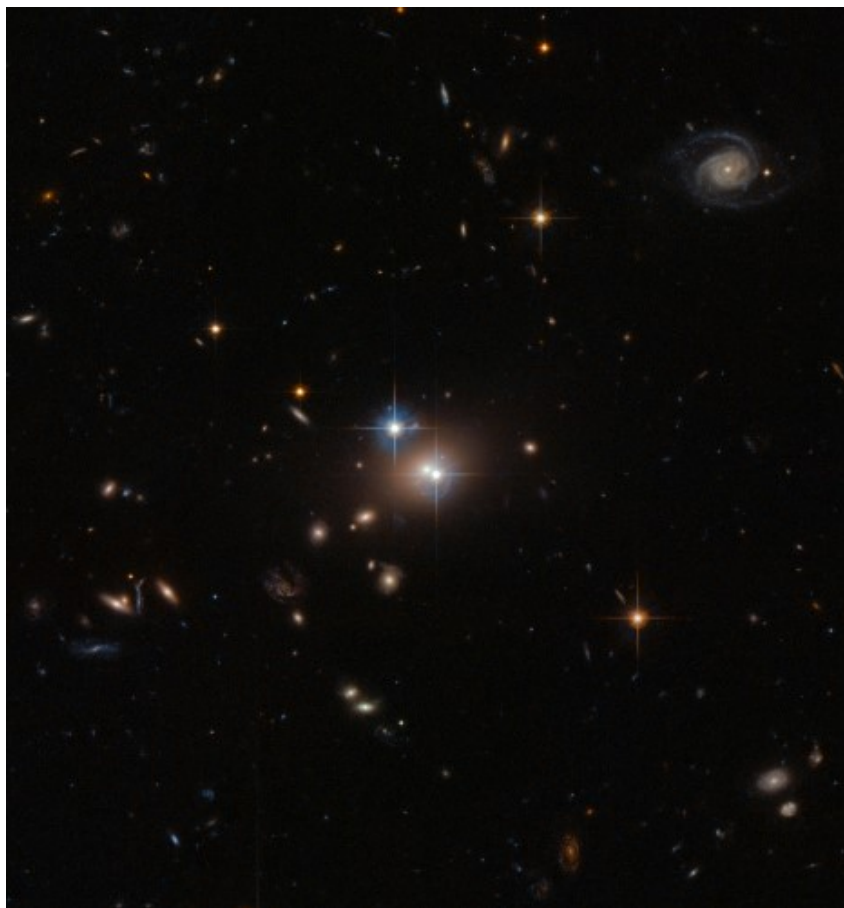


Figure 1.1: Image of the lensed quasar 0957 +561. The Twin Quasar, as renamed later, was the first proof of gravitational lensing applied to distant galaxies. The lens is the galaxy YGKOW G1 with a distance of 4 billion light-years from Earth. The quasar is distant 9 billion light-years. Credit image: ESA/Hubble & NASA

gravitational lensing phenomena where it was not possible to distinguish the images distinctly. What was observed was only a variation in the total flux. In 1986 Paczynski proposed the existence of compact objects made by dark matter surrounding the Milky Way would lead to microlensing of the stars in the Magellanic Cloud [1]. The observation of these objects would have shown that the existence of the massive astrophysical compact halo objects

1. AN INTRODUCTION TO MICROLENSING

(MACHOs), which also includes stellar remnants and brown dwarfs, was in too small quantities to account for the motion of stars in orbit within galaxies. The results confirmed this hypothesis ([2], [3], [4]). In 1991 Mao and Paczynski [5] demonstrated that with microlensing it was possible to detect the binary companions of stars and the following year Gould and Loeb demonstrated that exoplanets could also be detected with this technique [6].

Up to now more than 150 exoplanets have been detected with the microlensing, which is very sensitive to planets beyond the snow line, i. e. the location in the protoplanetary disk where the disk midplane temperature is below the sublimation temperature of water [7].

1.2 The basics of gravitational microlensing

A gravitational microlensing event appears when the light of a distant star (called source) is perturbed by the gravitational field of a foreground star (called lens), when it is between the source and the observer (see Figure 1.2). According to General Relativity the angle of deflection is:

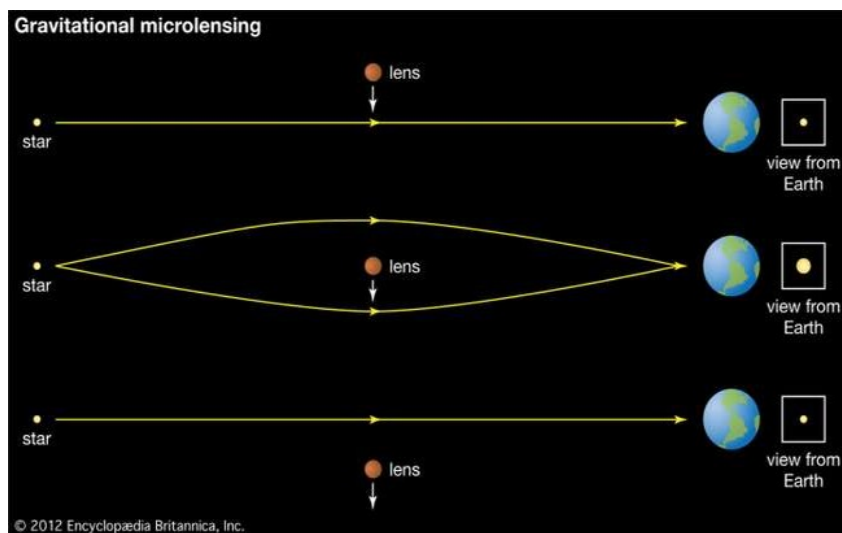


Figure 1.2: Picture of a gravitational microlensing event with a distant source (the star) whose signal directed to an observer (the Earth) is amplified by a lens. Credit image: Enciclopedia Britannica, Inc

1. AN INTRODUCTION TO MICROLENSING

$$\hat{\alpha} = \frac{4GM}{c^2 r_0} \quad (1.1)$$

where G is the gravitational constant, c is the speed of light and r_0 is the closest approach distance. The result is the creation of multiple images that we are not able to distinguish; what we observe is an increase in the flux of the source. The planetary companion can be detected if there are additional perturbation to the source flux.

Let us analyze this phenomenon in more detail. Consider a lens of mass M located at a distance D_L from an observer O and a distant D_S source. When the lens passes between the source and the observer there is the creation of two images that change their brightness and positions as the source moves. If source, lens and observer are perfectly aligned there is the formation of a circular ring called Einstein Ring, whose angular radius is [7]:

$$\theta_E = \sqrt{\frac{4GM}{c^2} \frac{(D_S - D_L)}{D_S D_L}} \quad (1.2)$$

The (1.2) can be rewritten as $\theta_E = (\kappa M \pi_{rel})$, where $\kappa = 4G/(c^2 au) = 8.144 \text{ mas } M_\odot^{-1}$ and $\pi_{rel} = au/D_L - au/D_S$ is the relative source-lens parallax. Assuming $D_L/D_S = 0.5$ and a lens mass of $M_L = 0.5 M_\odot$ we have for a source located in the Bulge $\theta_E \simeq 0.691 \text{ mas}$, while for a source in the Large Magellanic Cloud $\theta_E \simeq 0.285 \text{ mas}$ [8].

We can describe this scenario geometrically considering the configuration shown in Figure 1.3: the light of a source is deflected by an angle $\hat{\alpha}$ (defined in Eq. (1.1)) and the image is formed in the angular position θ .

The real angular position of the source is β and we call $\alpha = \theta - \beta$, where α is the angle between the source position and the image position. So given a deflection angle $\hat{\alpha}$ and the position of source and image we can relate these three quantities in the following way (considering the small-angle approximation):

$$D_S \beta = D_S \theta - D_{LS} \hat{\alpha} \quad (1.3)$$

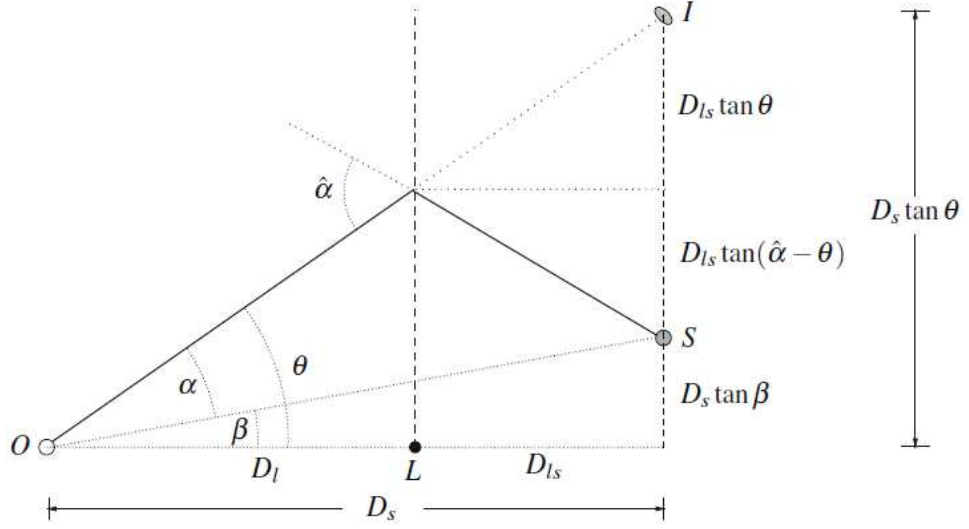


Figure 1.3: Geometric configuration of a gravitational lensing event with a point-lens. Credit image: Principles of Gravitational Lensing, Keeton, [9]

where $D_{LS} = D_S - D_L$. Defining $\alpha(\theta) = D_{LS}\hat{\alpha}(D_L\theta)/D_S$ we obtain the lens equation:

$$\beta = \theta - \alpha(\theta) \quad (1.4)$$

Assuming the simplest case of a point-mass lens, the Eq. (1.4) becomes:

$$\beta = \theta - \frac{D_{LS}}{D_S D_L} \frac{4GM}{c^2 \theta} = \theta - \frac{\theta_E^2}{\theta} \quad (1.5)$$

These equation has two solutions [1], $\theta_{\pm} = (\beta \pm \sqrt{\beta^2 + 4\theta_E^2})/2$. From this we know that the positive solutions θ_+ is always located at the same side of the source outside the Einstein ring, while θ_- always stays at the opposite side, inside the Einstein ring. Their angular separation is $\Delta\theta = \theta_+ - \theta_- = \sqrt{\beta^2 + 4\theta_E^2} \geq 2\theta_E$. Increasing the apparent lens-source separation we get that the smaller image reduces its dimensions as it approaches the lens until it disappears completely, while the larger image approaches the source until it coincides exactly with it (see Figure 1.4). We can normalize all the angular quantities by θ_E and defining $u = \beta/\theta_E$ and $y = \theta/\theta_E$ obtaining:

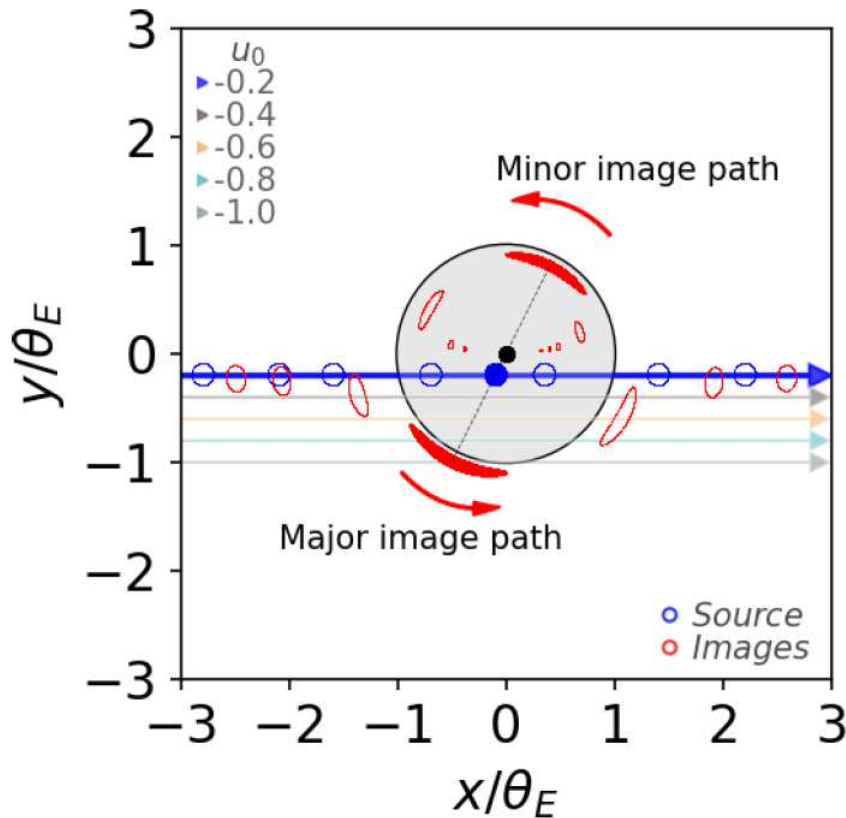


Figure 1.4: Geometric configuration of a single lens event. The black circle is the Einstein ring. Considering a frame in which the lens is fixed at the center of the plot with a black dot, the source trajectory is represented in five different configuration. Credit image: Microlensing Searches for Exoplanets, Tsapras, [10]

$$u = y - y^{-1} \tag{1.6}$$

1.2.1 Magnification

Since there are no processes of emission or absorption of photons during a microlensing event, the surface brightness is conserved [10]. In fact, if we consider an isotropic source and take an infinitesimal element dA_S the light ray coming from it will end up on the infinitesimal element of the image dA_I (i.e. the one observed by telescopes). The lensing effect is to modify the width of the

1. AN INTRODUCTION TO MICROLENSING

element which will therefore be distorted, thus modifying the subtended solid angle. We can define the total flux as the product of the surface brightness with the area covered in the sky (both for images and source). The magnification is defined as the surface area ratio between the image and the source:

$$A_{\pm} = \left| \frac{\theta_{\pm} d\theta_{\pm}}{\beta d\beta} \right| \quad (1.7)$$

Using the normalized coordinates we get the magnification of each images:

$$A_{\pm} = \frac{u^2 + 2}{2u\sqrt{u^2 + 4}} \pm \frac{1}{2} \quad (1.8)$$

The total magnification is given by the sum of the individual magnification:

$$A = A_+ + A_- = \frac{u^2 + 2}{2u\sqrt{u^2 + 4}} \quad (1.9)$$

In the most general case, since the lens equation acts as a mapping between the source plane and the lens plane we can express the magnification as a function of the determinant of the Jacobian defined as:

$$J = \det \frac{\partial \vec{\beta}}{\partial \vec{\theta}} \quad (1.10)$$

Where the angles are expressed in the vectorial notation give that a general lens may not necessarily have axial symmetry.

Since observer, lens and source are in relative motion, their position changes over time and consequently the angular separation will also be a function of time. In a first approximation if the timescale of the event is small and the accelerations are negligible we can assume the trajectory of the source relative to the lens rectilinear:

$$u(t) = \sqrt{u_0^2 + \left(\frac{t - t_0}{t_E}\right)^2} \quad (1.11)$$

where u_0 is the minimum impact parameter (or closest alignment) where the magnification reaches the maximum value (see Figure 1.5). t_0 is the time

1. AN INTRODUCTION TO MICROLENSING

when $u = u_0$ and t_E is called Einstein time and represents the timescale of the event. The last parameter contains the physical information of the event and it is related to the Einstein angle, since it is $t_E = \theta_E/\mu_{LS}$, with μ_{LS} relative proper motion between lens and source. The typical timescales of a microlensing event toward the Galactic Bulge is of order a month [7]:

$$t_E \simeq 24.8 \text{ days} \left(\frac{M}{0.5 M_\odot} \right)^{1/2} \left(\frac{\pi_{rel}}{125 \mu\text{as}} \right)^{1/2} \left(\frac{\mu_{rel}}{10.5 \text{ mas year}^{-1}} \right)^{-1} \quad (1.12)$$

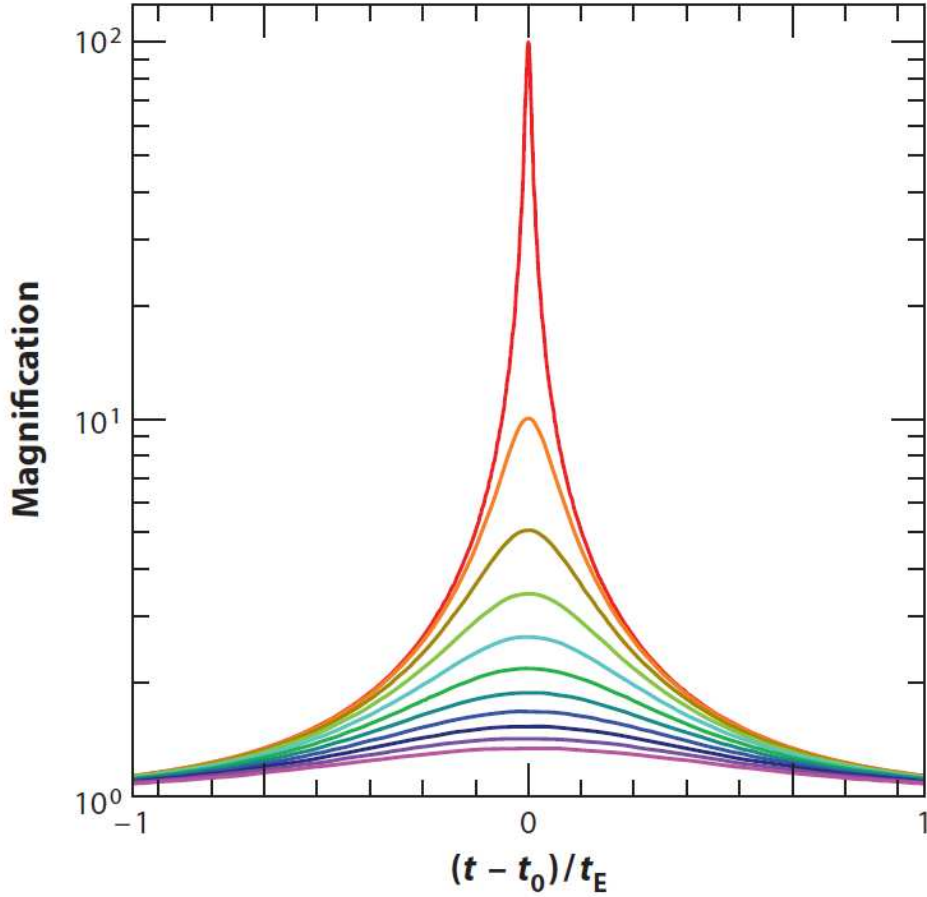


Figure 1.5: Magnification as a function of time for different values of u_0 . The lower the value of u_0 the higher the peak will be. Credit image: Microlensing Surveys for Exoplanets, Gaudi, [7]

1.2.2 Paczynski's curve

In the case of a single lens, the microlensing event can be described as in Figure 1.5. This type of symmetric and achromatic bell-shaped curve is called Paczynski's curve and the total flux $F(t)$ consists of two contributions:

$$F(t) = F_* A(t) + F_B = F_* \frac{u(t)^2 + 2}{u(t) \sqrt{u(t)^2 + 4}} + F_B \quad (1.13)$$

where F_* is the unlensed source flux and F_B is the blend flux and contains all the fluxes not affected by microlensing. It can be the flux of a background star or, in some cases, the lens itself. It does not change the shape and the timescale of the lightcurve but it only acts by raising or lowering the altitude of the peak. With five parameters (F_* , F_B , u_0 , t_0 , t_E) we can fit this kind of events. t_E is the only parameter that contains physical information about the lens. The Einstein time give us the timescale of the event and can vary the width of the lightcurve. In Eq. (1.13) we can find the height of the peak putting $t = t_0$

$$F(t_0) = \frac{u_0^2 + 2}{u_0 \sqrt{u_0^2 + 4}} F_* + F_B \quad (1.14)$$

and subtracting the baseline flux ($F_* + F_B$) we obtain a degenerate value depending only on F_* and u_0 . The latter, describing the minimum distance between lens and source, acts on the shape of the light curve.

1.2.3 Optical Depth and Event Rate

We know that a microlensing event appears when there is a precise alignment between observer, lens and source. But unfortunately this cannot be predictable and it is very rare. What can be done is to define quantities that allow us to quantify the probability that a microlensing event will occur. The first is the optical depth that gives us the probability that a star is inside the Einstein ring of a lens at a given time, star which will therefore be lensed. In order to have a microlensing event the impact parameter must be smaller

1. AN INTRODUCTION TO MICROLENSING

than θ_E . If we have $u_0 = 1$ then $A = 1.34$. Given a source at distance D_S and a lens with mass M at distance D_L we consider the microlensing tube that is the rotation solid obtained by the Einstein radius, as a function of D_L . We need to consider also all the potential lenses lying along the line of sight. In conclusion the optical depth is the integral over the number density of lenses multiplied by the area enclosed by their Einstein rings [10]:

$$\tau = \int_0^{D_S} \frac{4\pi G \rho(D_L) D_L D_{LS}}{c^2 D_S} dD_L \quad (1.15)$$

with $\rho(D_L) = \int_0^\infty dm (dn_L/dm d^3x) m$ the average mass density of lenses at D_L and (dn_L/dm) the mass distribution of lenses. For observations toward the Galactic bulge we have $\tau \simeq 10^{-6}$ while for observations toward the Large Magellanic Cloud $\tau \simeq 5 \cdot 10^{-7}$ [11].

More interesting is the microlensing event rate Γ that provides the rate at which a distant source undergoes a microlensing event due to a foreground lenses. The microlensing event happens if in the time interval dt the source lies in the fraction of the sky covered by the solid angle of width $2\theta_E$ and length $\mu_{rel} dt$. Assuming t_E as the timescale then:

$$\Gamma dt = \frac{2dt}{\pi t_E} \int_0^{D_S} n(D_L) D_L^2 \pi \theta^2 dD_L = \frac{2\tau}{\pi t_E} \quad (1.16)$$

Assuming a timescale in the bulge of $t_E \approx 20 - 30$ d the event rate is about $\Gamma \approx \tau / 10^{-1} \text{ yr}^{-1}$

1.2.4 Finite source effects

Stars are not point like sources but they have finite size that can be quantified by the parameter ρ_* defined as:

$$\rho_* = \frac{\theta_*}{\theta_E} \quad (1.17)$$

where $\theta_* = R_*/D_S$ is the angular radius of the star and R_* its physical radius. This parameter is relevant when the source passes near or across the caustic,

1. AN INTRODUCTION TO MICROLENSING

otherwise the source can be considered a point like star. The finite source effect comes into play in amplification in the following way (see Fig. 1.6 ([12]):

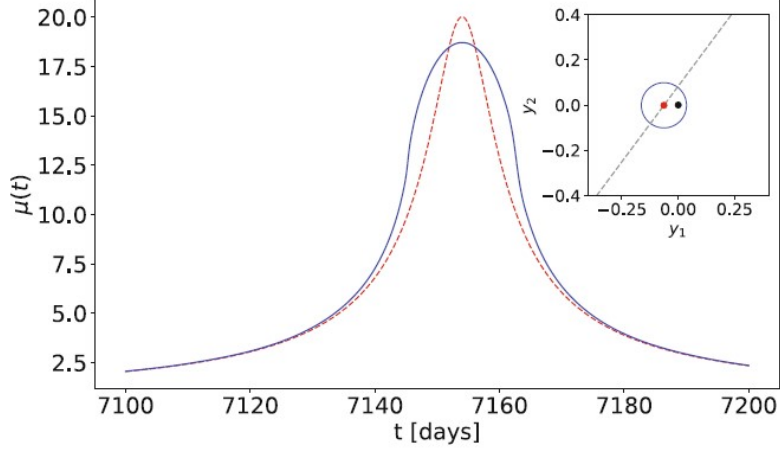


Figure 1.6: Lightcurve computation with finite source effect $\rho_* = 0.1$ (in blue) and without (in red). Credit image: Introduction to Gravitational Lensing, Meneghetti, [9]

$$A(y) = \frac{1}{F_*} \int_0^{2\pi} d\phi \int_0^{\rho_*} d\rho \rho I(\rho \hat{R}_E) \mu(\sqrt{y^2 + \rho^2 - 2y\rho \cos\phi}) \quad (1.18)$$

where $I(r)$ is the surface brightness, $\hat{R}_E = \theta_E / (D_L^{-1} - D_S^{-1})$ is the projected Einstein radius in the observer plane and μ the point source magnification. The total flux of the source is $F_* = \int_0^{2\pi} d\phi \int_0^{\rho_*} d\rho \rho I(\rho \hat{R}_E)$. At the peak $A(y = 0) = \sqrt{1 + 4/\rho_*^2}$. This is made for a uniform surface brightness but in reality limb darkening is present. In order to include it we have to rewrite the brightness profile in the following way:

$$I(\Psi) = I(0) \left[1 - \sum_{n=1}^{\infty} c_n (1 - \cos^n \Psi) \right] \quad (1.19)$$

where $\Psi = \theta_*/\theta_E$ and c_n are the limb darkening coefficients. In some cases microlensing could be an important technique to study stellar atmospheres.

1.3 The binary lens

Our Galaxy is rich of binary stars or multiple stellar systems [13]. Then it may happen to detect a microlensing event where the lens is binary (or also multiple). In some cases the mass of the second lens is very small compared to the first and most likely we are observing an exoplanet orbiting the host star. In order to study this case we implement the lens equation for a multiple lens system and we focus later on the binary lens. As made for the single lens, we introduce the dimensionless vectorial notation for the source position $\vec{u} = \vec{\beta}/\theta_E$ and the image positions $\vec{y} = \vec{\theta}/\theta_E$. We also introduce the mass ratio $\epsilon_i = m_i/M$ between the lens i and the total lens mass and $y_{m,i}$ that is the position of the lens mass i [7]. In this way the lens equation becomes:

$$\vec{u} = \vec{y} - \sum_i \epsilon_i \frac{\vec{y} - y_{m,i}}{|\vec{y} - y_{m,i}|^2} \quad (1.20)$$

Following the work of Witt [14] we define the complex notation in order to describe source and lens positions. Changing $\vec{u} \rightarrow \zeta = u_1 + iu_2$ and $\vec{y} \rightarrow z = y_1 + iy_2$ the Eq. (1.20) can be rewritten:

$$\zeta = z - \sum_i \epsilon_i \frac{1}{\bar{z} - \bar{z}_{m,i}} \quad (1.21)$$

If we take the complex conjugate of Eq. (1.21) we have an expression for \bar{z} that we can substitute in the previous equation in order to get a complex polynomial of order $n^2 + 1$ where n is the total lens number. For the binary lens we have 5 roots. But not always all the solutions give the physical image position. Indeed, depending on the source position with respect to the lens positions we can have some spurious solutions.

Using the complex notation we can calculate the determinant of the Jacobian:

$$\det J = 1 - \frac{\partial \zeta}{\partial \bar{z}} \frac{\partial \bar{\zeta}}{\partial z} \quad (1.22)$$

1. AN INTRODUCTION TO MICROLENSING

where $\partial\zeta/\partial\bar{z} = \sum_i \epsilon_i / (\bar{z} - \bar{z}_{m,i})^2$. Evaluating the inverse of Eq. (1.22) we obtain the magnification of every image. The total magnification is given by the sum of the contributions of all the images. The image positions where $\det J = 0$ provide the critical curves. We can find them by the condition:

$$\left| \sum_i \epsilon_i \frac{1}{(\bar{z} - \bar{z}_{m,i})^2} \right|^2 = 1 \quad (1.23)$$

Eq. (1.23) is equivalent to the condition $\sum_i \epsilon_i \frac{1}{(\bar{z} - \bar{z}_{m,i})^2} = e^{i\phi}$ where ϕ ranges from 0 to 2π . If we put the solutions of Eq. (1.23) in the lens equation we find the source positions where $\det J = 0$. This set defines the caustic curves, that is, the curves where the magnification diverges. They are characterized by folds (concave segments) and cusps (points where the folds meet). As the source approaches these regions the magnification begins to grow. As we will see later, the magnification does not diverge at these points since the sources, even if very distant, have a finite size.

Let us reconsider the Eq. (1.21) with $i = 2$ (i. e. the binary lens). We have:

$$\zeta = z + \frac{\epsilon_1}{\bar{z}_{m,1} - \bar{z}} + \frac{\epsilon_2}{\bar{z}_{m,2} - \bar{z}} \quad (1.24)$$

Our interest is to find the image location in the lens plane. In order to get this we invert the equation obtaining a fifth-order polynomial in z . In this case the roots cannot be obtained analytically but only numerically. As said before, depending on the source position with respect to the lenses we can have two spurious solutions. This means that three or five images will form.

Based on the lenses configuration we can have three topologies. The shape and the size of the caustics is determined by two parameters: the mass ratio between the two lenses $q = m_1/m_2$ and their instantaneous projected separation in units of θ_E , $s = |z_{m,1} - z_{m,2}|$. Based on the values of s and q , three different configurations of the caustics can be obtained: the close configuration with the formation of three caustics: one central and two smaller symmetrical ones located on both sides of the binary axis. For $s \simeq 1$ we

have the intermediate configuration where there is only one six-cusped central caustic. Finally there is the wide configuration with a central caustic and a secondary positioned along the binary axis. Introducing the parameter α that is the angle between the source trajectory and the planet-host axis, we can thus express the source position in the lens plane in the following way:

$$\begin{aligned} y_1 &= u_0 \sin(\alpha) - \frac{t - t_0}{t_E} \cos(\theta) \\ y_2 &= -u_0 \cos(\alpha) - \frac{t - t_0}{t_E} \sin(\alpha) \end{aligned} \tag{1.25}$$

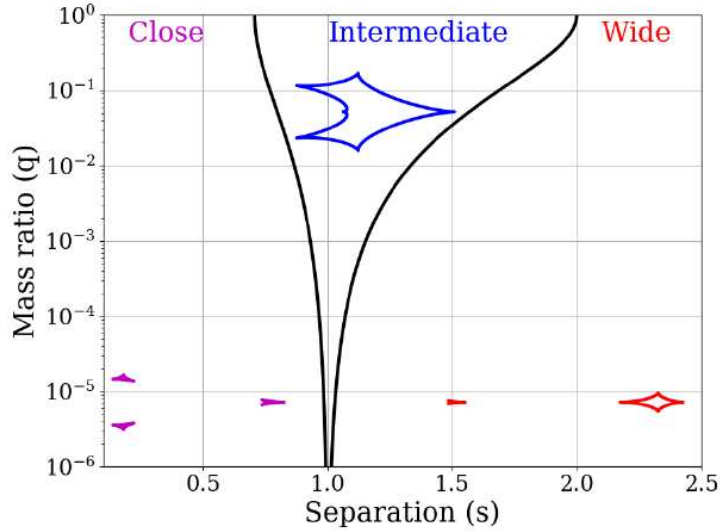


Figure 1.7: Boundaries between the three different topologies of caustics in the binary lens in the parameter space (s, q) . Also shown are three examples: the close configuration is obtained with $s = 0.75$, the intermediate with $s = 1$, the wide with $s = 1.5$. For all the cases $q = 10^{-2}$. Credit image: Microlensing Searches for Exoplanets, Tsapras, [10]

1.3.1 Binary lens: planetary configuration

When we have an exoplanet orbiting its host star, the mass ratio q with the primary lens is very small. Therefore, we generally refer to this limit as planetary configuration. The lightcurve is modulated principally by the host star while the planet generates perturbations (see Figure 1.8). These

perturbations can be produced only if the source crosses the regions inside or in proximity of the caustics. Far from these regions exoplanet detection becomes very unlikely. Similar to the case of the binary lens, also for the planetary case we can have three caustics configurations: considering $q \ll 1$ the boundaries between these configurations are [15]:

- Close configuration: $s < s_c \simeq 1 - 3q^{1/3}/4$
- Wide configuration: $s > s_w \simeq 1 + 3q^{1/3}/2$
- Intermediate configuration: $s_c < s < s_w$

As we will see later the lightcurve is invariant under the transformation $s \rightarrow s^{-1}$ thanks to the symmetry of the lens equation and in the limit of small q it is very difficult to distinguish between the two cases.

1.4 High order effects

1.4.1 Parallax

The assumption that the proper motion between lens and source is uniform is not strictly correct. The trajectory can be affected by the parallax effect. This phenomenon consists in a distortion of the lightcurve (see Figure 1.9) and arises from the accelerated motion of the Earth around the Sun [16].

Including the parallax effect the total transverse velocity \vec{v}_\perp must be modified:

$$\vec{v}_\perp = \vec{v}_{L,\perp} - \frac{D_L}{D_S} \vec{v}_{S,\perp} - \frac{D_{LS}}{D_S} (\vec{v}_{O,\perp} + AU \vec{\epsilon}'(t)) \quad (1.26)$$

In the previous equation $\vec{v}_{L,\perp}, \vec{v}_{S,\perp}, \vec{v}_{O,\perp}$ are the transverse velocities of lens, source and observer respectively. $\vec{\epsilon}'(t)$ represents the first derivative with respect to time of the vector $\vec{\epsilon} = (\cos \omega(t + \phi), \sin \beta \sin \omega(t + \phi))$ where β is the ecliptic latitude and ϕ is the phase which establishes the position of the Earth

1. AN INTRODUCTION TO MICROLENSING

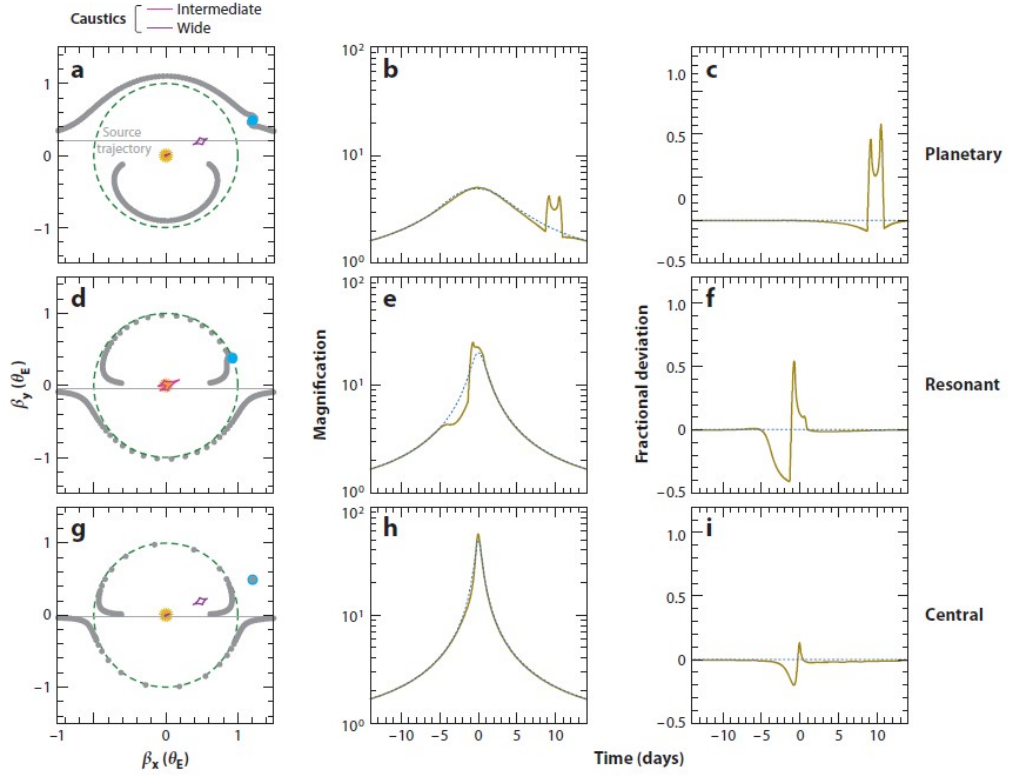


Figure 1.8: Schematization of three different planetary microlensing events: on the top (a,b,c) a wide configuration, with $s = 1.3$ and $q = 0.003$ where the source trajectory crosses the planetary caustic. In the middle we have (d,e,f) a resonant configuration with $s = 1.0$ and $q = 0.003$. In the bottom (g,h,i) another wide configuration where the source crosses the central caustic (also in this case $s = 1.3$ and $q = 0.003$) Credit image: Microlensing Surveys for Exoplanets, Gaudi, [7]

along its orbit. So both these angles are known. In these way the position of the source becomes:

$$\vec{y} = \vec{u}_0 + \frac{\vec{v}_\perp^0}{R_E}(t - t_0) - \frac{AU}{\tilde{R}_E} \vec{\epsilon}'(t) \quad (1.27)$$

It can be described by the parallax vector π_E with its two components along the East and North directions, $\pi_{E,E}$ and $\pi_{E,N}$ [17]. In addition to these two components, the parallax vector can be expressed in the components parallel to the projected direction of the Sun ($\pi_{E,\parallel}$) and the one perpendicular

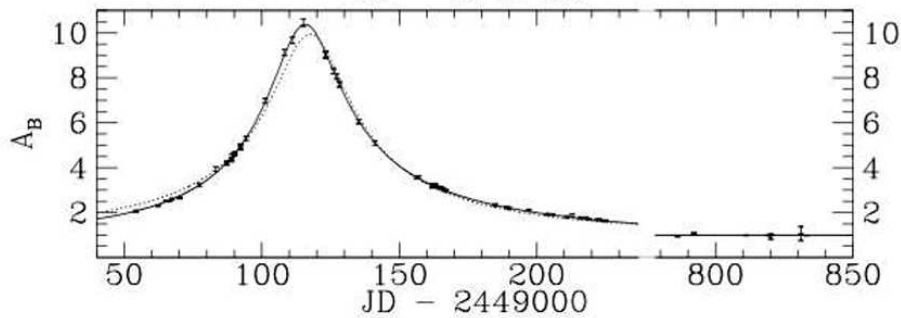


Figure 1.9: Lightcurve of a microlensing event with parallax effect. The dashed curve represents the static configuration while the fitted curve includes the parallax. Credit image: Rhavar, 2015, [8]

to it ($\pi_{E,\perp}$), which enter the equation of the lens, at the third and fourth order respectively. Its effect is particularly strong when the time scale of the microlensing event is comparable to the orbital period of the Earth, while the parallel component to the direction of the Sun leads to an asymmetry of the lightcurve, the other component induces a symmetric distortion.

Parallax can be related to the Einstein angle:

$$\pi_E = \frac{\pi_L - \pi_S}{\theta_E} = \frac{\theta_E}{\kappa M} \quad (1.28)$$

where π_L is the lens parallax and π_S is the source parallax. The parallax is very important because if we can measure both π_E and θ_E we can obtain the mass and the distance of the lens:

$$D_L = \frac{AU}{\pi_E \theta_E + \pi_S} \quad (1.29)$$

The parallax effect can be obtained also in other ways. For example with two observers, and one of them is an orbiting satellite (but also with two different observatories, in this case we have the geocentric parallax). They observe the event simultaneously but since their point of view is not the same they will have a different u_0 and t_0 (see Figure 1.10) . In this case the parallax vector is defined as:

$$\pi_E = \frac{AU}{D_\perp}(\Delta\tau, \Delta\beta) \quad (1.30)$$

where D_\perp is the separation projected in the sky between the two observers, while $\Delta\tau = (t_{0,sat} - t_{0,Earth})/t_E$ and $\Delta\beta = u_{0,sat} - u_{0,Earth}$. With the satellite parallax a fourfold degeneracy arises as we will see later.

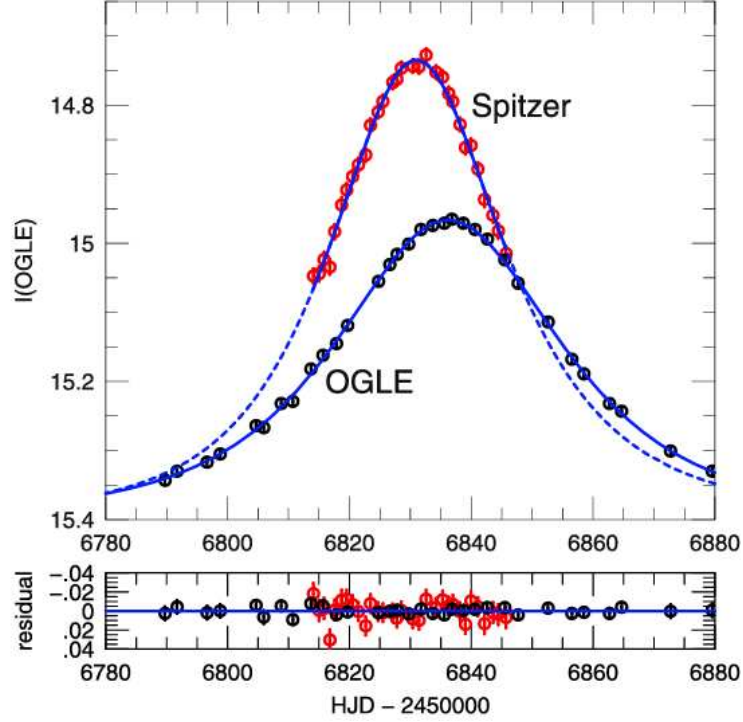


Figure 1.10: Lightcurve of a microlensing event detected by satellite (Spitzer) and Earth telescope (OGLE): the two lightcurve are different since u_0 and t_0 are not the same. The difference yields the parallax vector π_E . Credit image: Yee et al, 2015 [18]

1.4.2 Orbital motion

When a binary lens is detected, typically their relative positions are considered fixed. This is the case of static lens and for event with a short timescale is a good approximation. But if the event is very long and the source passes very close to the caustic we can detect the orbital motion of the

lens. This effect is shown in the changing of the shape of the caustics and in the variation of their orientation (see Figure 1.11).

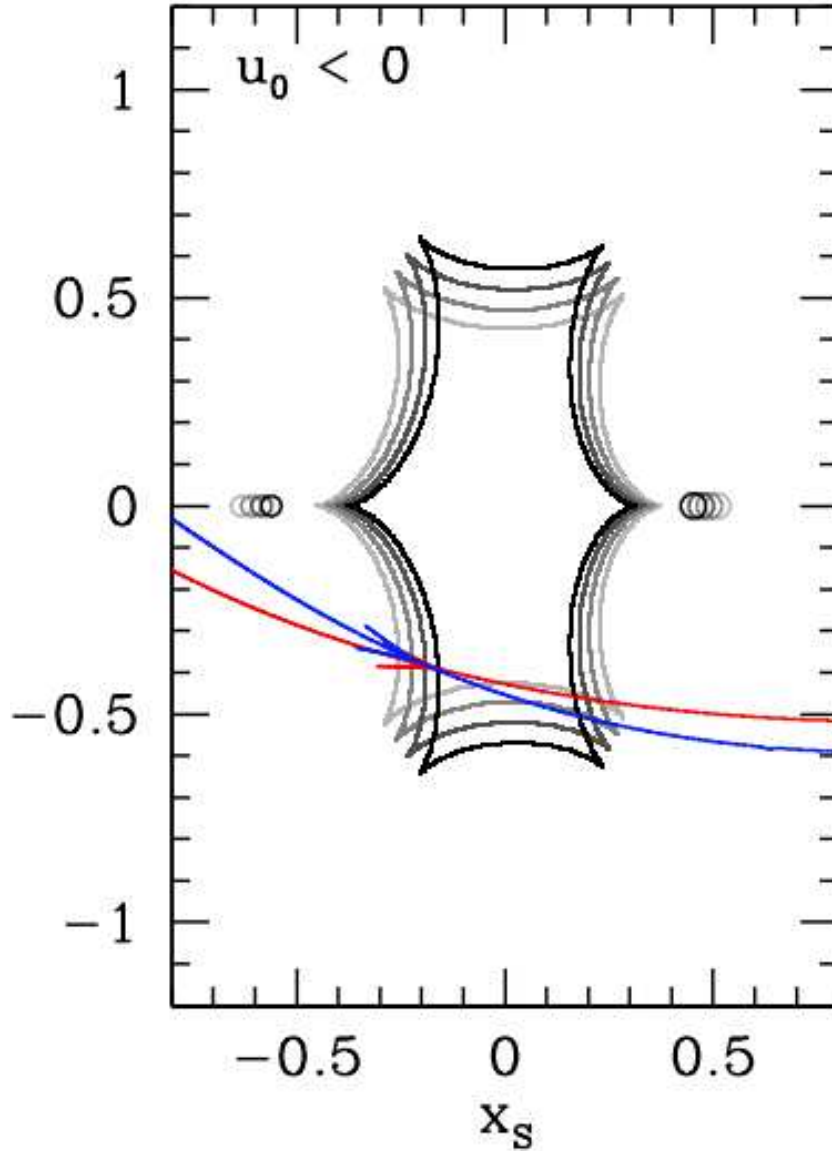


Figure 1.11: Caustic configuration of microlensing event OGLE-2015-BLG-0479. The temporal evolution of the resonant caustic due to the orbital motion of the binary system can be noted. The blue and red line indicate the source trajectory seen by ground telescope and satellite respectively. Credit image: Han et al, 2016 [19]

It can be described by the three components of the companion's velocity relative to the host star: the parallel component $\gamma_{\parallel} = (ds/dt)/s$,

the perpendicular component $\gamma_{\perp} = (d\alpha/dt)$ and the component along the line of sight of the observer $\gamma_z = (ds_z/dt)/s$ [20], [21]. The last is very poorly constrained by typical microlensing events. This description has the assumption that the orbit is circular but, albeit very rarely, it is possible describe the orbit with a fully Keplerian motion including the eccentricity.

When the orbital motion is detected another step must be done. Once we get the mass and the distance of the lens they must be compatible with the orbital parameters, if present. In order to have the compatibility the ratio between the projected kinetic energy and the projected potential energy must satisfy the following inequality [20]:

$$\frac{v_{\perp}^2 r_{\perp}}{2GM} = \frac{(\gamma_{\perp}^2 + \gamma_{\parallel}^2) s^3 \theta_E^3 D_L^3}{2GM} < 1 \quad (1.31)$$

where $r_{\perp} = s\theta_E D_L$ and v_{\perp} is the projected velocity. If the ratio in Eq. (1.31) is > 1 the orbital parameter obtained are unphysical. These parameters could be wrong also if the ratio is $\ll 1$ since r_{\perp} and v_{\perp} represents two components of their respective vectors so one expects a ratio of a few at most.

1.4.3 Binary source

Just as it is possible to find binary lenses, the same can be said for sources. In the simplest case if we have two sources the total lightcurve is given by the sum of the two Paczynski curves, with the same t_E . Or, if the two source are well separated, we will see two different peaks with their u_0 and t_0 . This type of event is chromatic since the two sources may have different color [22].

1.4.4 Xallarap

If the binary source is a gravitationally bound system we can detect their orbital motion around their common centre of mass.

This effect is called Xallarap since its effect on the light curve is the same of the parallax (see Figure 1.12). It is possible define a parameter [24]

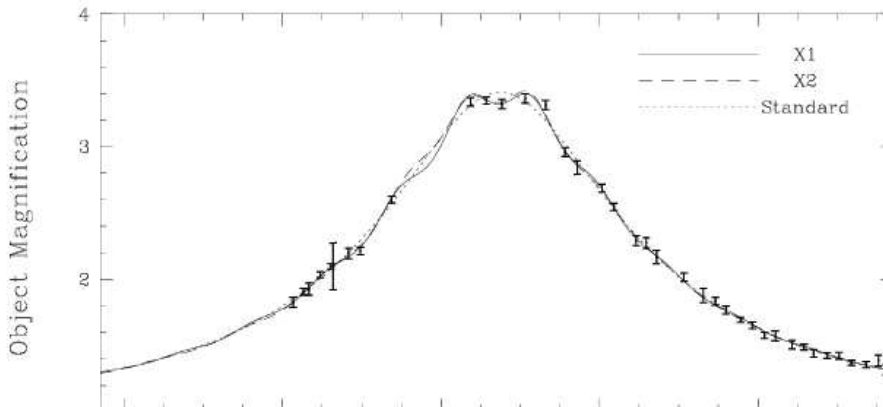


Figure 1.12: Lightcurve of microlensing event MACHO 96-LMC-2 described by a Xallarap model (continuous line) Credit image: Alcock et al, 2001, [23]

$\chi_E = (m_2/M_S)/(a/D_S\theta_E)$ where M_S is the source mass and m_2 is the source companion. a represents the semi-major axis of the binary source orbit that in a first approximation we can assume circular (refer to the chapter dedicated to the event of MOA-2006-BLG-074 for further details).

If this effect is very marked, in principle it would also be possible to detect an exoplanet orbiting the source, provided that the planet is very close to the star and has at least one Jovian mass [24]. Further, the Xallarap effect can mimic a planetary signal making it a contaminant for planetary microlensing.

1.5 Degeneracies in microlensing

The cases of microlensing events is disparate. We can have an incredible number of different configurations (binary stars, star and exoplanets, free floating planets, etc.). But often some problems arise during the analysis of a microlensing event, i.e. the degeneracies. When we have a degeneracy we are saying the we can describe the same light curve with a different set of parameters.

The first degeneracy already occur in the case of a single lens: for example if we consider the parameter t_E : this is the only measured parameter that contains physical information about the lens. Inside it there are mass and distance of the lens but without other information (θ_E or π_E) we have a degeneracy on

1. AN INTRODUCTION TO MICROLENSING

the determination of mass and distance. Obviously we cannot consider a high mass star located very near to the observer if there is no lens flux detectable. Always from the single lens there is another degeneracy: $u_0 \leftrightarrow -u_0$. Indeed if in a first approximation we assume a rectilinear uniform motion of the source. In this case the lightcurve is the same whether the source passes the lens on its right ($u_0 > 0$) or left ($u_0 < 0$). In the same way, extending this concept for the binary lens, there is a similar degeneracy including the source direction α and $-\alpha$ and we have $(u_0, \alpha) \leftrightarrow -(u_0, \alpha)$. Considering the binary lens, in the limit of $q \ll 1$ one more degeneracy comes to life: the close-wide degeneracy $s \longleftrightarrow 1/s$. It is due to the symmetries of the lens equation and it is very relevant when the source passes near the central caustic ($s \ll 1$). Another degeneracy that comes in planetary microlensing is the inner/outer degeneracy [25]. This is caused by the passage of the source in the two opposite sides of the central caustic. The inner case is when the source is in the inner region of the planetary caustic, outer otherwise.

A unification of these two degeneracy is the offset degeneracy [26]. It is a magnification degeneracy whose formulation is independent of caustics. The relationship between the two configurations is given by:

$$s_a = \frac{1}{2} \left[2x_0 - \left(s_b - \frac{1}{s_b} \right) + \sqrt{\left[2x_0 - \left(s_b - \frac{1}{s_b} \right) \right]^2 + 4} \right] \quad (1.32)$$

where $x_0 = u_0/\sin(\alpha)$ and s_a and s_b indicate the two degenerate separations s .

In planetary microlensing if the finite source effect parameter is measured we have a degeneracy between ρ_* and q : this happens because this two parameters enter the determination of the planetary perturbation Δt_p [27]. The inclusion of parallax gives rise to other degeneracies. For example, when the satellite parallax is present there is the four-fold satellite degeneracy [28] where there are four competitive models obtained by the reflection of the source trajectory around the lens axis changing the signs of the parallax components.

Some degeneracies arise also with the binary source. The first happens when the planetary perturbation with $s > 1$ can be described by a binary source

model. Always with binary source models, when Xallarap is detected a degeneracy with a binary model with parallax could be possible: this because Xallarap can mimic the parallax effect thanks to the similarity in the lightcurve of the binary source motion and the reflex motion of the Earth. We can deal with another type of degeneracy called ecliptic [20]. This degeneracy takes place in particular conditions: first of all it happens when the direction of the Sun's acceleration is constant and we have this condition when the source lies on the ecliptic or if the timescale of the event is shorter than the variation of the direction's acceleration.

This degeneracy takes $u_0 \rightarrow -u_0$ and $\pi_{E,N} \rightarrow -\pi_{E,N}$ [29]. Including also the orbital motion the implementation is $\gamma_{\perp} \rightarrow -\gamma_{\perp}$ [20]. When the microlensing event is detected by two telescopes and one of these is a satellite, there is a fourfold degeneracy due to the fact that the sign of u_0 cannot be determined. The Figure 1.13 shows all the possible configurations of the source trajectory seen from Earth and satellite.

In principle the orbital motion may break this degeneracy but if it is not measured we note that $\Delta\beta_{++} = \Delta\beta_{--}$ and $\Delta\beta_{+-} = \Delta\beta_{-+}$. This implies that $\pi_{E,++} = \pi_{E,--}$ and $\pi_{E,+-} = \pi_{E,-+}$ with the passage from a fourfold degeneracy to a twofold degeneracy that can be broken with the higher order effect in the ground based data or by the so called Rich Argument, i.e. an extra geometric factor that disfavors the large-parallax solutions [31].

1.6 Why is microlensing important?

A microlensing event is rare, unpredictable and with a transient signal. Since most sources are low-mass stars the events are usually faint. But despite everything, microlensing is a method of fundamental importance for the discovery of exoplanets (see Figure 1.14). First of all is the principal method, if not the only one, able to discover planets just beyond the snow mass line. This because the Einstein ring radius is typically located just beyond the region

1. AN INTRODUCTION TO MICROLENSING

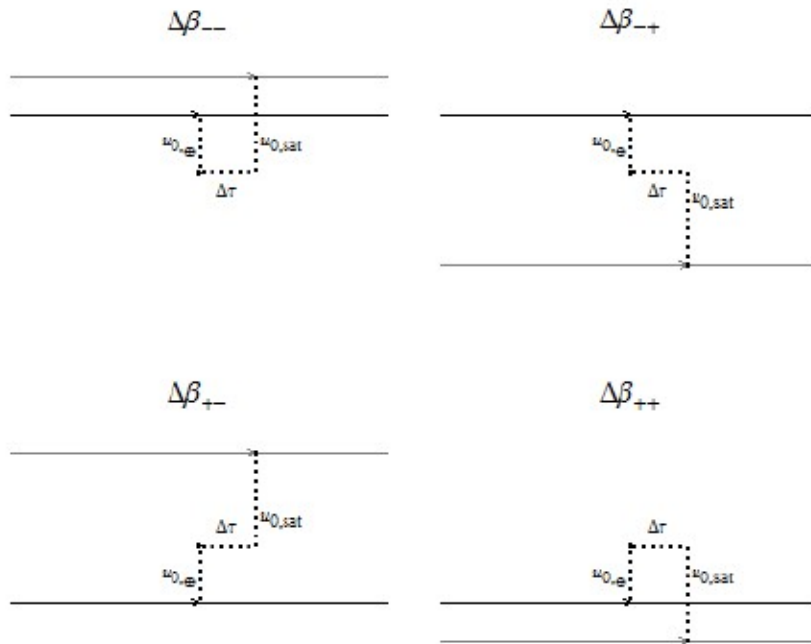


Figure 1.13: The four combinations of the source trajectory seen from satellite and Earth Credit image: Methods of detecting exoplanets, Bozza et al.[30]

where the midplane disk temperature is below the sublimation temperature of water, i.e. the snow line. Microlensing is sensitive to low-mass planets: this is possible since the magnification due to a planet does not depend on its mass but on the distance of the source from the caustic whose size scales as $\approx m_p^{1/2}$. From this it can also be deduced that microlensing is capable of detecting long-period planets and also free floating planets up to masses equal to those of Mars. Moreover, it does not matter which object the planet orbits, making it possible to find exoplanets in all types of systems: brown dwarfs, red dwarfs, white dwarfs, etc. Even if the event occurs only once and cannot be repeated, its duration is at most of the order of months and does not require the intervention of large telescopes. Another important feature of microlensing is its sensitivity to multiple-planet systems. In principle, for low-magnification events we can detect multiple planets if the source crosses the planetary caustics while for high magnification events it does not matter where the planet is located respect to the source: the probability to detect it

1. AN INTRODUCTION TO MICROLENSING

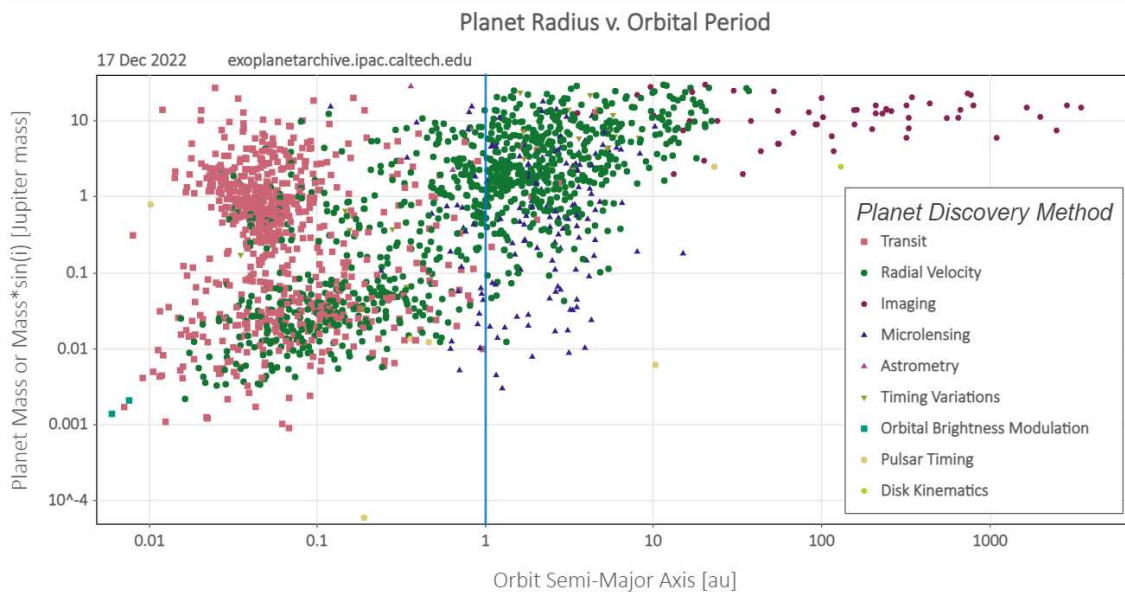


Figure 1.14: Mass versus semi-major axis of all exoplanets detected up to the 17 December 2022. We can see how all the techniques to discover exoplanets are complementary each other. We can note how most exoplanets detected by microlensing lie beyond the snow line, represented by the blue vertical line. Credit image: Nasa Exoplanet Archive

is very high. The fact that planetary systems can be found in both the disk and the bulge makes microlensing the only method by which it is possible to study the exoplanet demographics of two different populations of stars.

Microlensing is not just important for exoplanets. Thanks to this technique we are able to detect brown dwarfs (in binary systems or as free floating objects) that are objects of which not much is known, given their difficulty in being detected. In this way we are able to get more information about this mysterious objects making possible the implementation of a statistics for their distribution. With microlensing the importance of binary systems is emphasized making it possible to have a better understanding of their frequency and the variety of binary systems that can be detected making a better comprehension of distributions star in our galaxy. Other objects that can be revealed by microlensing are isolated black holes which, being ultra-compact objects, would be unique lenses of their kind. Of the particular

1. AN INTRODUCTION TO MICROLENSING

types of black holes that could be detected with microlensing are primordial black holes (PBHs), compact objects formed soon after the Big Bang. Since during their formations there were no stars PBHs are supposed to be composed of dark matter [32]. Indeed they belong to the MACHOs that can be discovered thanks to microlensing which, once again, is fundamental for the study of these objects.

CHAPTER 2

MODELLING A MICROLENSING EVENT

The main goal of the analysis of a microlensing event is to find the physical parameters of the lens system. In order to do this it is very important to find the best model that describes the lightcurve by minimizing the χ^2 with the data. The data can be provided by the various telescopes around the world and also in space, which are managed by various international collaborations.

2.1 Observations

The first observational campaigns of microlensing were focused on the search for MACHOs. It was thanks to Mao and Paczynski that microlensing was used to search for exoplanets. Being microlensing a random but above all rare phenomenon, in order to have a large number of events it is necessary to observe in areas of the sky densely populated by stars. Therefore the mainly observed region is that of the galactic bulge (since the optical depth is of $\approx 10^{-6}$). In this way we have a large amount of sources and lenses located both in bulge and disk with the possibility to study different star populations

2. MODELLING A MICROLENSING EVENT

thus having a great help for understanding the structure of the Milky Way and its dynamics.

Principally we have two types of microlensing observations: the ground-based and the space-based. The former are made with telescope located on Earth while the latter are obtained with the space satellites.

2.1.1 OGLE

The Optical Gravitational Lensing Experiment (OGLE) is the oldest microlensing project still running at present time. It started in 1992 thanks to Andrzej Udalski with the goal of the detection of variable stars, microlensing events and novae together with the study of Milky Way structure. The main targets observed are the Magellanic Clouds and the Galactic Bulge using the telescopes located at the Las Campanas Observatory in Chile (see Figure 2.1).



Figure 2.1: Las Campanas Observatory, Chile Credit image: OGLE collaboration

The OGLE collaboration gave us the first microlensing event in the galactic bulge [33]. Now it has reached the fourth phase of observations

2. MODELLING A MICROLENSING EVENT

(OGLE-IV, [34]) including the monitoring of Large and Small Magellanic Cloud with the use of the 1.3 m telescope with a field of view of 1.5 deg^2 covered by 32 mosaic CCD detectors whose resolution is of 2048×4102 pixels (see Figure 2.2). The photometry spans the range of $12 < I < 21$ mag for the Bulge and $13 < I < 21.7$ for the Magellanic system. The cadence of observations spans from 19-60 minutes in the inner Galactic bulge to 1-3 days for the rest of the fields. For the follow-up observations OGLE implemented the Early Warning System software to report ongoing microlensing event [35].

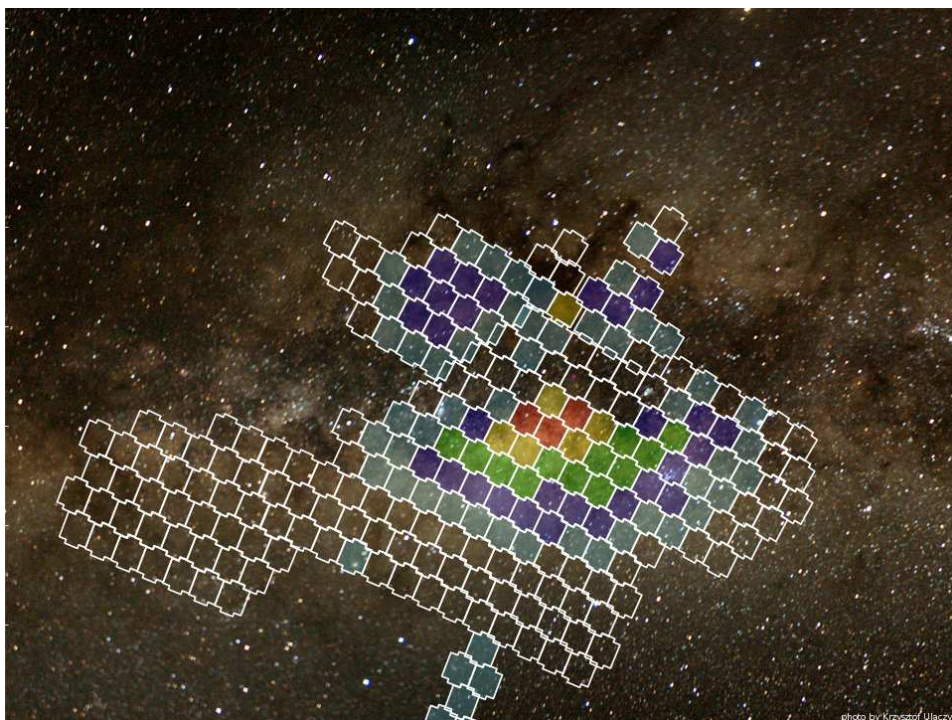


Figure 2.2: OGLE fields in the sky map. Credit image: OGLE collaboration

2.1.2 MOA

The Microlensing Observations in Astrophysics (MOA) was born from the collaboration between Japan and New Zealand in 1995. Their first goal was the study of the optical depth towards the Galactic bulge. In collaboration with OGLE they detected the first confirmed microlensing planet [36]. Always with OGLE they found the signs of the first rogue black hole in our galaxy [37]. For the observation MOA uses the 1.8 m telescope 2.3 located at Mt. John

2. MODELLING A MICROLENSING EVENT

University Observatory to which a wide field mosaic CCD has been mounted with 2000×4000 pixels covering a field of view of 2.2 deg^2 . In addition to microlensing events MOA analyzes and studies transits, variable stars and more. The fields of view are basically the galactic bulge (see Figure 2.4) but also the Magellanic system.



Figure 2.3: MOA telescope at the top of Mount John Credit image: MOA collaboration

2.1.3 KMTNet

The third main group of microlensing observation is the Korean Microlensing Telescope Network (KMTNet, [38]), a wide-field survey system with three telescopes 1.6 m wide located in the Southern hemisphere: the KMT-A in Siding Spring Observatory (SSO) in Australia, the KMT-S in the South African Astronomical Observatory (SAAO) in South Africa (see Figure 2.5) and the KMT-C located in Cerro-Tololo Inter-American Observatory (CTIO) in Chile. All the telescopes have a mosaic of four 18000×18000 CCDs providing a 2.0 by 2.0 square degree field of view [38]. KMTNet is focused on

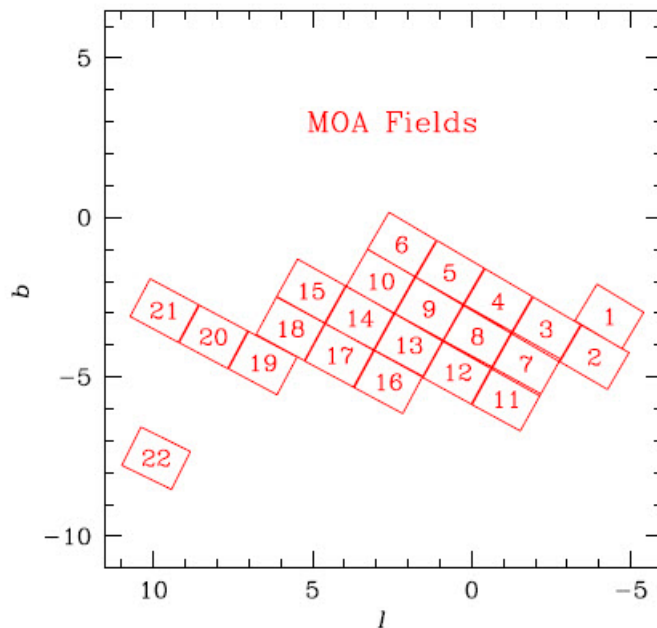


Figure 2.4: The 22 target fields observed by MOA surveys with the discovery of approximately 6000 microlensing events. Credit image: MOA collaboration

the search for exoplanets using microlensing especially the Earth-mass planets in the habitable zone. The location of their telescope has the advantage of being able to observe the galactic bulge continuously (see Figure 2.6). Also this collaboration has implemented an alert system to report all microlensing events discovered by KMTNet.

2.1.4 Satellite microlensing

Microlensing can be studied also using satellite telescopes. Simultaneously observing a microlensing event from the ground and from a satellite allows for parallax measurements, providing additional data for determining the physical parameters.

Spitzer

The most important space-telescope used for creating a sample of events with well-measured parallaxes is the Spitzer satellite [39]. It was launched in



Figure 2.5: The 1.6 m telescope located in South Africa for the KMTNet collaboration. Credit image: KMTNet collaboration

2003 and remained active until 2020. Starting from 2014 Spitzer has made a great contribution to microlensing with more than 700 events detected toward the Galactic bulge thanks to the IRAC camera (InfraRed Array Camera), an infrared camera used to obtain images and photometry. Of the four bands available, the one used for microlensing was centered at 3.6 micron. Among all the microlensing events detected, there was information on the mass of about ten isolated lens objects ([40]–[44]).

Kepler

Initially planned for the search for exoplanets with the transit method, the Kepler satellite has also made an important contribution to microlensing. Equipped with a 0.95 Schmidt telescope and 105 deg^2 field of view acquires images thanks to the array of 42 CCDs of 2200×1024 pixels each. The use of

2. MODELLING A MICROLENSING EVENT

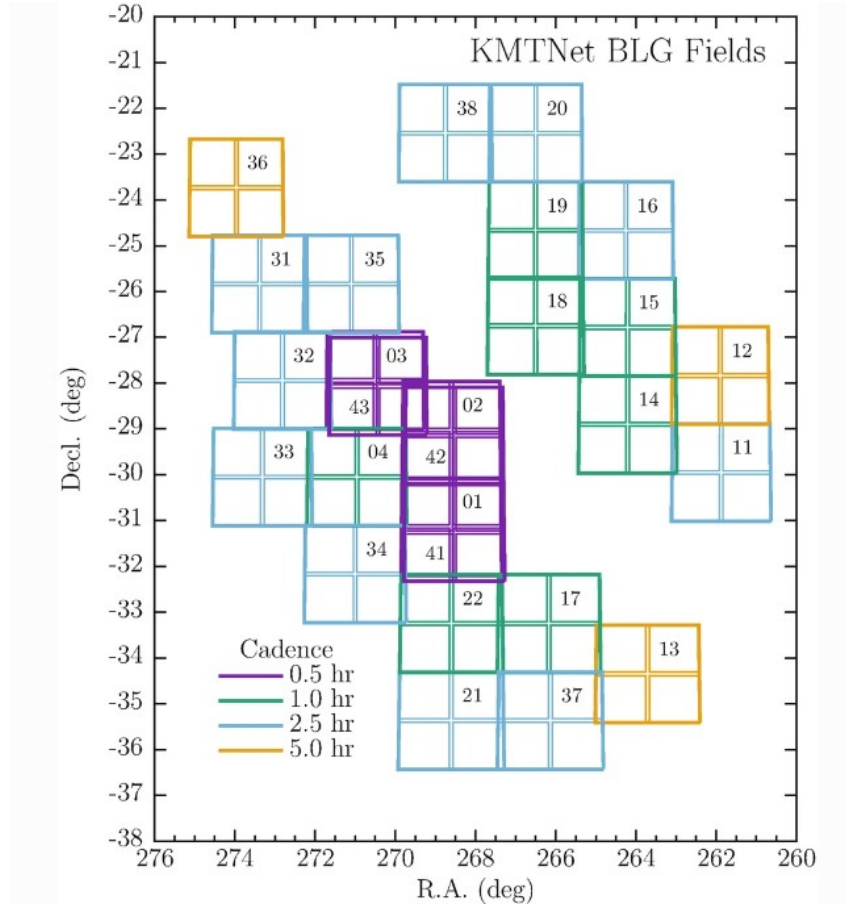


Figure 2.6: Fields observed by KMTNet in 2016, color-coded by cadence. Credit image: KMTNet collaboration, Matthew Penny

telescope for microlensing was first considered to find primordial black holes [45] but later with the Campaign 9 (K2C9) conducting a 3.7 deg^2 survey toward the Galactic bulge it was programmed to measure the parallax for more than 170 events and find exoplanets, including free floating planets [46].

Gaia

Gaia is one of the most important satellites of the present decade whose mission is to construct the most accurate three-dimensional map of our Galaxy observing more than 2 billion stars. Gaia is monitoring the sky continuously and a small fraction of the objects observed constitutes microlensing events which can reach up to magnitude 20.7 in Gaia's G-band [47]. One of the first and important microlensing events detected was Gaia16aye, a binary

2. MODELLING A MICROLENSING EVENT

system composed by two main-sequence stars with follow-up covering of about 500 days [48]. Up to now more than 360 microlensing events were detected and of these 90 have not been detected by other surveys [49]. The fact of continuously monitoring the entire Milky Way means that microlensing events can be detected all over the sky. Furthermore, Gaia can measure the small deviation of the centroid of the two images around the trajectory of the source giving huge perspectives for the new microlensing era based on astrometry [50].

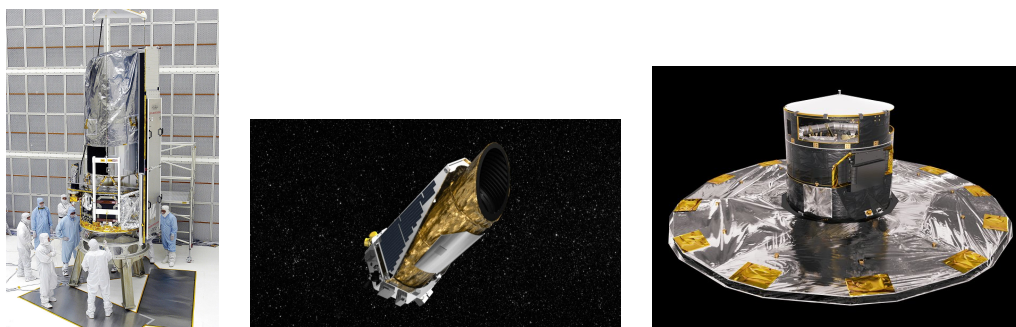


Figure 2.7: (Left) The Spitzer telescope in the Jet Propulsion Laboratory. (Center) Artistic representation of Kepler satellite. (Right) Artistic representation of Gaia satellite. Credit images: NASA/ESA

Roman Telescope

The Nancy Grace Roman Space Telescope (formerly known as WFIRST, the Wide Field Infrared Survey Telescope) is the future of microlensing. The main goals of this telescope are the discovery of exoplanets through microlensing and the study of dark matter and dark energy. The field of view of this of 2.4 m telescope is 200 larger than Hubble. For the microlensing it will use the Wide Field Instrument, a 300.8 megapixel camera. It is expected that Roman will detect more than 2600 exoplanets by monitoring 100 million stars (see Figure 2.8), where many of them are beyond the snow line, making Roman an ideal companion for Kepler and Tess [51].

In the future, Roman will be able to work together with the Euclid satellite for a joint survey on microlensing, the purpose of which will be to

2. MODELLING A MICROLENSING EVENT

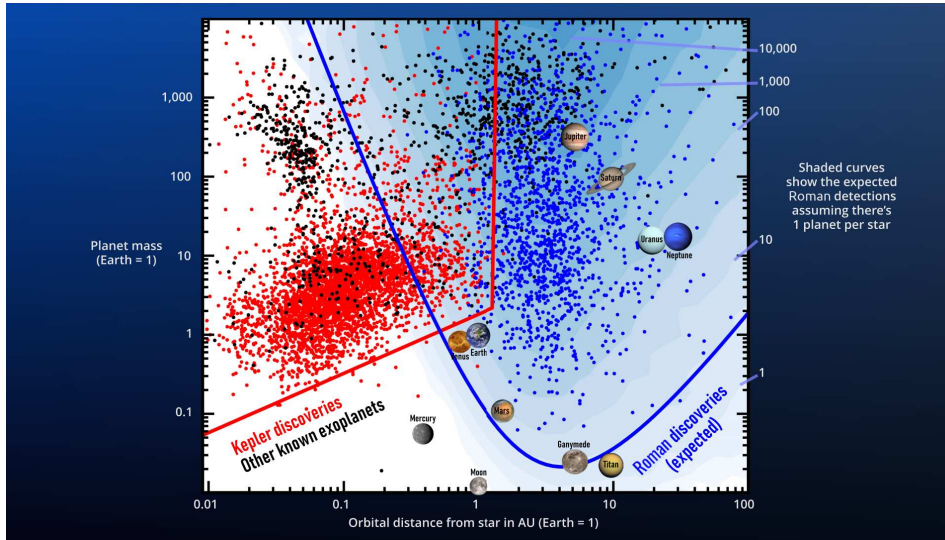


Figure 2.8: Prediction of exoplanets discovered by Roman telescope compared with the Kepler satellite Credit image: NASA’s Goddard Space Flight Center, adapted from Penny et al. (2019) [51]

detect free floating planets (130 per year) and the characterization of exomoons [52].

2.1.5 High resolution imaging: Hubble and Keck

In some cases it is difficult to obtain the correct properties of lens and source in microlensing events. If the proper motion of these objects is such that years after the event they separate, they can be observed distinctly with telescopes equipped with adaptive optics providing high resolution images. In this way, telescopes such as the Hubble and Keck, come to our aid, thanks to their instrumentation they are capable of distinguishing and separating lens and source in order to obtain even more precise information on their physical properties and proper motion. In conclusion the measure of the lens flux and of the relative proper motion can be useful to provide strong constraints and will discriminate between models in order to get a better measurement of θ_E [53]

2.1.6 Follow-up

A fundamental role for the observations of microlensing events belongs to the follow-ups, thanks to which it is possible to have more data and therefore more information on the event in progress. One of the first follow-up was PLANET (Probing Lensing Anomalies NETwork, [54]), now no longer in operation and merged in 2009 with another follow-up group, Microlensing Follow-Up Network (μ FUN, [55]), an informal consortium of observers dedicated to photometric monitoring of interesting microlensing events in the Galactic Bulge. For this thesis it is necessary to introduce two more follow-up groups with which the microlensing events present in the following chapters were analyzed.

MiNDSTEp

The Microlensing Network for the Detection of Small Terrestrial Exoplanets (MiNDSTEp) is an international collaboration whose purpose is to find exoplanets within our Galaxy using microlensing. The telescope used for observations is the 1.54 m Danish Telescope located at La Silla in Chile (see Figure 2.9)

The microlensing targets are from GAIA, MOA and OGLE in high time resolution, using a two color lucky imaging camera. In addition to microlensing, side projects such as transits, occultations, etc. are also carried out.

OMEGA Key Project

Observing Microlensing Events of the Galaxy Automatically or OMEGA Key Project is an international collaboration focalised on follow up of microlensing event in order to detect and characterize cold planet and stellar remnants. All the microlensing candidates are collected in the Microlensing Observing Platform (MOP) and analyzed by pyLIMA. The observations are made automatically with the aid of Las Cumbres Observatory automatic

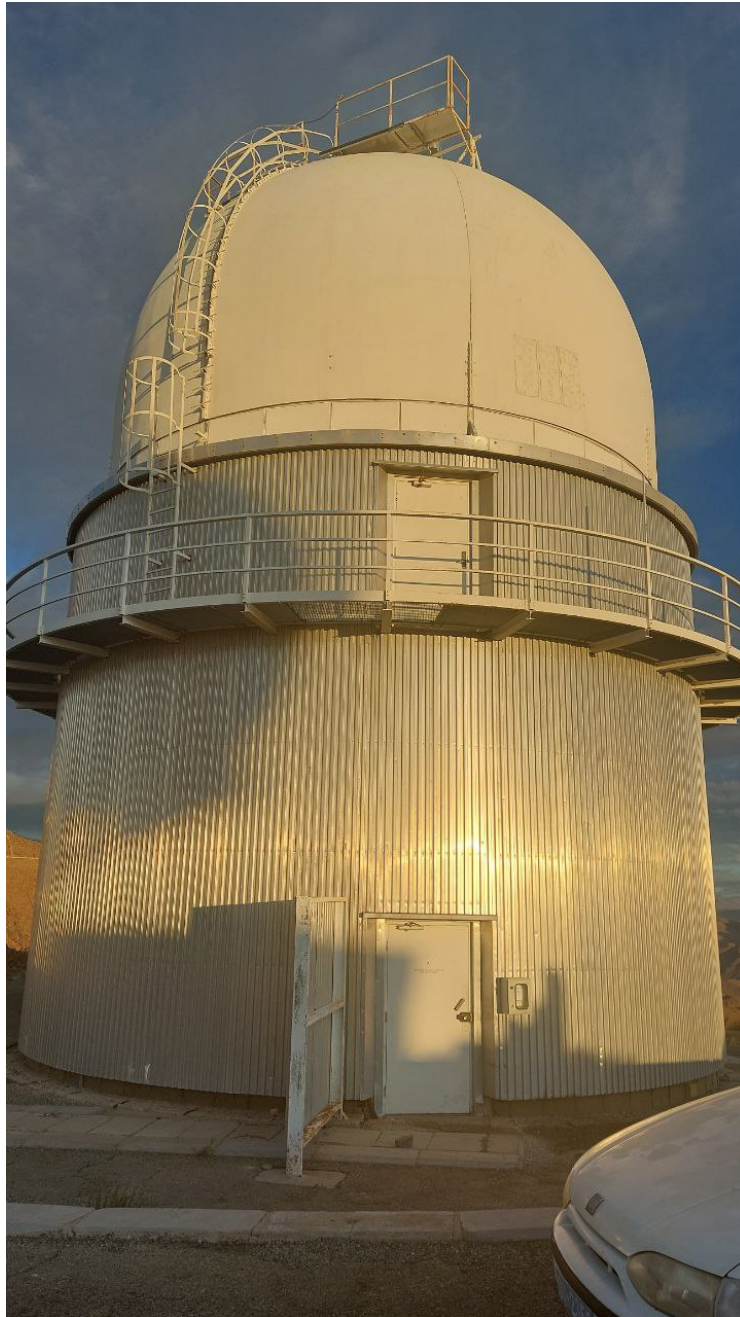


Figure 2.9: 1.54 m Danish Telescope at La Silla in Chile. Credit image: Paolo Rota

robotic telescope network.

2.2 Lightcurve computation

The computation of the light curve from the data obtained from the telescopes of a microlensing event is the most important step in determining the physical parameters of the event.

The numerical calculation of the light curve can be done in two ways: the inverse ray shooting and the contour integration.

2.2.1 Inverse Ray Shooting

The starting point is the lens equation (1.4) introduced in the first chapter:

$$\vec{y} = \vec{x} - \vec{\alpha}(\vec{x}) \tag{2.1}$$

where we are considering the normalized notation and $\vec{\alpha}(\vec{x})$ is the normalized deflection angle that contains all the constants. This implementation of the lens equation is suitable for mathematical study. We can consider it as a mapping between the source plane and the lens plane. With this equation we can describe the trajectory of a ray of light which goes from one plane to another. Since the light ray is invariant under time reversal it doesn't matter which direction we consider from the mathematical point of view. The inverse ray shooting is based on this assumption: starting from the observer we track the trajectory up to the source plane in order to solve the lens equation [56]. From the observer to the lens the trajectory is a trivial straight line without deflection. At the observer plane the rays will be deflected an amount given by the deflection angle. In the end, from the lens plane to the source plane there is no deflection and we have again a straight line. With a full scan of the lens plane, whose points are switched on if the light rays complete their path within the radius of the source, we are able to reconstruct all the images obtaining information about magnification. The inclusion of the limb darkening is, in a certain sense, almost automatic, given that we know where the ray falls in the source, thus having information on the local surface brightness.

2.2.2 Contour Integration

Another way to compute the lightcurve is the contour integration based on the resolution of the lens equation for all the points in the source boundary deriving the magnification with the Green's theorem. In practice, the \vec{x} positions of the images are obtained starting from the \vec{y} position of the source by inverting the equation of the lens. To better understand the process we consider the lens equation for a binary lens written in the following way:

$$\vec{y} = \vec{x} - \frac{1}{1+q} \frac{\vec{x} - \vec{x}_a}{|\vec{x} - \vec{x}_a|^2} - \frac{q}{1+q} \frac{\vec{x} - \vec{x}_b}{|\vec{x} - \vec{x}_b|^2} \quad (2.2)$$

where the two masses are written in terms of q . In the binary lens case we know that the number of images can be 1 or 3 when the source lies outside the caustics and 1 or 5 otherwise. Let I be the index spanning the number of images and n the number of points on the boundary indexed by i . The total area of the images is [57]:

$$A = \sum_I p_I \sum_{i=0}^{n-1} \vec{x}_{I,i} \wedge \vec{x}_{I,i+1} + \frac{1}{24} [(\vec{x}'_{I,i} \wedge \vec{x}''_{I,i}) + (\vec{x}'_{I,i+1} \wedge \vec{x}''_{I,i+1})] \Delta \theta^3 \quad (2.3)$$

where p_I is the parity of the images and the last term of (2.3) indicates the parabolic correction.

Limb Darkening

The contour integration does not include automatically the limb darkening. Following the work of Bozza 2010 [57] in order to do this we can divide the source into concentric uniform discs with radius ρ_i where i indicates a single disk and calculate their magnification. Introducing \bar{I} as the average surface brightness and $r = \rho/\rho_*$ the brightness profile can be described by a linear-darkening law $I(\rho) = \bar{I}f(r)$ [58] where:

$$f(r) = \frac{1}{1 - (a/3)} [1 - a(1 - \sqrt{1 - r^2})] \quad (2.4)$$

2. MODELLING A MICROLENSING EVENT

The contribution of each annulus with an inner radius ρ_{i-1} and outer radius ρ_i is:

$$I = \bar{I}\rho_*^2 F(r) \int_0^{2\pi} d\theta \mu(r, \theta) = \bar{I}\rho_*^2 \int_{r_{i-1}}^{r_i} r f(r) dr \int_0^{2\pi} d\theta \mu(r, \theta) \quad (2.5)$$

where $F(r) = 2 \int_0^r dr' r' f(r')$ is the cumulative function, $r_i = \rho_i/\rho_*$ and $\mu(r, \theta)$ is the point-source magnification factor. The limb-darkened magnification factor will be given by Eq. (2.5) divided by the original source flux $\bar{I}\pi\rho_*^2$

$$M = \frac{1}{\pi} \int_{r_{i-1}}^{r_i} r f(r) dr \int_0^{2\pi} d\theta \mu(r, \theta) \quad (2.6)$$

With the contour integration it is possible to estimate μ_i for a uniform disc of radius ρ_i :

$$\mu_i = \frac{1}{\pi r_i^2} \int_0^{r_i} r dr \int_0^{2\pi} d\theta \mu(r, \theta) \quad (2.7)$$

2.3 Modelling

2.3.1 VBBinaryLensing

After having seen the main protagonists of the microlensing observation campaigns and the main methods for calculating the light curves, the modeling of a microlensing event is now proposed. The starting point in the analyses carried out and presented in this work is the RTModel platform, based on VBBinaryLensing codes [57] [59] [21]. The main goal of an analysis of a microlensing event is to find the best model that fits the light curve in the best way. In order to find it we use the χ^2 as indicator. Indeed the minimization of χ^2 is the most important process to find the best model.

The VBBinaryLensing codes form the core of the modeling of the microlensing events presented in this thesis work. The lightcurve calculation is computed with the contour integration explained above. In the version 2.0 of this code [59] new upgrades are introduced and in version 3.0 also astrometric microlensing is included [21].

Finite source effects

A problem that arises from the computation of the lightcurve is when to use the point-like source or the finite source. In order to solve this problem VBBinaryLensing builds a sort of test where the plane of the source is divided into two sections, one where the source is treated as a point source and the other as a finite source, obtaining a magnification for both cases μ_p for the point source and μ_f for the other case. The condition of point source is satisfied if we have:

$$|\mu_f - \mu_p| < \delta \tag{2.8}$$

where delta is the required accuracy goal of the computation. In order to check this condition we have to look at the value of angular radius of the source ρ_* : if this parameter is very small we can consider the point-like treatment, otherwise for larger source we use the finite treatment. The limb darkening should also be included for completeness and the following condition would be obtained $|\mu_{f,LD} - \mu_p| \leq |\mu_f - \mu_p|$ but wanting to have a simpler and faster resolution, the uniform case is considered and limb darkening is introduced in successive steps [59].

Quadrupole test

Assuming $\delta \ll 1$ we expand the μ_f in terms of μ_p , ρ_* and σ [60] to see where the point source approximation fails:

$$\mu_f = \mu_p + \frac{\rho_*^2}{8} \Delta \mu_p + \frac{\rho_*^4}{192} \Delta \Delta \mu_p + o(\rho_*^4) \tag{2.9}$$

where $\Delta = \partial_{y_1} \partial_{y_1} + \partial_{y_2} \partial_{y_2}$ is the Laplacian operator. The term with ρ_*^2 is called quadrupole while that with ρ_*^4 is called hexadecapole. Using the complex notation where the images are described by $z_I = x_1 + ix_2$ the magnification for a point-source can be written in terms of the Jacobian:

$$\mu_p = \sum_I \frac{1}{|J(z_I)|} \tag{2.10}$$

2. MODELLING A MICROLENSING EVENT

where $J(z_I) = 1 - f(z)'f(\bar{z})'$ and $f(z) = -m_1/(z - s) - m_2/z$. Putting this definition into 2.9 we can define the quadrupole term as first correction for each image I :

$$\mu_Q = -\frac{2\text{Re}[3\bar{f}^3 f''^2 - (3 - 3J + J^2/2)|f''|^2 + J\bar{f}^2 f''']}{J^5} \rho_*^2 \quad (2.11)$$

where J is obtained from point-source magnification calculation and f is a rational function which can be calculated easily. In this way the condition to use the finite source approximation is:

$$\sum_I c_I |\mu_Q| < \sigma \quad (2.12)$$

where c_I is chosen empirically. But this is not enough, because another corrective term must be added which takes into account the regions near the cusps:

$$\mu_c = \frac{6\text{Im}[3\bar{f}^3 f''^2]}{J^5} \rho_*^2 \quad (2.13)$$

so that the total correction becomes:

$$\sum_I c |\mu_{qI} + \mu_{cI}| < \sigma \quad (2.14)$$

Ghost image test

When we have a binary lens we can have the formation of 3 or 5 images. This depends on the source position with respect to the caustic configuration and it must be considered in the computation. In fact when the source crosses a fold in the lightcurve there is a discontinuous slope change that corresponds to the creation of a new pair of images making the Eq. (2.14) useful only if the source is inside the caustic. In order to solve this VBBinaryLensing introduce the ghost image test where we expand the Jacobian in the position of the ghost images z_G [59]:

$$J(z) = J(z_G) + \frac{\partial J}{\partial z} dz + \frac{\partial J}{\partial \bar{z}} d\bar{z} \quad (2.15)$$

2. MODELLING A MICROLENSING EVENT

If we have a shift from the source center by a quantity $s\zeta = \rho_* e^{i\phi}$ also the ghost images will have a shift which satisfies the following equations:

$$\begin{aligned}\zeta &= z_G + f(\hat{z}) \\ \hat{z} &= \bar{\zeta} - f(z_G)\end{aligned}\tag{2.16}$$

For the real images $\hat{z} = \bar{z}$ but for the ghost image we must consider the conjugate separately. So modifying the Jacobian as $\hat{J} = 1 - f'(z_G)f'(\bar{z})$ (that becomes the original J when $\hat{z} = \bar{z}_G$). In conclusion the condition that states if we can work in the regime of point source or in the finite source is:

$$\frac{1}{2} \left| J(z_G) \frac{\hat{J}^2}{\hat{J}f''(\bar{z}_G)f'(z_G) - \bar{\hat{J}}f''(z_G)f'(\bar{z}_G)f'(\hat{z})} \right| > c_G \rho_* \tag{2.17}$$

Here c_G is a coefficient set empirically. If the left-hand side member (that represents the estimated distance needed to send the ghost image in the critical point in the source plane) is larger than ρ_* then we can use the point-source approximation since we are far from the fold, otherwise we use the finite-source approximation. This test must be made separately for each ghost image.

Planetary test

Everything we have seen so far works well for large binary caustics but may have problems if you have planetary caustics that have small size. This problems can be solved if we check that the distance from the centre of the source to the center of the planetary caustic is greater than ρ_* [59]:

$$|\zeta - \zeta_p|^2 > c_p(\rho_*^2 + \Delta_p^2) \tag{2.18}$$

where c_p is another empirical term and $\Delta_p = 3\sqrt{q}/s$ represents the extension of the caustic (both in the close and wide regime) [61], [62].

High order effects: parallax, satellites, orbital motion and xallarap

In the simplest case of binary lens we assume the static configuration where the two lenses are fixed and the motion of the source is rectilinear.

2. MODELLING A MICROLENSING EVENT

However this assumption is acceptable if the duration of the event is short. Otherwise we must take in account the high order effects. This can be made in `VBinaryLensing` with several functions. Parallax can be included with the addition of two parameters π_1 and π_2 . In this case the Earth orbit is calculated using the JPL approximate ephemeris formulae and the user can choose between the north-east reference and the parallel-perpendicular frame. Moreover it is possible to include the satellite parallax. Concerning orbital motion we can include it with the addition of three parameters $(\gamma_{\parallel}, \gamma_{\perp}, \gamma_z)$ that describe the orbit of the two lenses with the assumption of circular motion [20]. In addition to this we can compute the lightcurve also for the binary source, in particular with the inclusion of the xallarap effect, with the addition of five parameters $(i, \phi, \omega, \xi_{\parallel}, \xi_{\perp})$ following the work of Rahvar and Dominik [24]. In addition to this we include also the mass ratio between the two sources (further explanations will be given in the next chapter).

2.3.2 RTModel

Modelling a microlensing event is complex and requires time, and fast computation since every event is characterized by a large number of data and parameters. The main goal is to find the best χ^2 . In order to do this the platform `RTModel`¹ can help us since it has the ability to perform a modelling in real time, since it works with `ARTEMIS` (Automated Robotic Terrestrial Exoplanet Microlensing Search) [63] that gives an alert for a microlensing event that is ongoing sending the data in real time to `RTModel`, which can start modeling right away. The computation of `RTModel` is based on the `VBinaryLensing` codes.

2.3.3 Levenberg-Marquardt algorithm

The modeling of a microlensing event is developed starting from the Levenberg-Marquardt algorithm (LMA), a useful method used for the

¹<http://www.fisica.unisa.it/gravitationastrophysics/RTModel.htm>

2. MODELLING A MICROLENSING EVENT

resolution of non-linear least squares problems during the minimization processes when we have a large number of parameters. It is based on the gradient descent method and the Gauss-Newton algorithm.

In order to explain how it works we define the model function $f(x, t)$ where x are the n parameters of the model and t is an independent variable. Now we consider a dataset of N points $y(t_i)$ (where $i = 0, 1, \dots, N$) with their respective errors σ_{y_i} . The sum of the difference between each points with the values obtained by the model weighted by the error defines the χ^2 :

$$\chi^2 = \sum_{i=1}^N \left(\frac{y(t_i) - f(x, t_i)}{\sigma_{y_i}} \right)^2 \quad (2.19)$$

Defining the weighting matrix $W = 1/\sigma_i^2$ the χ^2 can be written as [64]:

$$\chi^2 = y^T W y - 2y^T W f + f^T W f \quad (2.20)$$

Gradient descent method

Widely used in the field of machine learning, the gradient descent method is an optimization algorithm for finding local minimum of a differentiable function. It is based on the update of parameter values in the downhill direction i.e. the direction opposite to the gradient of $f(x, t)$. We can calculate the gradient of χ^2 with respect to the function of the model as:

$$\begin{aligned} \frac{\partial \chi^2}{\partial x} &= 2(y - f(x, t))^T W \frac{\partial (y - f(x, t))}{\partial x} \\ &= -2(y - f(x, t))^T W \frac{\partial f(x, t)}{\partial x} \\ &= -2(y - f(x, t))^T W J \end{aligned} \quad (2.21)$$

where $J = \partial f(x, t)/\partial x$ is the Jacobian of the matrix $n \times N$ of the partial derivatives of f respect to x . We introduce a parameter h that moves the parameters in the direction of steepest descent as:

$$h = \alpha J^T W (y - f(x, t)) \quad (2.22)$$

where α is a scalar that adjusts the length of the step.

Gauss-Newton method

This method is used for minimizing a sum-of-squares function [64]. The first step is to approximate locally the function f with a first-order Taylor expansion:

$$f(x + h, t) \approx f(x, t) + \frac{\partial f}{\partial x} h = f + Jh \quad (2.23)$$

If we put this result in (2.20) we have:

$$\chi^2(x + h) \simeq y^T W y + f^T W f - 2y^T W f - 2(y - f) W J h + h^T J^T W J h \quad (2.24)$$

Setting $\partial\chi^2/\partial h = 0$ allows us to find the value of h :

$$\frac{\partial\chi^2(x + h, t)}{\partial h} \approx -2(y - f)^T W J h + 2h^T J^T W J \quad (2.25)$$

In this way we obtain the Gauss-Newton equations:

$$[J^T W J] h = J^T W (y - f) \quad (2.26)$$

The Levenberg-Marquardt method

Starting from the (2.26) we introduce the damping parameter λ .

$$[J^T W J + \lambda I] h = J^T W (y - f) \quad (2.27)$$

λ it is initialized to large values so that the first steps are small. If in one step we have $\chi^2(f + h) > \chi^2(f)$ then λ is increased, otherwise is decreased and the scaling of the parameter is given by:

$$[J^T W J + \lambda \text{diag}(J^T W J)] h = J^T W (y - f) \quad (2.28)$$

Depending on whether the λ value is large or small, we will switch from the gradient descent method to the Gauss-Newton method.

2.3.4 Markov Chain

After the use of the Levenberg-Marquardt algorithm to minimize the χ^2 another step is necessary in order to find the best models of a microlensing model. The method that we use is a stochastic process and in particular we adopt the Markov Chain Monte Carlo process. The particularity of this process is that the evolution depends only on the previous state, without taking into account everything that was there previously. We consider a set of parameters \vec{x} with dimension $n \in N$ on a state space S and we have the condition of stochastic process, where the transition from the state $n - 1$ to the state n is given by (here the time is represented by n and we are treating discrete-time processes) [65]:

$$Px_n = i_n | x_{n-1} = i_{n-1}, \dots, x_0 = i_0 = Px_n = i_n | x_{n-1} = i_{n-1} \quad (2.29)$$

for every $i_n \in S$. Introducing the stochastic matrix W_{ij} we can evaluate the probability of transition from a state i at the time t to a state j at the time $t + 1$ as:

$$P\{x_{t+1} = j | x_t = i\} = W_{ij} \quad (2.30)$$

Let us see the properties of this matrix. First of all the elements are non-negative (they represent probabilities). Moreover $\sum_j W_{ij} = 1 \forall i$. Now we express the conditioned probability for the two states i and j at the time t and $t + 1$ respectively as:

$$p_j(t + 1) = \sum_i W_{ij} p_i(t) \quad (2.31)$$

For this purpose we are considering the Chapman-Kolmogorov equations that relates the probability distribution of two different sets of coordinates, during a stochastic process. We can use the (2.31) to iterate the process, obtaining:

$$p_j(t) = \sum_i W_{ij}^t p_j(0) \quad (2.32)$$

2. MODELLING A MICROLENSING EVENT

where the stochastic matrix at the time (or jump) t is calculated as $W_{ij}^t = \sum_k W_{ik}^{t-1} W_{kj}$.

We apply the Markov Chain Monte Carlo process for the exploration of parameters space in order to find the final (and hopefully best model). The starting point is the model obtained by the Levenberg-Marquardt algorithm and with the Markov Chain Monte Carlo process we get, step by step, in a new configuration with a better χ^2 . The computation is performed according to some global parameters. The first is the number of steps of the chain. The higher is the number of steps the better will be the exploration in the parameters space. The second quantity is the radius that is related to the temperature, the third quantity that describes how large the region of exploration is. Larger values of the temperatures allow to explore far from the starting point in the parameter space and we can reach other minima, while for lower values of the temperature there will be little step very near from the starting point. These two parameters are important for the definition of the acceptance, that give us the probability that we have a jump during the Markov process.

Let us see the computation in deeper detail. We consider \vec{x}_k the k -element of the chain. The next element will be x_{k+1} that can be x_k (no jump) or a new quantity \hat{x} . This will be determined by the following probability that defines the acceptance:

$$P = e^{-\frac{1}{2} \frac{\chi^2(\hat{x}) - \chi^2(\vec{x}_k)}{T}} \quad (2.33)$$

In this way, if the $\chi^2(\hat{x}) < \chi^2(\vec{x}_k)$ the chain will accept the new point $\vec{x}_{k+1} = \hat{x}$. Otherwise, the new point will be accepted with some probability $0 < P < 1$. If the new point is not accepted, the chain will remain in the same point for one more step: $\vec{x}_{k+1} = \vec{x}_k$. We can note how the probability is modulated by the temperature T . Indeed, if we want to explore regions far from the starting point we put high values for T alleviating the effect of big sky differences. As we will see soon to explore wide regions it is important to

2. MODELLING A MICROLENSING EVENT

set a suitable radius value. An important question arises: how to define the \hat{x} . To solve this problem we consider the curvature matrix $C_{ij} = \partial f / \partial q_i \partial f / \partial q_j$ where f is the model and q_i are the parameters. The matrix has dimension $m \times m$ where m is the total number of parameters. The next step is the diagonalization of this matrix which gives us the eigenvalues λ_i and the eigenvectors \vec{v}_i . It is emphasized that these eigenvalues and eigenvectors are obtained from the first element of the chain, i.e. the model that comes out of the Levenberg-Marquardt algorithm and are no longer changed during the Markov process. These eigenvectors will be located in the parameter space with a certain orientation (they do not coincide with the parameter axes). Now we define a box in the parameter space centered at the origin where every edge in this m -dimensional space lies on every eigenvector \vec{v}_i with length $1/\lambda_i$. At this point we choose \hat{x} as:

$$\hat{x} = \vec{x}_k + \sum_{i=1}^m \mu_i \frac{\vec{v}_i}{|\vec{v}_i|} \frac{1}{\lambda_i} R \quad (2.34)$$

where μ_i is a random number in the range $[-1, +1]$ and R is the radius selected for the Markov Chain and makes explicit how far we actually go from the starting point in the parameter space. For small values of R it will always remain nearby while for high values we will go far from the starting point. For a good Markov process, it is important that for every steps, the acceptance ranges from 0.2 and 0.6 [66]. In this way at the end of the process we hope to obtain a smooth Gaussian-like distribution for every parameters. Otherwise a low acceptance gives a distribution with some isolated peaks while values of acceptance too high lead to a flat distribution. The Markov chain process adopted in addition to taking the model obtained from the Levenberg Marquardt algorithm also considers in the computation the limb darkening coefficients for each telescope if present.

CHAPTER 3

XALLARAP AS CONTAMINANT IN PLANETARY MICROLENSING: THE CASE OF MOA-2006-BLG-074

3.1 Motivations

In the most general case a microlensing event appears as a symmetric bell-shaped curve. If there is a second lens (planet or another star) we will see in the lightcurve additional peaks or dips depending on the geometry of the caustics. It is possible that the most common case of short duration additional peaks could be confused with the case of a secondary source suffering microlensing [22]. A binary source system should thus lead to the sum of two Paczynski curves, if both sources are luminous enough. Nevertheless, considering the orbital motion of the two sources we can have additional distortions to the light curve, with periodic modulations induced by the oscillatory motion of the two stars around the common center of mass [67]. The periods of binary systems may range from a few hours for very close systems to hundreds of years for widely spaced pairs. Furthermore, given the

3. XALLARAP AS CONTAMINANT IN PLANETARY MICROLENSING: THE CASE OF MOA-2006-BLG-074

steepness of the luminosity–mass relation, in most cases the secondary star might be much fainter than the primary, but its influence on the apparent trajectory of the source can be still present. For this reason, the binarity of the source may sometimes arise just from the perturbation of the motion of the primary without any signs of additional light. We also had examples of possible events observed by the EROS and MACHO projects with modulations induced by the orbital motion of the source around a hidden companion are in Palanque-Delabrouille et al. [68], Derue et al. [69], and Alcock et al. [23]. As said in the first chapter this effect is very similar to annual parallax ([70], [16]) arising from the orbital motion of the Earth around the Sun, save for the fact that it involves the other end of the line of sight. This is why it is commonly referred to as xallarap (i.e., the inverse of parallax). It was soon realized that the two effects may produce identical long-term perturbations if the duration of the event is short compared to the orbital period [71]. Indeed, for many microlensing events of interest, models with xallarap compete with models with parallax and cannot be excluded on the basis of physical arguments [72]–[77]. However, the combination of constraints from the third Kepler’s law with other information on the source may sometimes pinpoint the masses of the two components [78]. This may help rule out the xallarap model if the companion has a mass incompatible with the observed flux [79]–[81] unless it is a black hole. Furthermore, if a xallarap model returns a period of 1 year, there is a high chance that the fit has converged to a mirror solution of a parallax model [82], [83]. Nevertheless, binary stars are common around the Galaxy, with a multiplicity fraction around 40% [13], [84], which should be probably further increased for the stars in the bulge targeted by microlensing campaigns. Although most of these binaries are too wide to show any signatures in microlensing events, a systematic study of 22 long-duration events in the bulge showed that 23% of them were actually affected by xallarap [29]. Indeed, some planetary microlensing events require binary sources for a complete modeling of all deviations [85]–[87]. The contamination of xallarap in planetary microlensing events has been poorly investigated, but it is known

3. XALLARAP AS CONTAMINANT IN PLANETARY MICROLENSING: THE CASE OF MOA-2006-BLG-074

to exist [88]. The study of binary sources and their orbital motion may even provide new opportunities: it may help break degeneracies in microlensing [78] or it may open a new channel to discover planets orbiting around the source star [89]–[91]. Indeed, xallarap must be considered as a possible alternative before introducing additional bodies to explain the observed deviations [92] and reducing the time of computation of such events. The event analyzed in this chapter is MOA-2006-BLG-074, whose anomaly has been initially overlooked and only recently noticed in a retrospective analysis by the MOA collaboration. This event provides an enlightening example of a very promising planetary candidate that can be explained by the xallarap effect. Understanding events like this is important to develop methods to discriminate between the two cases in future automatic analysis pipelines running on large data sets.

3.2 Observations

The event was detected by the Microlensing Observations in Astrophysics (MOA; [93], [94]) at the following J2000 equatorial coordinates (R.A., decl.) = $(18^h05^m27^s.341, -31^\circ47'17''.68)$ corresponding to Galactic coordinates $(l, b) = (-0^\circ.316, -5^\circ.131)$. although data from many years of observation are available for the purpose of microlensing modeling it is sufficient to consider data within the 2006 season. In fact, the peak was reached on 2006 July 15 (HJD' ≈ 3931.64) and the full duration of the microlensing magnification is about 50 days, fully confined well within the season. For this event we have 738 data points in the MOA-R broadband, which spans across Johnson–Cousins–Bessell R and I bands. Unfortunately, no MOA-V data are available for this event, a fact that makes a color analysis of the source particularly difficult. In addition, there is no data from the Optical Gravitational Lensing Experiment [95], the other main survey active at the time of the event, because the event fell at the edge of the field. As usually adopted in the microlensing field [75] error bars are adjusted as $\sigma_i^2 = k\sqrt{\sigma_{i,orig}^2 + e_{min}^2}$ where e_{min} is fixed by requiring that the residuals are similar for high magnification and

3. XALLARAP AS CONTAMINANT IN PLANETARY MICROLENSING: THE CASE OF MOA-2006-BLG-074

low-magnification sections of the light curve, while k ensures that $\chi^2/d.o.f = 1$ for the best model.

3.3 Modeling

In Fig. 3.1 we see that the residuals of the observed light curve from such a model are evident in the peak and after the peak around $HJD \sim 3940$. The anomalies at the peak suggest the possibility that the central caustic is not point-like (denoted with $1L$ for this analysis) due to the distortion of a secondary lens. In the retrospective analysis carried by the MOA collaboration, MOA-2006-BLG-074 was independently identified as a possible planetary event using three different modeling codes (Bennett [96], Bozza [57], Sumi [85]). All of them give the same close binary model with a mass ratio of $q \sim 10^{-4}$, that, in principle, was identified as a promising planetary candidate. In order to explore the parameter space, we use the RTModel platform which is based on a template library approach [97]. The basic magnification calculation is performed by the VBBinaryLensing code [21], [57], [59]. With this approach, we find two planetary solutions with $s < 1$, and their corresponding wide duals with $s \rightarrow 1/s$ [98], [99]. Among these solutions, the best one plotted in Figure 3.1 and 3.2 as $2L$ is the wide one with the smaller separation. Its parameters, listed in 3.1 indicate a planet with $q \sim 10^{-4}$ in a nearly resonant configuration. As anticipated, the χ^2 of the binary lens model is much lower than that of the single-lens model. This is confirmed by the fact that the residuals around $HJD = 3940$ in Figure 3.1 are flattened. However, some residuals remain in the peak (see Figure 3.2). We also note that the alternative model with slightly wider separation flattens the residuals at the peak while leaving the deviation at $HJD = 3940$ untouched. The close duals of these two models have higher χ^2 and have a poorer performance. These residuals cannot be explained by a simple static binary lens so it is natural to think that high order effects (parallax and orbital motion) must be taken in account. Considering the orbital motion of the two lenses and using the parametrization described

3. XALLARAP AS CONTAMINANT IN PLANETARY MICROLENSING: THE CASE OF MOA-2006-BLG-074

in the first chapter following the works of Skowron [20] and Bozza [21] we use the three parameters describing the projected angular velocity γ_{\parallel} , γ_{\perp} and γ_z . With the assumption of circular orbital motion, these three parameters are sufficient to completely characterize the orbit and thus allow us to explore a subspace of possible physical solutions, as opposed to the two-parameter linear orbital motion. We refer to the binary model including the parallax effect and the circular orbital motion as model 2LO. In all the cases, the parameter space is significantly enlarged.

In order to lead the broadest exploration possible, we start from the static solution and minimize the χ^2 by a Levenberg–Marquardt run. After that, we start Markov chains at large temperatures and record all separate minima we find. For each of the minima we run chains at lower temperature until we single out the best solution. In the case of annual parallax, the symmetry of the model for reflection around the star–planet axis is broken and we have to consider possible reflections separately. As results of our search, we first note that all models with parallax and no orbital motion for the lens converge to unphysically large values of the parallax, with $\pi_E > 2$, which would imply a very close-by or very small lens. For this reason we discard such models and take this outcome as a suggestion that some motion with a shorter timescale is at work in this event.

A more satisfactory model (named 2LO in Figures 3.1, 3.2 and Table 3.1) is obtained when the lens orbital motion is included. The $\Delta\chi^2 = 136$ with respect to the static model 2L can be appreciated especially in the peak region visible in Figure 3.2. Some deviation is left on the left side at $HJD \sim 3917$. The parallax components of this model are poorly constrained and still compatible with zero at 1σ , which confirms that parallax is not the main motion to be considered here. The orbital motion has a zero γ_{\perp} component, which means that the planet orbit is seen edge-on. Note also that the value of $s < 1$ indicates that this model comes as the evolution of one of the static close models. However, the high value for γ_{\parallel} warns that the separation rapidly evolves from the close to the wide regime. This evolution is apparent

3. XALLARAP AS CONTAMINANT IN PLANETARY MICROLENSING: THE CASE OF MOA-2006-BLG-074

Table 3.1: Parameters for all models considered for MOA-2006-BLG-074, Credits [100]

	(Unit)	1L	2L	2LO	1L2SX
t_E	days	$40.12^{+0.55}_{-0.47}$	$39.84^{+0.46}_{-0.54}$	$40.86^{+1.05}_{-0.91}$	$33.29^{+0.31}_{-0.31}$
t_0	HJD	$3931.627^{+0.001}_{-0.002}$	$3931.627^{+0.002}_{-0.001}$	$3931.637^{+0.001}_{-0.006}$	$3931.610^{0.001}_{-0.002}$
u_0		$0.0102^{+0.0002}_{-0.0003}$	$0.0084^{+0.0003}_{-0.0002}$	$-0.0067^{+0.0004}_{-0.0005}$	$0.0091^{+0.0001}_{-0.0002}$
ρ_*		$0.01192^{+0.00026}_{-0.00043}$	$0.00942^{+0.00037}_{-0.00024}$	$0.00633^{+0.00110}_{-0.00041}$	$0.00985^{+0.00064}_{-0.00022}$
α		-	$3.133^{+0.001}_{-0.001}$	$-3.130^{+0.032}_{-0.005}$	-
s		-	$1.088^{+0.002}_{-0.001}$	$0.755^{+0.015}_{-0.011}$	-
q		-	$0.00014^{+0.00001}_{-0.00001}$	$0.00063^{+0.00005}_{-0.00013}$	-
$\pi_{E,N}$		-	-	$-0.473^{+1.053}_{-0.177}$	-
$\pi_{E,E}$		-	-	$0.323^{+0.069}_{-0.352}$	-
γ_{\parallel}	days ⁻¹	-	-	$0.0483^{+0.0030}_{-0.0020}$	-
γ_{\perp}	days ⁻¹	-	-	$-0.0060^{+0.0030}_{-0.0030}$	-
γ_z	days ⁻¹	-	-	$0.0389^{+0.0031}_{-0.0004}$	-
ξ_{\perp}		-	-	-	$0.0198^{+0.0018}_{-0.0017}$
ξ_{\parallel}		-	-	-	$0.0088^{+0.0007}_{-0.0001}$
ω	days ⁻¹	-	-	-	$0.442^{+0.001}_{-0.008}$
i		-	-	-	$-0.054^{+0.017}_{-0.049}$
ϕ		-	-	-	$4.493^{+0.630}_{-0.049}$
q_s		-	-	-	< 0.4498
R_{base}	mag	$-9.913^{+0.002}_{-0.003}$	$-9.921^{+0.003}_{-0.003}$	$-9.924^{+0.008}_{-0.003}$	$-9.937^{+0.009}_{-0.003}$
g		$0.647^{+0.022}_{-0.017}$	$0.710^{+0.020}_{-0.023}$	$0.782^{+0.051}_{-0.032}$	$0.422^{+0.026}_{-0.004}$
χ^2		1594.4	849.5	713.1	699.1

3. XALLARAP AS CONTAMINANT IN PLANETARY MICROLENSING: THE CASE OF MOA-2006-BLG-074

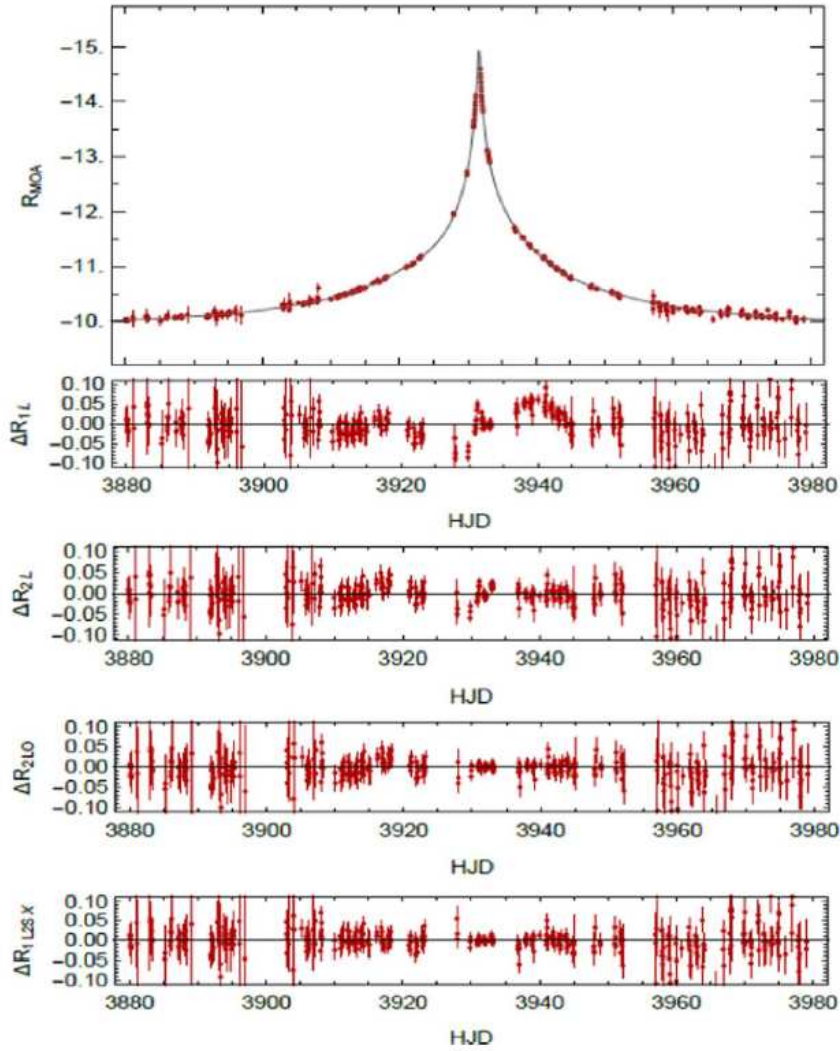


Figure 3.1: Light curve of MOA-2006-BLG-074 with the best model 1L2SX. We also show the residuals for the single-lens model 1L, the static binary lens model 2L, the binary lens model including orbital motion 2LO, the single lens binary source model 1L2SX, Credits [100]

in Figure 3.3 where we see that the caustic is still in the close topology when the source passes close to the central caustic. Soon after, the caustic becomes resonant and finally the planetary caustic detaches to the right. The impression is that in order to explain the peak anomaly together with the wing anomalies the caustic “follows” the source along its motion, which looks quite suspicious. In parallel with the binary lens model, we test an alternative direction to explain the anomalies seen in Figure 3.3. Instead of adding a second lens, we

3. XALLARAP AS CONTAMINANT IN PLANETARY MICROLENSING: THE CASE OF MOA-2006-BLG-074

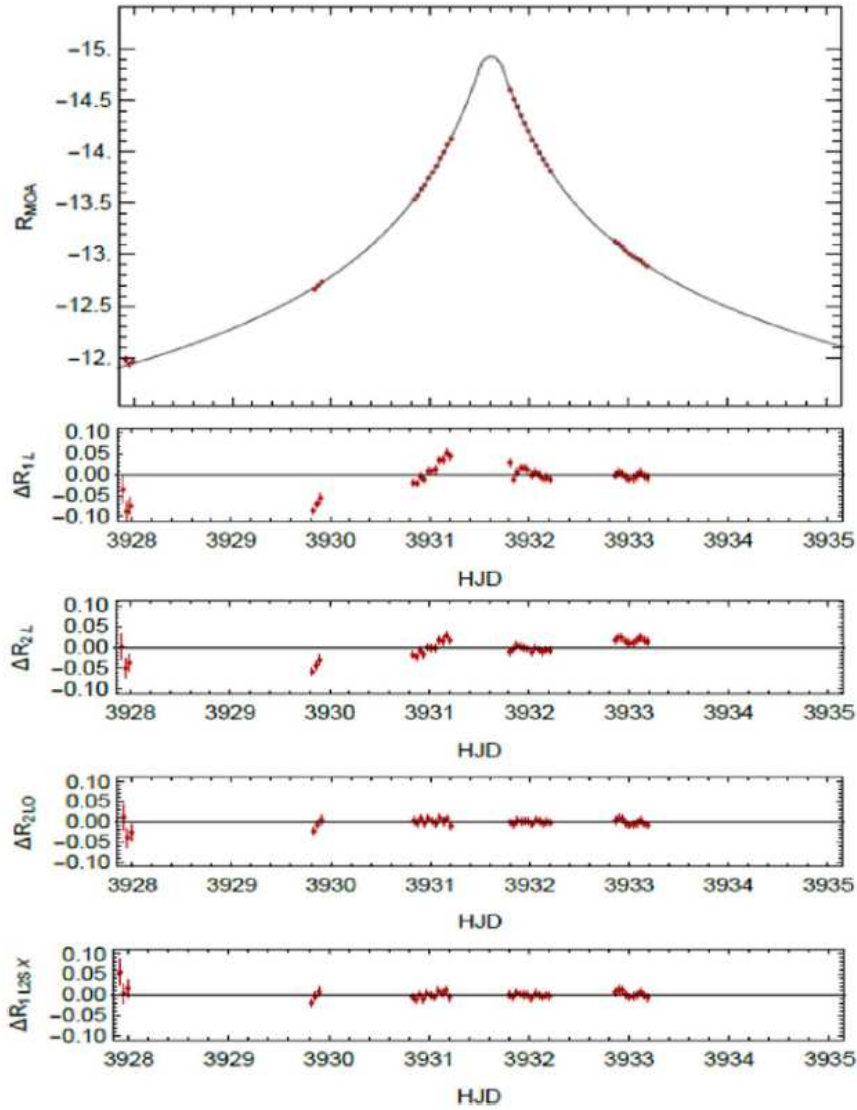


Figure 3.2: Zoom of the light curve of MOA-2006-BLG-074 with the best model. We also show the residuals for the single-lens model 1L, the static binary lens model 2L, the binary lens model including orbital motion 2LO, the single lens binary source model 1L2SX, Credits [100]

add a second source [22]. From the very beginning we include the orbital motion of the two sources around the common center of mass under the simplifying hypothesis of a circular trajectory. Therefore, in addition to the four parameters of the 1L model (t_E, t_0, u_0, ρ_*) we introduce five more parameters [24]: the inclination of the orbital plane i , the phase from the ascending node ϕ , the angular velocity ω and the two projections of the node

3. XALLARAP AS CONTAMINANT IN PLANETARY MICROLENSING: THE CASE OF MOA-2006-BLG-074

line parallel and perpendicular to the source velocity at time t_0 : ξ_{\parallel} and ξ_{\perp} , with the angular orbital radius being $\xi = \sqrt{\xi_{\parallel}^2 + \xi_{\perp}^2}$ in units of θ_E . Finally, we consider the possibility that the secondary source contributes to the observed flux. Therefore, we introduce the mass ratio q_s , of the secondary to the primary. For simplicity, we assume a power-law mass–luminosity relation $F_2 = F_* q_s^4$, and a mass-radius relation $\rho_2 = \rho_* q_s^{0.8}$ [101]. We will see that the results do not depend on the particular choice of these relations. We have started our search in the parameter space from the best single-lens-single-source model. The five orbital parameters have been set to zero in the initial condition, while q_s has been set to 0.1. Similarly to model *2LO*, we have run Markov chains with decreasing temperature, and branched different chains for independent provisional minima. At the end of our search, our best solution (labeled as *1L2SX*) improves the fit with respect to model *2LO* by $\Delta\chi^2 = 14$. This model represents the light curve plotted in Figures 3.1 and 3.2, which fits the peak region well, while performing much better on the wing anomalies. It is still too early to consider this model as the best, since that we must go through all possible checks that this solution is indeed physically acceptable. The orbit we find is nearly face-on with a period of $P = 14.2$. The orbital radius for the primary is $\xi = 0.022$ in units of the Einstein angle, which suggest that we are dealing with either a close binary system or a system in which the secondary is much lighter than the primary. Indeed, for the mass ratio we only find an upper limit $q_s < 0.422$, which indicates that the secondary basically intervenes through the reflex motion of the primary, while its contribution to the total flux is not essential. Also for this model we delay a full discussion of the physical constraints after the source analysis. The trajectories of the two sources are shown in Figure 3.4 where q_s is set to 0.33 (we will explain this choice later).

The orbital and xallarap models fit very well the observations. But before them we tried other models with not good results but that we still want to mention. First we consider a static triple-lens model *3L*. We have already mentioned that for a static binary model we have found two solutions with

3. XALLARAP AS CONTAMINANT IN PLANETARY MICROLENSING: THE CASE OF MOA-2006-BLG-074

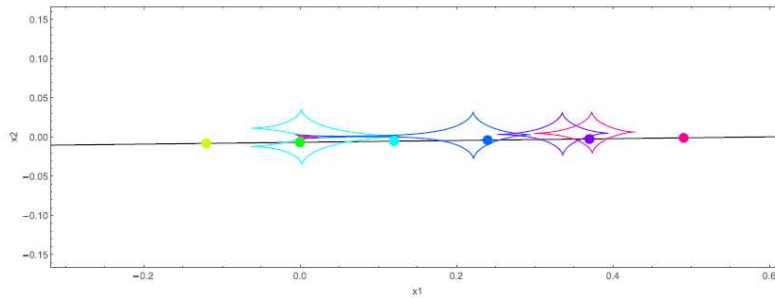


Figure 3.3: Caustic configuration for the binary orbital model $2LO$ presented in Table 3.1, with the source moving along the straight line from left to right. The green color refers to time t_0 , while other colors represent the source and caustics in time-steps of 5 days, Credits [100]

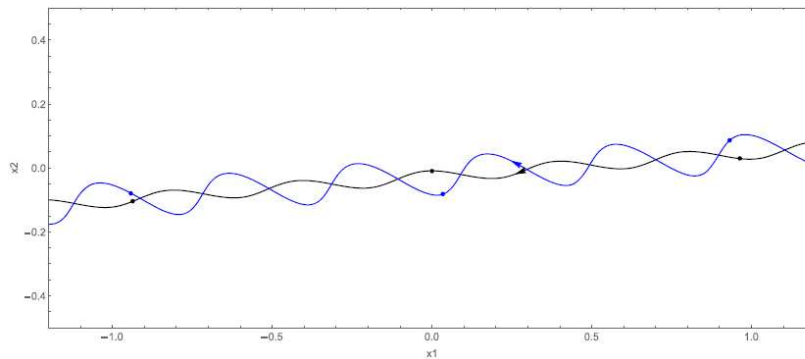


Figure 3.4: Trajectory of the primary source (black) and secondary source (blue) for the best model with one lens and two sources in Table 3.1 with a choice of the mass ratio $q_s = 0.33$. We have marked the positions of the sources at $t_0 - t_E, t_0, t_0 + t_E$, Credits [100]

a close-in planet and two solutions with a planet in a wide configuration. Therefore, we have considered having two planets in the system placed in two of the positions of these four different binary solutions, taking all six possible combination in account. The best of these is the configuration with both the planet in the wide case with a $\chi^2 = 729.4$ that is no better than $2LO$ so there is no reason to consider this model. Another possibility is that we have two sources and two lenses at the same time. Combining the parameters of $2L$ and $1L2SX$ we find a $\chi^2 = 674.9$ that is lower than the χ^2 of $1L2SX$ but is far below any conventional threshold in microlensing observations to

3. XALLARAP AS CONTAMINANT IN PLANETARY MICROLENSING: THE CASE OF MOA-2006-BLG-074

claim evidence of an additional body and can be explained by overfitting of systematics. Finally we tried to include the parallax in the *1L2SX* getting only a very modest improvement of the χ^2 .

3.4 Source Analysis

At this point we have to competitive models: *2LO* and *1L2SX*. We must discriminate between them on the basis of physical constraints. In order to do that, we can use the information on the source size, which is well constrained in both cases, to derive the size of the angular Einstein radius θ_E . We derive this quantity using the values of the model *1L2SX* indicating the values for *2LO* in round brackets.

The source size parameter is $\rho_* = 9.85 \times 10^{-3}$ (6.33×10^{-3}). In this case it is difficult find the Einstein angle because MOA observations are only available in the MOA-R band for this event, and no additional observations have been taken by other telescopes during the microlensing event. In Figure 3.5 we show a color-magnitude diagram for the MOA field including our microlensing event. The centroid of the red clump is at $R_{MOA,clump} = -11.120 \pm 0.009$ and $(V - R)_{MOA,clump} = 1.295 \pm 0.006$. The next step is the conversion from MOA bands to standard Johnson-Cousins bands using the cross-calibration with OGLE-III photometry [102] and deriving the following relations:

$$\begin{aligned} I_{OGLE} &= R_{MOA} + 28.206 - 0.217(V_{MOA} - R_{MOA}) \pm 0.002 \\ V_{OGLE} &= V_{MOA} + 28.510 - 0.146(V_{MOA} - R_{MOA}) \pm 0.002 \end{aligned} \quad (3.1)$$

From these we have $I_{OGLE,clump} = 16.805 \pm 0.009$ and $V_{OGLE,clump} = 18.496 \pm 0.011$. If we compare these quantities with the intrinsic red clump color $(V - I)_{clump,0} = 1.06 \pm 0.07$ [103] and the intrinsic magnitude $I_{clump,0} = 14.44 \pm 0.04$ [104] we obtain an extinction $A_I = 2.36 \pm 0.04$ and a reddening $E(V - I) = 0.63 \pm 0.07$. The blending parameter is $g = 0.421(0.782)$ and the baseline is $R_{base} = -9.931(-9.924)$. From this we can derive the source

3. XALLARAP AS CONTAMINANT IN PLANETARY MICROLENSING: THE CASE OF MOA-2006-BLG-074

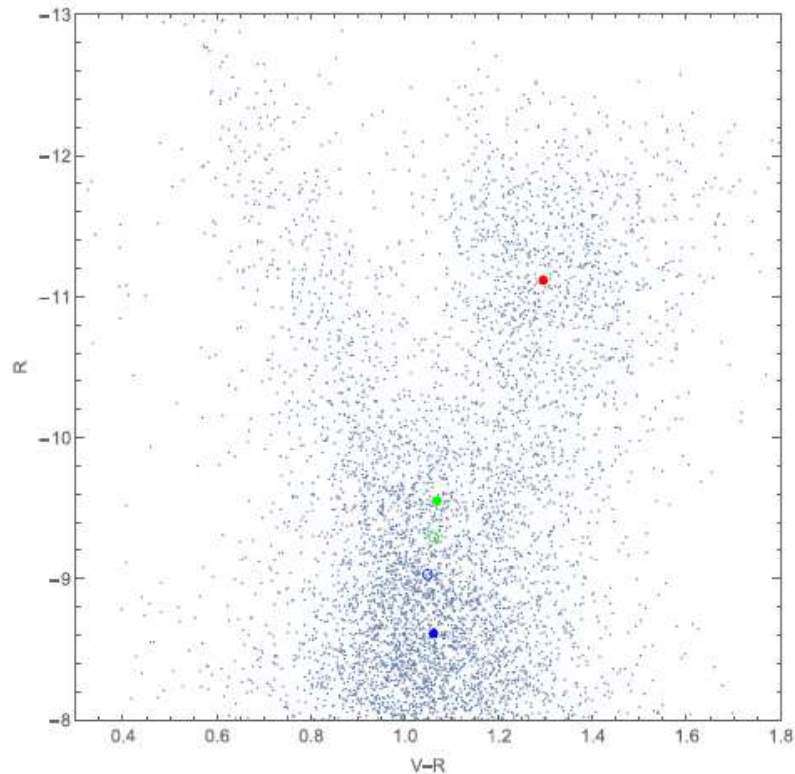


Figure 3.5: Color magnitude diagram (CMD) of the stars in the field of MOA-2006-BLG-074. The red dot shows the position of the red clump. The green dot represents the source star and the blue dot shows the blend position for model *1L2SX*. The empty circles represent the same objects for the *2LO* case, Credits [100]

magnitude $R_{MOA,*} = -9.549(-9.297) \pm 0.010$. Since there is no observation in MOA-V band we can make the following hypothesis: the levels $R_{MOA,*}$ for the two models correspond to the region of the turn-off point of the main sequence. The range of colors of the stars in the field is relatively narrow. So we assume that the source color can be represented by the average color of the stars in the field at $R_{MOA,*}$ with an uncertainty given by the rms. From these we get $V_{MOA,*} = -8.480(-8.235) \pm 0.164(0.155)$ and finally we have the magnitude in OGLE-III bands: $I_{OGLE,*} = 18.424(18.678) \pm 0.036(0.034)$ and $V_{OGLE,*} = 19.874(20.120) \pm 0.139(0.133)$ from which we have the de-reddened values for the source of $I_{OGLE,*0} = 16.064(16.318) \pm 0.054(0.052)$ and $V_{OGLE,*0} = 16.884(17.130) \pm 0.160(0.155)$. Using the Bessel & Brett

3. XALLARAP AS CONTAMINANT IN PLANETARY MICROLENSING: THE CASE OF MOA-2006-BLG-074

relations [105] we convert the color from $V - I$ to $V - K$ and with the empirical formula of Kervella [106] we obtain the angular radius of the source $\theta_* = 2.15(1.89) \pm 0.56(0.47) \mu as$. Once θ_* is obtained we can estimate the angular Einstein radius:

$$\theta_E = \frac{\theta_*}{\rho_*} = 0.22(0.30) \pm 0.06(0.10) mas \quad (3.2)$$

and consequently also the lens-source relative proper motion $\mu_{rel} = \theta_E/t_E = 2.40(2.67) \pm 0.26(0.28) mas yr^{-1}$. It must be considered the limb-darkening since we have a relevant value for the finite source effect. In order to estimate it correctly we proceed in the following way: first we take the value of $(V - I)_{OGLE} = 1.450$ and the magnitude $M_I = 3.96$ of the source. After this we compute the simulation of a stellar population with solar metallicity using IAC-STAR [107] with the stellar evolution library of Bertelli et al. [108] and the bolometric correction library of Castelli & Kurucz [109] and we derive $\log g = 4.31$ and $T_{eff} = 5625K$. Then we get the limb darkening coefficients in I and R band $a_I = 0.462$ and $a_R = 0.554$ and we take the mean value for the final limb darkening coefficient adopted since the R_{MOA} band cover the two bands almost equally.

3.5 Physical Constraints

Now we are able to derive the physical parameters of the system since we have obtained θ_E . Since we do not have a parallax measure in either models, we resort to a Bayesian analysis for the estimate of the mass and distance of the lens. We assume the galactic model of Dominik [110]. We will use the values measured of t_E and ρ_* to constrain the lens physical parameters. We also include the constraint from the lens flux, for which we use the mass–luminosity model of Castelli & Kurucz [109] to estimate the magnitude R_{MOA} of the lens and impose that it does not exceed the blend flux. For the source distance, the Galactic model predicts a modal value of $D_S = 9$ kpc that we use for the next part of the analysis which it will be divided in two part (one

for every model).

3.5.1 Constraint on the $2LO$ model

The posterior probability obtained for the $2LO$ model is shown in Figure 3.6 where we note a best value for the lens mass of $0.5M_{\odot}$.

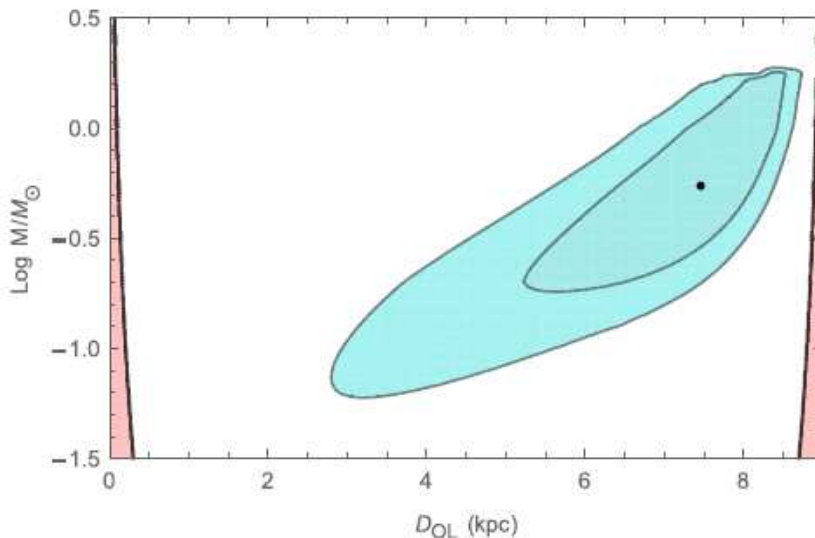


Figure 3.6: Allowed regions (in blue) in the plane $D_L(\text{kpc}) - \text{Log } M/M_{\odot}$ at 68% and 95% CL for the $2LO$ model. In red, the regions allowed by the Keplerian constraint, Credits [100]

To validate the orbital model it is necessary to take a further step: the mass and the distance to the lens must be compatible with the orbital period derived in our model. Following Skowron et al. [20], in order to have a bound system, the projected kinetic energy must be less than the projected potential energy:

$$\frac{v_{\perp}^2 r_{\perp}}{2GM} = \frac{(\gamma_{\perp}^2 + \gamma_{\parallel}^2) s^3 \theta_E^3 D_L^3}{2GM} < 1. \quad (3.3)$$

But as we can see in Figure 3.6 the only regions allowed are very near to the observer or the source and there is no overlapping with model. In conclusion we have to discard this model.

3.5.2 Constraints on 1L2SX model

The posterior probability for the 1L2SX model is shown in Figure 3.7 where we can note a lighter lens and even closer to the source with respect to the model 2LO. We derive $M_L = 0.38 \pm 0.23 M_\odot$, $D_{OL} = 7.9^{+0.6}_{-1.0}$ kpc. The lens has a 70% probability to be a bulge star rather than a disk star.

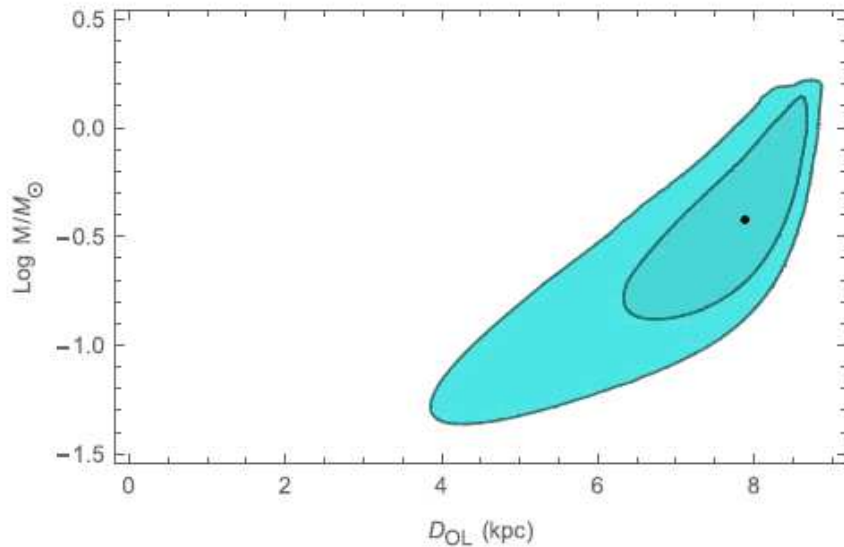


Figure 3.7: Allowed region in the plane $D_L(\text{kpc}) - \text{Log } M/M_\odot$ at 68% and 95% CL for model 1L2SX, Credits [100]

Using again the stellar libraries we are able to estimate also the source mass obtaining $M_S = 1.32 \pm 0.36 M_\odot$. Now we can test if the xallarap solution is compatible with the third Kepler's law [75], [78]. We introduce:

$$f_K(q_s, \xi, \omega) = K, \quad (3.4)$$

where:

$$f_K(q_s, \xi, \omega) = \log \left[\frac{\omega^2 \xi^3 (1 + q_s)}{q_s^3} \right], \quad (3.5)$$

$$K = \log \left[\frac{M_1 G}{(D_S \theta_E)^3} \right] = -14.16 \pm 0.90. \quad (3.6)$$

All quantities in f_K are fitting parameters of model 1L2SX, while the quantities in K have been estimated by use of the Galactic model and stellar

3. XALLARAP AS CONTAMINANT IN PLANETARY MICROLENSING: THE CASE OF MOA-2006-BLG-074

libraries. Only the models whose fitting parameters satisfy this constraint within the uncertainties can be considered as physically allowed.

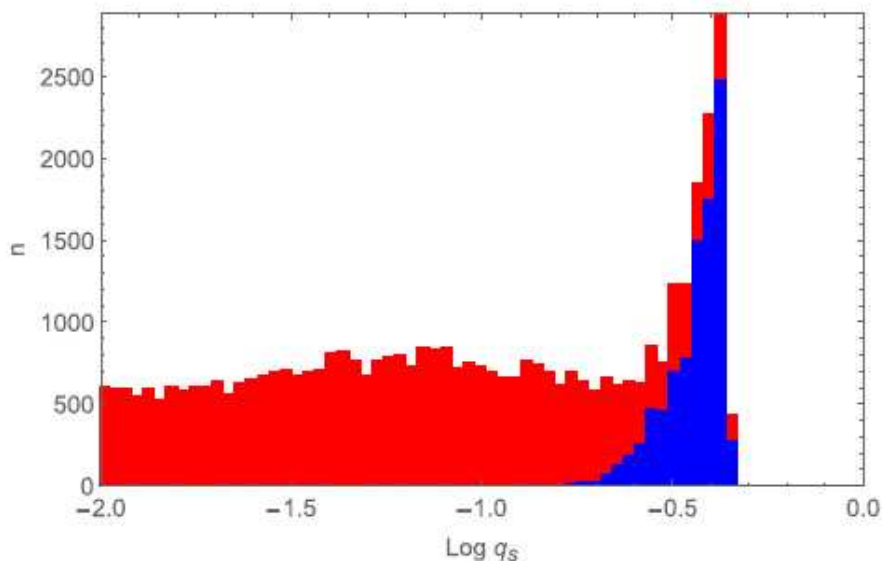


Figure 3.8: Distributions of the parameter $\log q_s$. The red histogram is obtained with a flat prior, while the blue one is the same distribution where each point in the Markov chain is weighted by the prior $P(q_s, \xi, \omega)$ in Eq. (3.7), Credits [100]

In Figure 3.8 it is represented the distributions for $\log q_s$ made in two ways: the first, in red, is generated by a Markov chain with a flat prior for this parameter, while the second, in blue is obtained weighting each point of the Markov chain by the following Gaussian prior

$$P(q_s, \xi, \omega) = \exp \left[-\frac{(f_K(q_s, \xi, \omega) - K)^2}{2\sigma_K^2} \right], \quad (3.7)$$

where σ_K is the uncertainty in the combination K . The red distribution is generally flat with a sharp peak on the right end for higher mass ratios before dropping to zero when the source becomes too luminous to be compatible with the observed light curve. We can see how the two peaks coincide, meaning that in both cases the same mass ratio is favored. Since the mass ratio only intervenes when the light of the secondary source becomes relevant, this can be interpreted as a marginal detection of the companion to the main source.

3. XALLARAP AS CONTAMINANT IN PLANETARY MICROLENSING: THE CASE OF MOA-2006-BLG-074

$D_L(kpc)$	$7.9_{-1.0}^{+0.6}$
$M_L(M_\odot)$	0.38 ± 0.23
$M_{S1}(M_\odot)$	1.32 ± 0.36
$M_{S2}(M_\odot)$	0.44 ± 0.14
$a(au)$	0.043 ± 0.012
$P(d)$	14.2 ± 0.2
$i(^{\circ})$	-3.0 ± 1.9

Table 3.2: Physical parameters for model 1L2SX, Credits [100]

Such detection is perfectly compatible with the Keplerian constraint derived from the properties of the primary source. The results obtained are shown in Table 3.2.

3.6 Discussion

In the retrospective analysis of MOA microlensing events a sizeable number of candidate planets has been found. For many of these events there are no additional observations that may complement the MOA data set. In particular for the event discussed in this chapter MOA-2006-BLG-074 there is only a single band observation. Nevertheless, modeling of the available photometry is possible and leads to interesting results that can be useful to drive this and future analyses in similar situations. This is a high-magnification event ($A \sim 110$) with an anomaly in the peak that in principle can be interpreted as the result of a central caustic perturbed by a small planet. High order effects must be considered since there are modulations on the wings but the orbital motion found is so fast that the Keplerian constraint for a bound system can only be fulfilled by a lens in the immediate neighborhood of the source. We consider another scenario: a binary source and a single lens. This configuration is able to explain the peak anomaly and the wing modulations with an orbital motion of 14 days. We obtain a lower χ^2 and a physically viable solution in which the primary is a star at the turn-off point of the main sequence

3. XALLARAP AS CONTAMINANT IN PLANETARY MICROLENSING: THE CASE OF MOA-2006-BLG-074

and the secondary is a K-M dwarf whose light may have been marginally detected. Observations in a second band would have been very useful to check for a color difference of the two sources. The lens is probably an M-dwarf in the bulge. In this case we have not discovered a new exoplanet despite three different modelling platform indicated it as such. Although binary sources have long been studied as possible contaminants in planetary microlensing searches, they are often overlooked in real-time modeling or in the selection process from large data sets. It is important to consider this contamination with the advent of the Roman Galactic Exoplanet Survey [51] since it has never been seriously estimated. This because we do not really know the precise fraction of binary and multiple systems. But it is very important to check how often the planetary signal can be mimicked by a binary source. In some cases the signal leads to an exoplanet [111] but in other cases the result can be similar to that found in this work [112], [113]. It can be possible to distinguish between the two cases if we have multiband observations with high enough cadence, since it is helpful to have a color constraint during the (sometimes short) anomalies, so we do not expect that this issue would significantly affect the current predictions of the exoplanetary yield from Roman. Nevertheless, it would be interesting to clarify and quantify this contamination with a dedicated investigation.

CHAPTER 4

PRECISION MEASUREMENT OF A BROWN DWARF MASS IN A BINARY SYSTEM: THE CASE OF OGLE-2019-BLG-0033

4.1 Motivations

Brown dwarfs (BDs) are still poorly understood objects.. A first reason is their low brightness which makes them difficult to detect and second their mass is lower than that of stars. The minimum mass needed to trigger hydrogen burning in the core corresponds to $0.078 M_{\odot}$ at solar metallicity [114] and it is the upper limit for the BDs that may still burn deuterium for a short period [115]. The distinction with the planets it is not really clear; we know that the deuterium-burning limit is of $0.013 M_{\odot}$ [116] but its impact is very small on the global properties and evolution of these substellar objects. The formation of BDs may occur via the instability and collapse of gas clouds with the same Jeans mechanism that generates stars [117] but it does not work at

4. PRECISION MEASUREMENT OF A BROWN DWARF MASS IN A BINARY SYSTEM: THE CASE OF OGLE-2019-BLG-0033

low masses excluding a fraction of BDs observed [118], [119]. Furthermore we can have bigger planets formed by core accretion that may exceed the above-mentioned planet-BD threshold and be classified as BDs [120], [121]. A lack of transits of these objects has been detected in Kepler's observational campaigns just as there are no companions around Sun-like stars and this can hint at some migration or instability mechanism depleting planetary systems of overly massive objects [122]–[124]. The difficulty in their observation lies in the fact that they are dim objects that can be detected when they are young and hot [125], [126]. In principle BDs can be detected in the infrared [127], [128] but there have also been discoveries of BDs in radio [129]. Spectroscopic observations in systems with red dwarfs are too difficult since these objects are too faint [130].

Microensing does not rely on the luminosity of the lenses and can be a precious technique to detect such substellar objects. Based on recent studies, the majority of the lens population is considered to be made up of low-mass stars or possibly BDs and even rogue planets [131]–[135]. In this respect with microensing we are able to define the mass function throughout our Galaxy in the low end [136]. A problem can arise considering the degeneracies that in general can be broken with high order effects. Indeed there are discoveries of this type of object thanks to microensing [137], [138]. The first isolated BD discovered by microensing was OGLE-2007-BLG-224 [139] while often they are revealed in binary systems [140], [141]. It can happen to find a binary system composed by two BDs [142] or of a planet orbiting around a BD [73]. During the years the number of BD discovered is increasing, but of particular note are those discoveries with very precise mass measurements, with a better than 10% accuracy [79], [139], [141]–[143] including the analysis presented in this chapter.

4. PRECISION MEASUREMENT OF A BROWN DWARF MASS IN A BINARY SYSTEM: THE CASE OF OGLE-2019-BLG-0033

4.2 Observations

The microlensing event OGLE-2019-BLG-0033/MOA-2019-BLG-035 was announced by the OGLE collaboration at the beginning of the 2019 bulge season on February 19 and independently found by MOA four days later. Its equatorial coordinates (J200) are: $RA = 18 : 08 : 38.26$, $Dec = -30 : 03 : 38.7$ corresponding to Galactic coordinates $l = 1.53^\circ$, $b = -4.90^\circ$. The lightcurve is shown in Figure 4.1 with all the observation taken from the ground telescopes and from Spitzer. The OGLE observations were carried out with the 1.3 m Warsaw Telescope at Las Campanas Observatory, Chile (see Section 2.1.1 for more details) using the I -band filter with an exposure time of 100 s. Occasionally observations in V -band were taken for color information. The event is located in the BLG521 OGLE field which was observed with an average cadence of less than one observation per night. Photometry of OGLE-2019-BLG-0033 was derived using the standard OGLE photometric pipeline [34], based on difference image analysis implementation by [144]. Instead the MOA collaboration is carrying out a high cadence microlensing survey with a 1.8-m MOA-II telescope at Mt. John University Observatory in New Zealand (see Section 2.1.2 for more details). The filter used is the MOA-Red filter and the images were reduced with MOA’s implementation [93] of the difference image analysis (DIA) method [145]–[147]. The systematic errors for MOA were de-trended considering correlations with the airmass and the seeing as well as the motion of a nearby possibly unresolved star [148]. This event was selected for Spitzer observations on 2019 May 10 at UT 04:11 ($HJD' = HJD - 2400000 = 8613.67$) as a ”subjective, immediate” target with an ”objective” cadence with roughly one observation per day starting in Week 2 of the 2019 Spitzer campaign using the $3.6 \mu\text{m}$ (L -band) channel of the IRAC camera. Each observation consisted of six dithered exposures. Because the target was very bright, the first ten epochs were taken with 12s exposures. Then, 30s exposures were used after $HJD' = 8692$ once it was established that the target would not be saturated as seen from Spitzer. The

4. PRECISION MEASUREMENT OF A BROWN DWARF MASS IN A BINARY SYSTEM: THE CASE OF OGLE-2019-BLG-0033

Spitzer data were reduced using the photometry pipeline developed by Calchi Novati [31] for IRAC data in crowded fields.

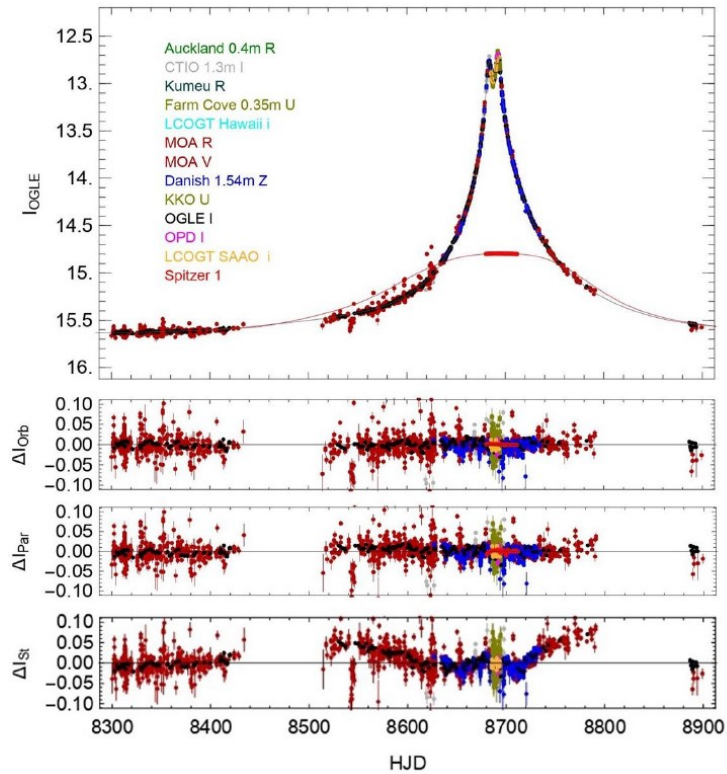


Figure 4.1: Light curve of the event OGLE-2019-BLG-0033 showing all observations from different telescopes as described in the text. The black curve is the best microlensing model for ground observers, and the red curve is the best model for Spitzer observations, as described in Section 3. In the bottom panel, we show the residuals from several models: best model including the parallax and orbital motion, best model with parallax without orbital motion, and best static model without parallax., Credits [149]

For this event follow-up observations were particularly useful. There were observations in *I*-band and *H*-band by μ FUN using the SMARTS Cerro Tololo 1.3m telescope (CT13) in Chile. They used these two bands in order to measure the color of the source but starting from $HJD' = 8666$ this event was added to a group of events followed at a higher cadence in order to increase the sensitivity to small planets and so this follow-up took a couple

4. PRECISION MEASUREMENT OF A BROWN DWARF MASS IN A BINARY SYSTEM: THE CASE OF OGLE-2019-BLG-0033

of observations per night sending an anomaly alert at UT 17:09. In addition, there are more observations from μ FUN with the Auckland Observatory (AO), Farm Cove Observatory (FCO), and Kumeu Observatory in New Zealand where the first and the last used R filter while the second did the observations without filter. Other observations made without filter were taken by the Klein Karoo Observatory in South Africa and from the Observatorio do Pico dos Dias (OPD) we have observations in i band. The data reduction were made using the DoPHOT pipeline [150]

Through the 0.4m telescope at the South African Astronomical Observatory (SAAO) in South Africa and the Haleakala Observatory in Hawaii (FTN) the Las Cumbres Observatory (LCO) global network conducted several observations. In this case data were reduced using a custom DIA pipeline [151] based on the ISIS package [146], [147].

Finally there are also data collected from the MiNDSTEp collaboration using the Danish 1.54m telescope at ESO La Silla Observatory in Chile for the microlensing follow-up program [152]. The telescope is equipped with a multiband EMCCD [153] providing shifted and co-added images in its custom red and visual passbands. This work utilizes red band time-series photometry which was reduced with a modified version of DANDIA [154], [155].

4.3 Modeling

In Figure 4.2 the zoom of the double peak is shown occurring at moderate magnification ($A_{max} \simeq 15$). This structure indicates that the central caustic generated by the lens has a typical astroid shape, which may arise either for close binary lenses or for a lens perturbed by a wide companion [15], [62]. This caustic is shown in Figure 4.3 for the best models, with a zoom-in shown in Figure 4.4.

4. PRECISION MEASUREMENT OF A BROWN DWARF MASS IN A BINARY SYSTEM: THE CASE OF OGLE-2019-BLG-0033

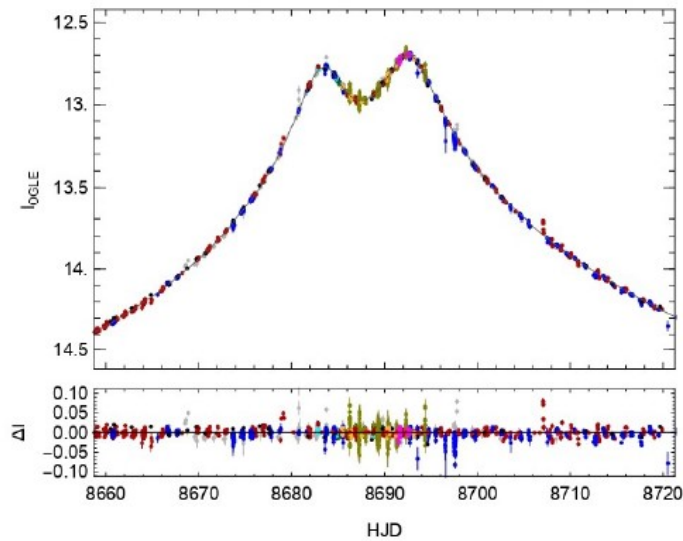


Figure 4.2: Zoom on the double-peak region of the light curve. The color coding for the observations is the same as in Figure 4.1, Credits [149]

4.3.1 Detailed modeling procedure

From Spitzer we have 29 data points spanning 32 nights. These observations are around the peak of the magnification as seen from the ground observations and are very far from the baseline. Without a baseline, Spitzer observations for this event must be complemented by a flux constraint to be included in the analysis [31]. In this analysis we try to obtain the microlensing parameters considering, at first, only the ground data. Then we use the flux constraint on Spitzer data and we compare it with the measured flux, in order to infer the geometry of the event as seen from the satellite alone. In this way we obtain an independent estimate of the parallax that we can compare with the ground-only measurement [156]. In the last part we combine all data and we discuss the impact of satellite data in the fit.

Modeling of ground data

Using RTModel (see Section 2.3.2), we try to find and evaluate all possible competing models with all the available ground data. From the four-fold satellite degeneracy [28], [157] we find four competitive models

4. PRECISION MEASUREMENT OF A BROWN DWARF MASS IN A BINARY SYSTEM: THE CASE OF OGLE-2019-BLG-0033

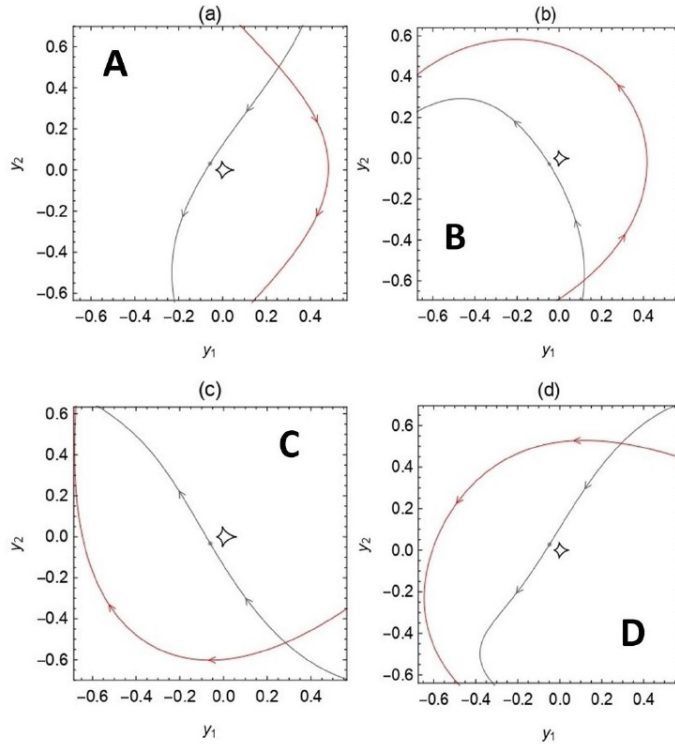


Figure 4.3: Caustics of the four binary lens models examined in our analysis, with the best model labeled as A. The source trajectories are also shown as seen from Earth observatories (black) and from Spitzer (red), Credits [149]

obtained by the reflection of the source trajectory around the binary lens axis and by changes of signs in the parallax components. We label them A, B, C and D (as shown in Fig. 4.3). A big improvement is obtained including the orbital motion that impacts the estimated component of the parallax [20], [158]. We work in the geocentric frame, setting the reference time for the parallax and orbital motion calculations as $t_{0,orb} = t_{0,par} = t_0$.

Once we find these four models with parallax and orbital motion we proceed to the second step where the error bars of all dataset are re-normalized to ensure that $\chi^2/d.o.f. = 1$. This standard procedure makes the fit more robust against possible low-level unknown systematics in the data [159]. At this point including also the limb darkening coefficient for the source in each band (the process of deriving the limb darkening coefficients will be explained later) we ran a Markov Chain Monte Carlo with one million samples to explore the

4. PRECISION MEASUREMENT OF A BROWN DWARF MASS IN A BINARY SYSTEM: THE CASE OF OGLE-2019-BLG-0033

parameter space around each model. In Table 4.1 the final parameters for the four models are shown.

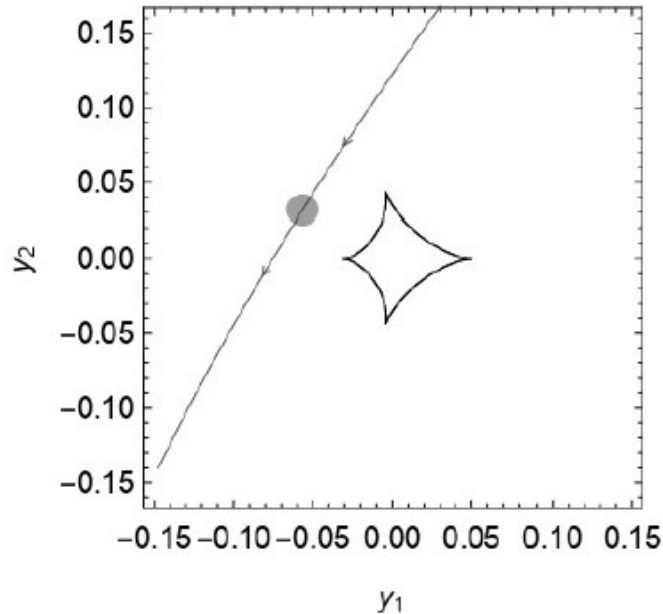


Figure 4.4: Zoom-in on the caustic of the best binary lens model with the source trajectory. The size of the source is shown by the gray disk, Credits [149]

We note that the model *A* stands out with a $\Delta\chi^2 = 120$ from the closest model, the *B*. Without considering the orbital motion we have $\Delta\chi^2 = +477$ from the best solution. If we consider only the static lens we have $\Delta\chi^2 = +4020$. We tried also the binary source and single lens model with a $\Delta\chi^2 = +906$ and a model with a binary lens with parallax and xallarap that gives $\Delta\chi^2 = +215$. None of these were included in the further analysis. Since the timescale is long and the blending is negligible we can have accurate estimates for all the microlensing parameters. The event can be clearly ascribed to a close binary system with a secondary object that is one-third as massive as the primary. The source size parameter, ρ_* , is measured at 3% precision, in spite of the fact that the source trajectory does not cross any caustics. This happens because the giant source passes over the magnified lobes surrounding two cusps

4. PRECISION MEASUREMENT OF A BROWN DWARF MASS IN A BINARY SYSTEM: THE CASE OF OGLE-2019-BLG-0033

Table 4.1: Parameters of the best microlensing models found with ground-only data. Credits [149]

	(Unit)	A	B	C	D
t_E	days	$103.64^{+0.57}_{-0.57}$	$119.26^{+1.55}_{-0.25}$	$102.70^{+0.71}_{-0.38}$	$121.56^{+0.81}_{-0.60}$
t_0	HJD'	$8689.840^{+0.017}_{-0.013}$	$8689.854^{+0.005}_{-0.029}$	$8689.841^{+0.011}_{-0.019}$	$8689.758^{0.008}_{-0.020}$
u_0		$-0.06498^{+0.00036}_{-0.00036}$	$0.05479^{+0.00017}_{-0.00081}$	$0.06899^{+0.00034}_{-0.00055}$	$-0.05594^{+0.00044}_{-0.00029}$
ρ_*		$0.01017^{+0.00030}_{-0.00030}$	$0.00857^{+0.00020}_{-0.00050}$	$0.01083^{+0.00046}_{-0.00058}$	$0.01042^{+0.00049}_{-0.00079}$
α		$1.0311^{+0.0029}_{-0.0024}$	$5.2539^{+0.0052}_{-0.0011}$	$5.2480^{+0.0037}_{-0.0017}$	$1.0173^{+0.0016}_{-0.0041}$
s		$0.3325^{+0.0024}_{-0.0024}$	$0.3228^{+0.0008}_{-0.0056}$	$0.3381^{+0.0016}_{-0.0035}$	$0.3136^{+0.0012}_{-0.0042}$
q		$0.3157^{+0.0059}_{-0.0059}$	$0.2712^{+0.0085}_{-0.0017}$	$0.3360^{+0.0098}_{-0.0051}$	$0.3076^{+0.0115}_{-0.0046}$
$\pi_{E,N}$		$0.2971^{0.0033}_{-0.0082}$	$-0.2566^{+0.0039}_{-0.0075}$	$0.2742^{+0.0077}_{-0.0064}$	$-0.2740^{+0.0119}_{-0.0033}$
$\pi_{E,E}$		$-0.1962^{+0.0035}_{-0.0019}$	$-0.1199^{0.0042}_{-0.0010}$	$-0.2021^{+0.0046}_{-0.0038}$	$-0.1448^{+0.0045}_{-0.0018}$
$(ds/dt)/s$	yr^{-1}	$-1.109^{+0.079}_{-0.055}$	$-1.756^{+0.051}_{-0.142}$	$-0.675^{+0.051}_{-0.124}$	$-1.770^{+0.050}_{-0.154}$
$d\alpha/dt$	yr^{-1}	$-0.146^{+0.084}_{-0.088}$	$1.729^{+0.008}_{-0.097}$	$-2.369^{+0.091}_{-0.149}$	$0.569^{+0.179}_{-0.087}$
$(ds_z/st)/s$	yr^{-1}	< 0.65	< 1.58	< 0.77	< 3.57
I_{OGLE}	mag	$15.6463^{0.0011}_{-0.0005}$	$15.6397^{+0.0010}_{-0.0005}$	$15.6505^{+0.0009}_{-0.0013}$	$15.6409^{+0.0012}_{-0.0003}$
BF_{OGLE}		$0.0461^{+0.0048}_{-0.0066}$	$0.2529^{+0.0187}_{-0.0037}$	$-0.0195^{+0.0081}_{-0.0046}$	$0.2307^{+0.0094}_{-0.0077}$
χ^2		4793.2	4913.0	4919.6	4921.6

4. PRECISION MEASUREMENT OF A BROWN DWARF MASS IN A BINARY SYSTEM: THE CASE OF OGLE-2019-BLG-0033

of the astroid caustic. Its size is large enough to make it sensitive to the steep gradients in these regions, as shown in Figure 4.4. Using ground data only we have an accurate measure for the parallax components. About the orbital motion we have well measured parameters concerning the first component, while the second is marginally seen. In the end we have only an upper limit for the third component. Since the blending is negligible the source flux dominates making the source analysis easier.

Parallax determination from Spitzer

Since the parallax parameters obtained from ground data only can be affected by high order effects, using a different observation point is desirable. For this purpose the data obtained by Spitzer comes in handy and we can test the consistency of the results. In order to do this, we follow the cheap space-based parallax method suggested by Gould & Yee [156] and tested previously by Shin et al. [43], [160]. With Spitzer we can check if, actually, the blending is negligible, the fact that the satellite has a pixel scale of $1.2''$ compared to $0.26''$ for OGLE makes it more exposed to blending by nearby objects. Fortunately, no stars within this angular distance appear in OGLE images or in OGLE catalog and, indeed, the source appears well isolated in the Spitzer images. The lack of blending is confirmed by the comparison of the CMD obtained by MOA observations in V and R filters (top panel of Figure 4.5) with a CMD derived using the I -OGLE band and the L -Spitzer band (bottom panel of Figure 4.5). In both cases, the source lies just slightly below the centroid of the red clump, demonstrating that the ground and space measurements refer to the same object with no appreciable blending. Following the work of Yee et al. [161] and based upon Spitzer photometry of field stars cross-matched with OGLE-EWS CMD, we calculate the color $I - L = -5.67 \pm 0.06$ for a zero point at 25 for Spitzer. Considering a baseline of $I = 15.65$ we get the following baseline flux for Spitzer in instrumental units [149]:

4. PRECISION MEASUREMENT OF A BROWN DWARF MASS IN A BINARY SYSTEM: THE CASE OF OGLE-2019-BLG-0033

$$f_{base,Sp} = 29.65 \pm 0.82 \quad (4.1)$$

The measurements of Spitzer during the event show a quite flat light curve. Taking the average of the two closest observations at time t_0 equal to $f_{t_0,Sp} = 69.52 \pm 0.26$ we can get the magnification seen from Spitzer at this time:

$$A_{0,Sp} = \frac{f_{t_0,Sp}}{f_{base,Sp}} = 2.34 \pm 0.07 \quad (4.2)$$

Also in this case we are considering the blending negligible. Considering the Eq. (1.9) seen in the first chapter and inverting it we can obtain the angular separation of source and lens in Einstein radii (assuming the lens a point mass):

$$u(A) = \sqrt{2[(1 - A^{-2})^{-1/2} - 1]} \quad (4.3)$$

In our case we get $|u_{0,Sp}| = 0.460 \pm 0.015$. The angular separation can be calculated in more detail considering that the lens is binary. We find that $0.44 < u_{0,Sp} < 0.48$ depending on the orientation of the source as seen from Spitzer with respect to the binary lens axis: a result very similar from that obtained by single lens. Indeed, the Spitzer separation is seven times larger than the size of the caustic in Einstein units, so that perturbations of the magnification from lens binarity are small. The offset of the source as seen from Spitzer with respect to the ground again depends on the unknown relative position angle. Therefore, this offset may range from $|u_{0,Sp}| - |u_0|$ to $|u_{0,Sp}| + |u_0|$. Combining the uncertainties we set $\Delta u_0 = |u_{0,Sp}| - |u_0| = 0.46 \pm 0.07$. Considering that at t_0 the distance between Spitzer and Earth projected orthogonally to the line of sight was $d_{0,Sp} = 1.51$ au we can derive the satellite parallax:

$$\pi_{E,Sp} = \Delta u_0 \frac{au}{d_{0,Sp}} = 0.304 \pm 0.05 \quad (4.4)$$

4. PRECISION MEASUREMENT OF A BROWN DWARF MASS IN A BINARY SYSTEM: THE CASE OF OGLE-2019-BLG-0033

The parallax obtained above can be compared with the ground-only parallax $\pi_{E,gr} = 0.356 \pm 0.006$. These two results are completely independent each other. The consistency becomes even more evident when we note that for the best model A, the predicted offset of the source δu as seen from Spitzer is indeed close the maximal value quoted before. We conclude that Spitzer fully validates the ground-only derived parallax making our result more robust against any possible sources of systematics that would remain uncontrolled with ground-only data [149].

Models including ground and Spitzer data

The final step is dedicated to the check for the consistency between ground and Spitzer observations. We conduct a Markov chain explorations including all the data with the constraint for the Spitzer flux based on the Eq. (4.1) so as to remain in acceptable regions during the exploration. The final result is shown in Table 4.2 where we can see that the best model is the *A* with $\Delta\chi^2 = 46$ compared to $\Delta\chi^2 > 71$ for other models. The best model is the only in which the parallax remains within 2σ while in the other models is altered proving that the space parallax would be in tension with the ground parallax in these cases. This tension is apparent in the light curves of these models, which predict a declining trend for the Spitzer light curve that is not observed. The Figure 4.1 shows how the Spitzer lightcurve is quite flat as predicted by model A. Therefore, Spitzer provides an additional strong confirmation of the model found using ground data only. The accuracy for the parallax measure is shown in Figure 4.6. With this analysis we found that Spitzer photometry was free of any important systematic effects, which may be present when the source is faint or blended [136] and that a correct use of the color constraint makes Spitzer data extremely useful for validating ground data and excluding possible additional effects [149].

4. PRECISION MEASUREMENT OF A BROWN DWARF MASS IN A BINARY SYSTEM: THE CASE OF OGLE-2019-BLG-0033

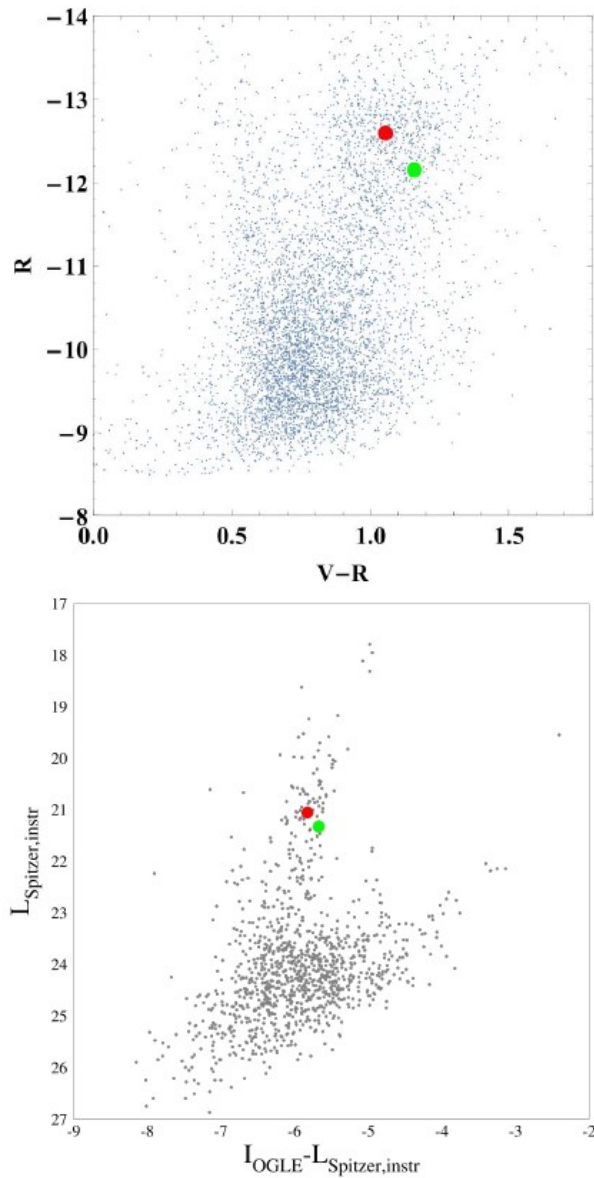


Figure 4.5: Color-magnitude diagrams using different resources. Top panel: CMD of stars in the 2' field of the event OGLE-2019-BLG 0033 built from MOA observations. The red dot corresponds to the center of the red clump and the green dot shows the position of the source. Bottom panel: CMD built from I-band observations from OGLE and L-band measurements from Spitzer. Credits [149]

4.4 Source analysis

Since both the results from ground-only and satellite data are very similar, with a slightly smaller uncertainty if we include the Spitzer data, we

4. PRECISION MEASUREMENT OF A BROWN DWARF MASS IN A BINARY SYSTEM: THE CASE OF OGLE-2019-BLG-0033

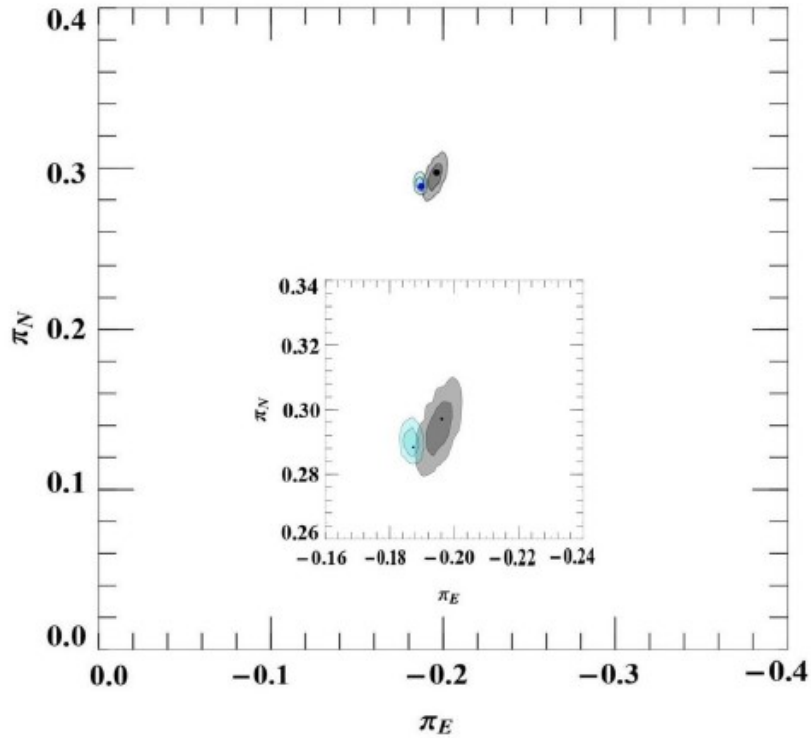


Figure 4.6: Components of the parallax vector as found by the fit excluding Spitzer (in gray) or including Spitzer data (in cyan). Confidence levels at 68% and 95% are given. Credits [149]

adopt the values of the combined fits, that are shown in Table 4.3.

As in the previous chapter in this section we derive the angular source radius θ_* and the limb darkening coefficients adopted for the analysis of the event. In this case there are no observations in V -OGLE band. But for the construction of the CMD, as shown in Figure 4.5, we can use the MOA observations in V and R band and always considering the same figure we can determine the position of the red clump. We have $R_{MOA,Clump} = -12.5931 \pm 0.0091$ and $(V - R)_{MOA,Clump} = 1.0543 \pm 0.0065$. We can convert them to standard Johnson-Cousins magnitudes using the photometric relations by Bond et al. [148]:

4. PRECISION MEASUREMENT OF A BROWN DWARF MASS IN A BINARY SYSTEM: THE CASE OF OGLE-2019-BLG-0033

Table 4.2: Comparison of parallax π_E and χ^2 for our four models if Spitzer data are included or excluded. Credits [149]

Model	π_E	χ^2
Spitzer Data Excluded		
A	$0.3560^{+0.0061}_{-0.0061}$	4973.2
B	$0.2832^{+0.0060}_{-0.0040}$	4913.0
C	$0.3406^{+0.0078}_{-0.0068}$	4919.6
D	$0.3099^{+0.0032}_{-0.0121}$	4921.6
Spitzer Data Included		
A	$0.3439^{+0.0005}_{-0.0005}$	4839.1
B	$0.3333^{+0.0005}_{-0.0008}$	5001.0
C	$0.2878^{+0.0008}_{-0.0011}$	5231.0
D	$0.3099^{+0.0011}_{-0.0005}$	4992.0

$$\begin{aligned}
 I_{Clump} &= R_{MOA,Clump} + 28.0264 - 0.1984(V_{MOA,Clump} - R_{MOA,Clump}) \\
 V_{Clump} &= V_{MOA,Clump} + 28.6274 - 0.1682(V_{MOA,Clump} - R_{MOA,Clump})
 \end{aligned} \tag{4.5}$$

From these we obtain $I_{Clump} = 15.2241 \pm 0.0095$ and $(V - I)_{Clump} = 1.6872 \pm 0.0074$. Comparing to the Red Clump Intrinsic magnitude $I_{Clump,0} = 14.384 \pm 0.040$ [104] and color $(V - I)_{Clump,0} = 1.06 \pm 0.07$ [103] we find a reddening of $E(V - I) = 0.627$ and an extinction $A_I = 0.852$.

The best model considered has a negligible blending so we can attribute the baseline flux entirely to the source. In this way applying the same equations as above and including extinction and reddening we obtain $(V - I)_{*,0} = 1.137 \pm 0.071$ and $I_{*,0} = 14.835 \pm 0.042$. As made in the previous chapter we pass from the (V, I) bands to the (V, K) bands and following Kervella et al. [106] we find the angular radius of the source:

$$\theta_* = 5.49 \pm 0.32 \mu\text{as} \tag{4.6}$$

4. PRECISION MEASUREMENT OF A BROWN DWARF MASS IN A BINARY SYSTEM: THE CASE OF OGLE-2019-BLG-0033

Table 4.3: Microlensing parameters for model A including Spitzer data.
Credits [149]

Parameter		Model A w/ Spitzer
t_E	days	$103.85^{+0.47}_{-0.47}$
t_0	HJD'	$8689.856^{+0.015}_{-0.011}$
u_0		$-0.06491^{+0.00035}_{-0.00035}$
ρ_*		$0.01007^{+0.00035}_{-0.00035}$
α		$1.0338^{+0.0030}_{-0.0023}$
s		$0.3336^{+0.0024}_{-0.0024}$
q		$0.3114^{+0.0059}_{-0.0059}$
$\pi_{E,N}$		$0.2884^{+0.0010}_{-0.0006}$
$\pi_{E,E}$		$-0.1873^{+0.0018}_{-0.0009}$
$(ds/dt)/s$	yr^{-1}	$-1.080^{+0.084}_{-0.055}$
$d\alpha/dt$	yr^{-1}	$-0.091^{+0.091}_{-0.073}$
$(ds_z/st)/s$	yr^{-1}	< 0.45
I_{OGLE}	mag	$15.6459^{0.0006}_{-0.0005}$
BF_{OGLE}		$0.0477^{+0.0040}_{-0.0071}$
χ^2		4839.05

4. PRECISION MEASUREMENT OF A BROWN DWARF MASS IN A BINARY SYSTEM: THE CASE OF OGLE-2019-BLG-0033

From the Gaia EDR3 we get the source parallax $\pi_S = -0.013 \pm 0.089$ mas that is compatible with zero within the errors [47], [162]. So, for an estimate of the source distance, we solely rely on the CMD. As the source position in the CMD is very close to the bulge red clump, it is reasonable to assume it is a bulge giant. Using the Galactic model by Dominik [110] for this event we find that the peak stellar density in the bulge along the observation cone is encountered at a distance $D_S = 8.1$ kpc which we assume to be a valid proxy for the source distance as well. The uncertainty in the source distance is assumed to be 1 kpc, reflecting the FWHM of the stellar density distribution along the line of sight [149]. For the limb darkening coefficients we adopt the same procedure followed in the previous chapter: we simulate a stellar population using IAC-Star [107] with the stellar evolution library by Bertelli et al. [108] and the bolometric correction by Castelli & Kurucz [109] and we find for the source $T_{eff} = 4950$ K, $\log g = 2.77$ and $Z = 0.011$. Comparing these values in the tables by Claret & Bloemen [163] we get the linear limb darkening coefficients in the relevant bands: $a_I = 0.5015$, $a_R = 0.5983$ and $a_V = 0.6945$. The analysis explained in the previous section has been made with these coefficients.

4.5 Lens system properties

4.5.1 Mass and distance

For the event OGLE-2019-BLG-0033 we have just one best model without degeneracies and with accurate estimates for parallax and source size parameters. We also have a negligible blend with all the base flux generated by a red clump giant source that allow us to estimate the Einstein angle:

$$\theta_E = \frac{\theta_*}{\rho_*} = 0.545 \pm 0.037 \text{ mas} \quad (4.7)$$

Having both π_E and θ_E measured we are able to estimate the mass and the distance of the lens:

4. PRECISION MEASUREMENT OF A BROWN DWARF MASS IN A BINARY SYSTEM: THE CASE OF OGLE-2019-BLG-0033

Table 4.4: Parameters of the binary lens system. Credits [149]

Parameter	Value
$M_1 (M_\odot)$	0.1494 ± 0.0099
$M_2 (M_\odot)$	0.0463 ± 0.0031
$a_\perp (au)$	0.585 ± 0.054
$D_L (kpc)$	3.22 ± 0.21

$$\begin{aligned}
 M &= \frac{\theta_E}{\kappa\pi_E} = 0.195 \pm 0.013 M_\odot \\
 D_L &= \frac{au}{\theta_E\pi_E + \pi_S} = 3.22 \pm 0.21 kpc
 \end{aligned}
 \tag{4.8}$$

Using the mass ratio q we get the masses of the two components of the binary system: $M_1 = M/(1+q) = 0.1494 \pm 0.0099 M_\odot$ and $M_2 = Mq/(1+q) = 0.0463 \pm 0.0031 M_\odot$. The projected separation of the two lenses is:

$$a_\perp = s\theta_E S_L = 0.585 \pm 0.054 au \tag{4.9}$$

These results are summarized in the Table 4.4.

The binary system is composed by a red dwarf of $0.15 M_\odot$ and a BD of $0.046 M_\odot$. The result is in agreement with the negligible blending flux since the light from this system is very weak, $V \sim 26$ for a M5V red dwarf [164]. The separation of 0.58 au is typical for binary systems discovered through the microlensing method as the sensitivity to companions is maximized for separations of the same order as the Einstein radius.

4.5.2 Orbital motion

In order to check if the orbital motion is physically acceptable we calculate the mass ratio between the projected kinetic energy and the projected potential energy (like in the previous chapter). Taking the Eq. (3.3) and putting the values of the parameters obtained we get $K = 0.0153$ which

4. PRECISION MEASUREMENT OF A BROWN DWARF MASS IN A BINARY SYSTEM: THE CASE OF OGLE-2019-BLG-0033

satisfies the constraint, but remains relatively smaller than typical expectations from a random distribution of orbits. Such small values indicate a nearly edge-on orbit, which would apply to our case, given that $\gamma_{\perp}/\gamma_{\parallel} = 0.09$. So, with the information in hand, we can conclude that the orbital motion suggested by the light curve fit is perfectly acceptable and consistent with the constraints on the mass and scale of the system coming from the combination of parallax and finite source effects [149].

4.5.3 Lens kinematics

Once we have the Einstein angle we can get the lens-source proper motion:

$$\mu_{rel} = \frac{\theta_E}{t_E} = 1.92 \pm 0.13 \text{ mas yr}^{-1} \quad (4.10)$$

From this we can derive the components in the eastern and northern directions in the geocentric frame, using the parallax vector:

$$\mu_{rel,geo} = \frac{\mu_{rel}}{\pi_E} (\pi_{E,E}, \pi_{E,N}) = (-1.04 \pm 0.07, 1.61 \pm 0.11) \text{ mas yr}^{-1} \quad (4.11)$$

The result can be converted in the heliocentric frame using the velocity components of the Earth at time t_0 projected orthogonally to the line of sight:

$$\mu_{rel,hel} = \mu_{rel,geo} + v_{\oplus} \frac{\pi_{rel}}{au} = (-0.04 \pm 0.07, 1.56 \pm 0.011) \text{ mas yr}^{-1} \quad (4.12)$$

Using the measurement of the proper motion of the source from Gaia EDR3, we can derive the lens kinematics. From Gaia we have:

$$\mu_s = (-0.872 \pm 0.093, -7.28 \pm 0.067) \text{ mas yr}^{-1} \quad (4.13)$$

that are the components in the eastern and northern directions respectively. The lens proper motion will be:

$$\mu_L = \mu_{rel,hel} + \mu_s = (-0.91 \pm 0.12, -5.72 \pm 0.13) \text{ mas yr}^{-1} \quad (4.14)$$

4. PRECISION MEASUREMENT OF A BROWN DWARF MASS IN A BINARY SYSTEM: THE CASE OF OGLE-2019-BLG-0033

In order to measure μ_L in the Galactic frame we rotate it by 61.36° ;

$$\mu_{L,Gal} = (-5.46 \pm 0.12, -1.94 \pm 0.12) \text{ mas yr}^{-1} \quad (4.15)$$

Here, the first component is along the Galactic longitude direction l and the second component is along the Galactic latitude b . Knowing the distance of the lens we can get the velocity components:

$$v_{L,Gal} = (-83.2 \pm 5.7, -29.6 \pm 2.7) \text{ km/s} \quad (4.16)$$

Finally, subtracting the peculiar velocity of the Sun, we may move to the local standard of rest (LSR):

$$v_{L,LSR} = (-71.0 \pm 5.7, -23.3 \pm 2.7) \text{ km/s} \quad (4.17)$$

Since the line of sight is very close to the Galactic center, these components are very close to the peculiar velocity components of the lens along the tangential circle, v , and orthogonal to the Galactic plane, w , respectively [149]. The value for the velocity obtained is common for red metal-poor old stellar populations from the disk, as can be inferred from studies of the asymmetric drift [165]. Studying the kinematics allows us to firmly assign our lens, made up of a red and a brown dwarf, to Population II stars in the thick disk. Similar conclusions were obtained by Gould [16] proving the effectiveness of microlensing in the investigation of populations of very low-mass components of our Galaxy.

4.6 Discussion

OGLE-2019-BLG-0033 is not the first binary microlensing with a BD discovered. In Table 4.5 there are other similar microlensing events. In particular we collect the events with the best precision measurement for BDs in literature and we realize that this event is among those with the most precise mass measurements ever realized for a BD in binary system. With the analysis

4. PRECISION MEASUREMENT OF A BROWN DWARF MASS IN A BINARY SYSTEM: THE CASE OF OGLE-2019-BLG-0033

Table 4.5: Binary microlensing events with relative error less than 10% for the BD mass. The suffixes A and B in the names indicate that the BD is the primary or the secondary component in the lens. No suffix means that the BD lens was isolated. Credits [149]

Name of the event	BD mass (M_{\odot})	Rel. unc. (%)	Reference
OGLE-2011-BLG-0420A	0.025	4	Choi et al. 2013 [142]
MOA-2007-BLG-197B	0.039	5	Ranc et al. 2015 [141]
OGLE-2009-BLG-151A	0.018	5.5	Choi et al. 2013 [142]
OGLE-2019-BLG-0033B	0.046	6.8	this work
OGLE-2007-BLG-224	0.056	7.1	Gould et al. 2009 [139]
OGLE-2012-BLG-0358A	0.022	8.6	Han et al. 2013 [79]
OGLE-2016-BLG-1266A	0.015	10	Albrow et al. 2018 [143]
MOA-2011-BLG-149B	0.019	10.5	Shin et al. 2012 [166]

of this event we demonstrate how microlensing is very important to the study of low mass objects in the Milky Way. In general it is very difficult find a solution without degeneracies. The case of OGLE-2019-BLG-0033 shows that long events with clear parallax and orbital motion signals are optimal for at least two reasons: a precise parallax detection gives a mass-distance relation to be combined with other constraints on θ_E ; orbital motion may distinguish otherwise degenerate solutions and help single out the correct model. For short events difficulties increase because discrete degeneracies can give several interpretations for the lens geometry with typically different values for the masses in spite of individual low uncertainties for the degenerate models [133], [167]. However, annual parallax measurements rely on long-term modulations in the observed flux for which there might be possible alternative explanations or contaminants, including lens orbital motion itself, xallarap, long-term variability of the source, or systematics in the data. Therefore, the presence of measurements from a different point of observation such as Spitzer, allows for an independent determination of parallax that goes back to pure geometry rather than subtle modulations in the photometry. In fact, Spitzer

4. PRECISION MEASUREMENT OF A BROWN DWARF MASS IN A BINARY SYSTEM: THE CASE OF OGLE-2019-BLG-0033

observations contribute to a further reduction with regard to the uncertainty inherent in our best model [149]. The second quantity needed to have precision mass measurement is θ_E that in our case we derived from the detection of the finite source effects. Since the source is a red clump giant the analysis was very easy. The importance of the source analysis should not be underestimated in microlensing mass measurements. Indeed, even in our optimal situation, θ_* dominates the error budget in the derived masses. One way to improve the source knowledge could be a systematic spectroscopic survey of bright sources of microlensing events, which certainly may enhance the significance of microlensing mass measurements [103], [168], [169]. If finite source effects cannot be estimated high-resolution imaging can help, in particular for event with fast-moving lenses (and also sufficiently bright) [170]. The discovered BD adds to the more than 3,000 already found. Most of them are in the solar neighborhood [171] while some are in binary systems or in young clusters [172]. A BD desert was postulated since none of these object was discovered around FGK stars in a close orbit < 5 au [123]. The theories describing the formation of BD binaries are various as their detection is complicated. Microlensing can be very important for its ability to identify such systems, especially with regard to measuring the masses of BDs in binaries and quantifying their occurrence throughout the Galaxy. Kinematic studies combining relative lens-source proper motions from microlensing and source proper motion from Gaia provide very interesting perspectives for assigning low-mass systems to the correct dynamical component of the Galaxy and understanding how the production of BDs may have evolved during the history of the Milky Way [149]. For this purpose the upcoming Roman Telescope will give a huge contribution for the census of these objects combining high-resolution imaging, space parallax and precise characterization of resolved source, and in some cases, also with the xallarap. It has a 100 wider field of view with respect to the James Webb Telescope [173] that will be very important for this topic since it will be well-suited for the detection of BDs and free floating planets in smaller fields, such as clusters and for the detailed investigation on nearby BDs. In the next

4. PRECISION MEASUREMENT OF A BROWN DWARF MASS IN A BINARY SYSTEM: THE CASE OF OGLE-2019-BLG-0033

years we will have the Extremely Large Telescope equipped with Advanced Optics [174] that will be fundamental for astrometry in crowded fields. In this way we can re-analyze all past microlensing events since every year about 100 microlensing binary events are discovered and most of them are composed of low-mass objects. A systematic astrometric investigation of all events would thus build a very broad, detailed, and reliable statistics of binary systems in our Galaxy.

CHAPTER 5

MICROLENSING IN THE GAIA ERA: GAIA20BOF AND GAIA21BLX

The advent of the latest generation of large-sky surveys is changing the face of microlensing. An important role is played by the Gaia satellite which, by observing the entire sky, allows us to discover microlensing events that are of considerable importance for several reasons. First of all we are able to discover events not only in the bulge direction but also in other regions of the sky (obviously with less cadence than the bulge direction). Moreover with Gaia observations we can characterize microlensing events with the detection of parallax or orbital motion since the duration of events in the Galactic Disk is usually long enough to detect high order effects. And with the astrometric series delivered by Gaia we will have a new way to measure the Einstein angle [175] providing mass/distance relation for a large fraction of lenses.

In this contest the follow-up observations make the difference and the OMEGA Key Project, specialized in performing automatic follow-up of microlensing events detected by large-sky surveys in the entire sky whose primary goal is the characterization of cold planets and stellar remnant (as explained in the dedicated section), plays a fundamental role.

5. MICROLENSING IN THE GAIA ERA: GAIA20BOF AND GAIA21BLX

In this chapter we present the analysis of two microlensing events detected by the Gaia satellite: Gaia20bof and Gaia21blx. The first has several degenerate solutions (including some planetaries) while the second is still with degenerate solutions but with an interesting way to derive the lens properties using the Gaia parallax and the blend flux.

5.1 Gaia20bof

5.1.1 Observations

The event is located in the Galactic Disk at (R.A., decl.) = $(12^h18^m28^s.36, -63^\circ29'50''.14)$ corresponding to Galactic coordinates $l = 299.26406^\circ$, $b = -0.86052^\circ$. It was alerted the 30 March 2020 by Gaia Science Alerts while the spectroscopic observation of SALT [176] confirmed the fact that it was a microlensing event the 10 June 2020.

In Table 5.1 all the data collected for this event are summarized. As we can see there are a lot of images taken in the SDSS-g' and SDSS-i' bands from Siding Spring in Australia (COJ), South African Astronomical Observatory in South Africa (CPT) and La Silla in Chile (LSC). We note that just few images are taken from the LSC telescopes: this is due to the COVID-19 pandemic which blocked the observations. Data reduction was made with pyDANDIA.

5.1.2 Modeling

From the Figure 5.1 we can see the anomaly at $HJD' \sim 9025$ which suggests to us that we could have a binary lens configuration or even a binary source. We start the analysis using the RTModel platform [21], [57], [59]. In a first step we try the binary source single lens model in order to describe the anomaly but we obtain a χ^2 two times higher than the binary lens model so we excluded it. We keep the binary lens model including the parallax and we start a Markov Chain in order to explore the space parameters. The results are listed in Table 5.2 where we presented eight degenerate models. This is due to the

5. MICROLENSING IN THE GAIA ERA: GAIA20BOF AND GAIA21BLX

Table 5.1: Summary of photometric observations. Due to the low number of observations, the LSC datasets were not used in the modeling. This is mainly due to the COVID-19 pandemic and the LCO site at La Silla remains closed longer than other sites. Courtesy of Etienne Bachelet, (Bachelet et al. 2023, in prep.)

Name	Filter	Observations	k
Gaia	G	169	2.058
COJA_gp	SDSS-g'	43	7.052
COJA_ip	SDSS-i'	64	4.779
COJB_gp	SDSS-g'	61	3.905
COJB_ip	SDSS-i'	55	3.782
CPTA_gp	SDSS-g'	5	1.087
CPTA_ip	SDSS-i'	10	3.759
CPTB_gp	SDSS-g'	11	1.043
CPTB_ip	SDSS-i'	14	2.327
CPTC_gp	SDSS-g'	12	1.496
CPTC_ip	SDSS-i'	12	1.710
LCO-coj1m003_gp	SDSS-g'	41	1.223
LCO-coj1m003_ip	SDSS-i'	68	1.598
LCO-coj1m011_gp	SDSS-g'	34	0.903
LCO-coj1m011_ip	SDSS-i'	72	1.689
LCO-cpt1m010_gp	SDSS-g'	17	0.741
LCO-cpt1m010_ip	SDSS-i'	19	0.798
LCO-cpt1m012_gp	SDSS-g'	24	0.634
LCO-cpt1m012_ip	SDSS-i'	30	0.736
LCO-cpt1m013_gp	SDSS-g'	22	0.732
LCO-cpt1m013_ip	SDSS-i'	25	1.021
PROMPT04_ip	SDSS-i'	15	2.286
TRT-SB007_ip	Johnson-I	11	1.993
TRT-SB007_vp	Johnson-V	11	1.993
LSCA_gp	SDSS-i'	3	*
LSCA_ip	SDSS-g'	2	*
LSCC_gp	SDSS-g'	2	*

5. MICROLENSING IN THE GAIA ERA: GAIA20BOF AND GAIA21BLX

fact that there is no clear caustic crossing by the source, as it is immediately noticeable from the fact that ρ_* parameter is not measured but there is only an upper limit. On the other hand this configuration is very similar to the approach of a Chang-Refsdal lens that presents a strong degeneracy in terms of lens geometries [15]. Among these solutions the Wide+ seems to be the best, but all the solutions may be possible.

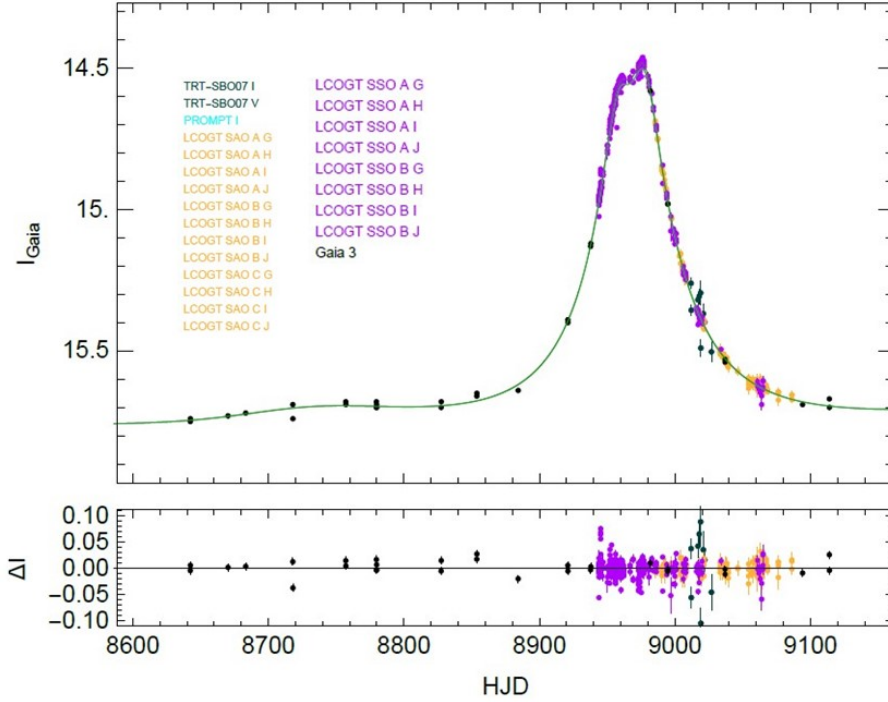


Figure 5.1: Lightcurve with residuals of the best model (Wide+) for Gaia20bof

About the the χ^2 calculated we adopt the usual procedure used also in the Chapter 3 where the original errors in magnitude are rescaled with the two parameters k and e_{min} . Also for this model e_{min} is set to zero for each dataset since it is not a high magnification event and k is such that $\chi^2/d.o.f \sim 1$ (see Table 5.1).

5.1.3 Source analysis

During the event one spectrum was collected by the SALT (Southern African Large Telescope) the 6 June 2020 when the magnification was ~ 1.8 while another one was taken by the XShooter at the VLT at the baseline the

5. MICROLENSING IN THE GAIA ERA: GAIA20BOF AND GAIA21BLX

Table 5.2: Best models from the modeling of the lightcurves. Courtesy of Etienne Bachelet, (Bachelet et al. 2023, in prep.)

Parameters	Unit	CloseB-	CloseB+	CloseP-	CloseP+	Resonant-	Resonant+	Wide-	Wide+
t_E	days	$56.860^{+2.050}_{-0.290}$	$64.406^{+1.306}_{-1.094}$	$56.698^{+2.398}_{-1.102}$	$67.229^{+2.469}_{-0.961}$	$64.931^{+2.131}_{-1.169}$	$58.073^{+1.973}_{-1.327}$	$609.576^{+71.575}_{-129.424}$	$122.000^{+5.000}_{-5.000}$
t_0	HJD	$8971.750^{+0.093}_{-0.303}$	$8971.780^{+0.117}_{-0.173}$	$8969.302^{+0.054}_{-0.037}$	$8969.245^{+0.043}_{-0.051}$	$8969.342^{+0.020}_{-0.084}$	$8969.210^{+0.052}_{-0.043}$	$8782.530^{+4.868}_{-0.902}$	$8893.300^{+2.400}_{-2.400}$
u_0		$-0.2723^{+0.0138}_{-0.0020}$	$0.2531^{+0.0052}_{-0.0062}$	$-0.2645^{+0.0122}_{-0.0088}$	$0.2641^{+0.0049}_{-0.0111}$	$0.2423^{+0.0081}_{-0.0097}$	$-0.2974^{+0.0138}_{-0.0050}$	$-0.1540^{+0.0190}_{-0.0340}$	$1.0500^{+0.0600}_{-0.0600}$
ρ_*		< 0.0631	< 0.0583	< 0.0724	< 0.0621	< 0.0684	< 0.1023	< 0.0427	< 0.0721
α		$0.9146^{+0.0069}_{-0.0332}$	$5.3689^{+0.0169}_{-0.0131}$	$-1.6310^{+0.0027}_{-0.0018}$	$1.6411^{+0.0017}_{-0.0034}$	$4.6525^{+0.0028}_{-0.0012}$	$-4.6398^{+0.0019}_{-0.0032}$	$-5.7510^{+0.0550}_{-0.0550}$	$5.1660^{+0.0170}_{-0.0170}$
s		$0.4153^{+0.0044}_{-0.0072}$	$0.4314^{+0.0031}_{-0.0075}$	$0.5706^{+0.0058}_{-0.0058}$	$0.5430^{+0.0080}_{-0.0080}$	$1.4049^{+0.0229}_{-0.0251}$	$1.4571^{+0.0063}_{-0.0648}$	$3.6421^{+0.0101}_{-0.0279}$	$3.7100^{+0.0500}_{-0.0500}$
q		$1.0207^{+0.1500}_{-0.0038}$	$0.8305^{+0.0685}_{-0.0475}$	$0.0364^{+0.0017}_{-0.0017}$	$0.0431^{+0.0023}_{-0.0023}$	$0.04400^{+0.0021}_{-0.0026}$	$0.0507^{+0.0009}_{-0.0055}$	$0.7934^{+0.0524}_{-0.0256}$	$0.8700^{+0.0600}_{-0.0600}$
$\pi_{E,N}$		$0.3660^{+0.0049}_{-0.0224}$	$0.2188^{+0.0086}_{-0.0107}$	$0.2566^{+0.0074}_{-0.0091}$	$0.3043^{+0.0060}_{-0.0123}$	$0.2449^{+0.0091}_{-0.0065}$	$0.2914^{+0.0077}_{-0.0100}$	$0.1538^{+0.0157}_{-0.0157}$	$0.0930^{+0.0120}_{-0.0120}$
$\pi_{E,E}$		$-0.3447^{+0.0148}_{-0.0157}$	$-0.3566^{+0.0147}_{-0.0143}$	$-0.3361^{+0.0071}_{-0.0071}$	$-0.4025^{+0.0098}_{-0.0098}$	$-0.3277^{+0.0078}_{-0.0078}$	$-0.3391^{+0.0119}_{-0.0151}$	$-0.2477^{+0.0102}_{-0.0102}$	$-0.3283^{+0.0013}_{-0.0013}$
G_s	Vega mag	15.92 ± 0.01	16.06 ± 0.02	15.91 ± 0.01	16.08 ± 0.01	15.92 ± 0.01	16.09 ± 0.02	$16.22/pm0.01$	16.8 ± 0.01
G_b	Vega mag	18.1 ± 0.1	17.36 ± 0.08	18.11 ± 0.09	17.31 ± 0.04	18.07 ± 0.08	17.27 ± 0.07	16.98 ± 0.02	17.34 ± 0.03
g_s	AB mag	17.141 ± 0.007	17.25 ± 0.01	17.127 ± 0.006	17.271 ± 0.007	17.141 ± 0.005	17.28 ± 0.01	17.441 ± 0.005	17.317 ± 0.005
g_b	AB mag	18.27 ± 0.03	18.09 ± 0.03	18.33 ± 0.03	18.04 ± 0.032	18.30 ± 0.03	18.06 ± 0.03	17.74 ± 0.01	17.96 ± 0.02
i_s	AB mag	15.473 ± 0.008	15.573 ± 0.008	15.457 ± 0.008	15.603 ± 0.008	15.450 ± 0.006	15.60 ± 0.01	15.755 ± 0.003	15.651 ± 0.004
i_b	AB mag	16.97 ± 0.06	16.87 ± 0.03	17.06 ± 0.07	16.61 ± 0.04	17.41 ± 0.04	16.76 ± 0.03	16.295 ± 0.003	16.615 ± 0.009
χ^2		756	759	759	779	769	785	785	750
$\chi^2_{small} - \chi^2_{large}$		6.59	4.83	6.63	6.05	5.62	5.68	5.31	6.30

5. MICROLENSING IN THE GAIA ERA: GAIA20BOF AND GAIA21BLX

7 January 2022. Both the spectra are shown in Figure 5.2 and the results are listed in Table 5.3 with a good agreement with the measurements released from Gaia-DR3 that indicates $T_{eff} = 5430 K$ and $logg = 3.52$ and a source distance of $D_S = 2.2 kpc$. In addition to this information we consider the PARSEC stellar isochrones and we found that the source is most likely an old subgiant. From the source luminosity, the source magnitude in G_{Gaia} band and the extinction law obtained from the analysis of the spectra we found that the source angular radius is $\theta_* \sim 5.5 \mu as$ and it is independent of the source distance that is $D_S = 2.0_{-0.3}^{+0.6} kpc$. The result obtained is in agreement with the parallax measurements from Gaia, but slightly closer, probably due to the presence of the blend in the Gaia measurements (Bachelet et al. 2023, in prep.).

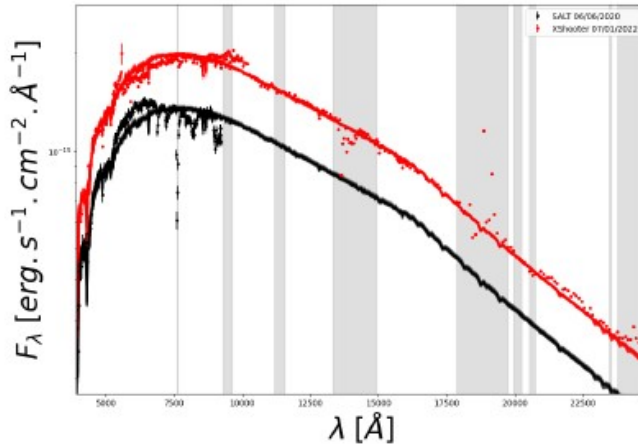


Figure 5.2: The two spectra from SALT (black) and XShooter (red), as well as several models from the MCMC exploration, are visible. The gray vertical lines indicates absorption bands, where the data were not used for the modeling. Courtesy of Etienne Bachelet, (Bachelet et al. 2023, in prep.)

5.1.4 Constraint on the lens and discussion

From the derivation of the source distance and the blend we can have an upper limit for the lens mass $M_L \leq 0.8 M_\odot$. More details can be obtained with the astrometry from which we can derive the Einstein angle and the lens

5. MICROLENSING IN THE GAIA ERA: GAIA20BOF AND GAIA21BLX

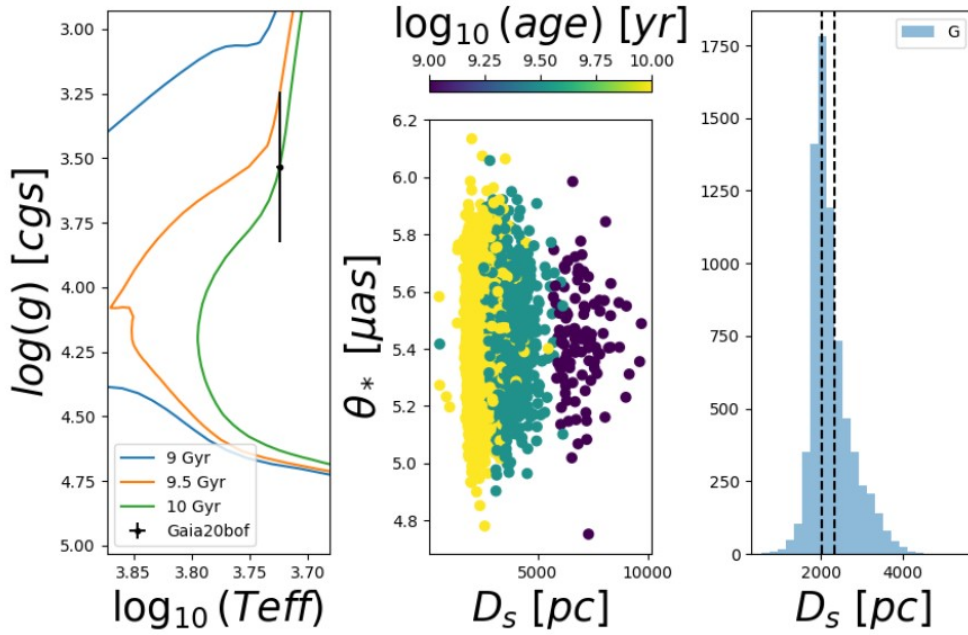


Figure 5.3: (Left) PARSEC stellar isochrones for 9, 9.5 and 10 Gyr with a fix metallicity of -0.75. The source is most likely an old subgiant. (Middle) Source angular radius based on the spectral models as a function of the source distance and age (color-coded). (Right) Source distance based on the Gaia source measurements from the model ($G_s \sim 16$ mag) and the extinction estimated from the spectral modeling. Black dash lines indicates the 1- σ confidence region from the parallax measurement of Gaia. Courtesy of Etienne Bachelet, (Bachelet et al. 2023, in prep.)

mass. In Figure 5.4 we show the astrometric signals as seen by Gaia assuming $\theta_E = 1$ mas. Information from astrometry was used for the first time in Gaia16aye [48] so with the advent of the Gaia DR 4 we can finally break the degeneracy of Gaia20bof. Another step forward could be done with the use of high resolution imaging, like the blend flux: we can note from the Table 5.2 how the blend is different for every model. With the high resolution imaging we can fix this value measuring the lens flux directly, limiting the number of possible scenarios. In conclusion, for the moment, we can assume that the lens is a binary system with an upper limit for the mass that can be defined more precisely considering the astrometry with the Gaia DR 4 and with the high

5. MICROLENSING IN THE GAIA ERA: GAIA20BOF AND GAIA21BLX

Parameters	
A_v [mag]	$1.56^{+0.02}_{-0.04}$
T_{eff} [K]	5300^{+30}_{-30}
Fe/H	$-0.7^{+0.3}_{-0.1}$
log g	$3.50^{+0.30}_{-0.25}$

Table 5.3: Parameters of the source from spectroscopic analysis. Courtesy of Etienne Bachelet, (Bachelet et al. 2023, in prep.)

resolution imaging.

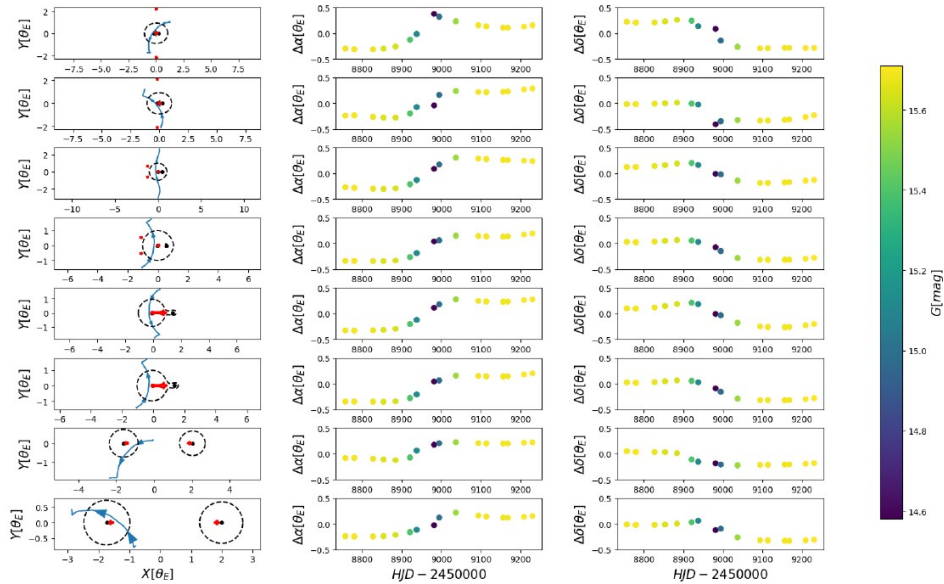


Figure 5.4: (Left) The source trajectories (blue), caustics (red) and critical curves (black) for the eight models for Gaia20bof. Note that the center of mass of the lenses is kept fixed at (0,0). The microlensing astrometric deflections in right ascension (Middle) and in declination (Right) versus time are also displayed. The color indicates the observed Gaia G magnitude. Courtesy of Etienne Bachelet, (Bachelet et al. 2023, in prep.)

5.2 Gaia21blx

5.2.1 Observations

Gaia21blx is located in the Galactic Disk at (R.A., decl.) = $(14^h53^m15^s.42, -62^\circ01'30''.61)$ corresponding to Galactic coordinates $l = 316.69911^\circ$, $b = -2.45443^\circ$. The alert was published the 22 March 2021 with Gaia magnitude of ~ 16.64 . After the alert follow-up observations started with data collected in g' band from the CTIO telescope and i' band from the SAO telescopes of the LCOGT network.

5.2.2 Modeling

The first step is made using the RTModel platform [21], [57], [59] from which we obtain a close binary lens model with parallax. Since from the beginning we have ρ_* and π_E well measured so that in principle we are able to derive mass and distance of the lens. From the best solutions obtained with RTModel we start a Levenberg-Marquardt algorithm in order to minimize the χ^2 and after this we run Markov Chains to find the best solution. In a second moment we consider the inclusion of the orbital motion for a more robust estimate of errors in parallax (we label it LOClose). Starting from the initial model (the parallax one) we run three other cases: the first is obtained changing the s parameter due to the offset degeneracy [26] (the wide configuration LOWide), while the second is derivated from the first changing the sign of u_0 and α (called LOCloseR whose lightcurve is shown in Figure 5.5). The last is obtained with the reflection of u_0 and α from the wide configuration (LOWideR). All the caustic configurations and the source trajectories are shown in Figure 5.6. The final results, including the orbital motion, are shown in Table 5.4 where we can note that the orbital parameters can be compatible with to 0 in the errors and the χ^2 are similar, which forces us, at first, to retain all competitive models.

5. MICROLENSING IN THE GAIA ERA: GAIA20BOF AND GAIA21BLX

Table 5.4: Parameters of the best models. Rota et al. 2023 in prep.

Parameters	(Unit)	LOcloseR	LOclose	LOWide	LOWideR
t_E	days	$152.800^{+7.700}_{-7.700}$	$134.374^{+13.374}_{-16.626}$	$101.270^{+4.470}_{-13.029}$	$120.960^{+18.960}_{-7.040}$
t_0	<i>HJD</i>	$9300.318^{+0.027}_{-0.524}$	$9300.755^{+0.092}_{-0.209}$	$9297.420^{+0.158}_{-0.046}$	$9297.830^{+0.072}_{-0.072}$
u_0		$0.0887^{+0.0046}_{-0.0017}$	$-0.0968^{+0.0061}_{-0.0061}$	$0.0263^{+0.0016}_{-0.0016}$	$-0.0093^{+0.0007}_{-0.0027}$
ρ_*		$0.0019^{+0.0001}_{-0.0003}$	$0.0020^{+0.0003}_{-0.0002}$	$0.0027^{+0.0001}_{-0.0002}$	$0.0021^{+0.0005}_{-0.0001}$
α		$-4.9001^{+0.0115}_{-0.0115}$	$4.9009^{+0.0032}_{-0.0216}$	$4.9909^{+0.0219}_{-0.0201}$	$-5.0379^{+0.0498}_{-0.0498}$
s		$0.4332^{+0.0124}_{-0.0048}$	$0.4539^{+0.0159}_{-0.0159}$	$2.0116^{+0.0033}_{-0.0033}$	$1.9926^{+0.0019}_{-0.0019}$
q		$0.5471^{+0.0401}_{-0.0429}$	$0.4509^{+0.0269}_{-0.0611}$	$0.2344^{+0.0188}_{-0.0063}$	$0.2049^{+0.0099}_{-0.0208}$
$\pi_{E,N}$		$0.1360^{+0.0420}_{-0.0190}$	$0.1048^{+0.0229}_{-0.0411}$	$0.2247^{+0.0127}_{-0.0823}$	$0.2193^{+0.0833}_{-0.0097}$
$\pi_{E,E}$		$0.0001^{+0.0456}_{-0.0049}$	$-0.1468^{+0.0097}_{-0.0447}$	$-0.2114^{+0.0136}_{-0.0464}$	$-0.0504^{+0.0998}_{-0.0006}$
γ_{\parallel}	days ⁻¹	$-0.0020^{+0.0021}_{-0.0003}$	$-0.0022^{+0.0015}_{-0.0015}$	$0.0009^{+0.0008}_{-0.0003}$	$0.0022^{+0.0023}_{-0.0001}$
γ_{\perp}	days ⁻¹	$0.0001^{+0.0007}_{-0.0007}$	$0.0023^{+0.0011}_{-0.0005}$	$-0.0003^{+0.0004}_{-0.0005}$	$0.0049^{+0.0033}_{-0.0007}$
γ_z	days ⁻¹	$0.0028^{+0.0020}_{-0.0022}$	$0.0024^{+0.0024}_{-0.0051}$	$0.0006^{+0.0004}_{-0.0026}$	$0.0056^{+0.0029}_{-0.0013}$
χ^2		443.6	444.1	457.3	451.0

5. MICROLENSING IN THE GAIA ERA: GAIA20BOF AND GAIA21BLX

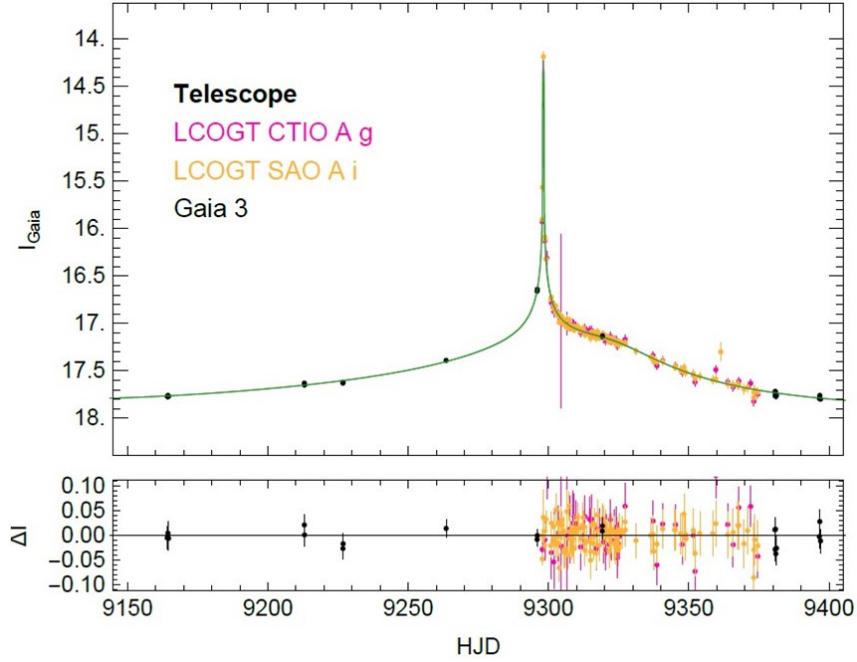


Figure 5.5: Lightcurve with residuals of the best model (called LOCloser) for the microlensing event Gaia21blx. (Rota et al. 2023 in prep.)

5.2.3 Constraint on the lens and discussion

From the four models we derive the source flux and the blend flux listed in Table 5.5. We can immediately note that the blend is very high for all the models and attribute it to the lens itself. Indeed the fact that the blend flux is generated by the lens is our first assumption (that in future can be confirmed by spectroscopic observations). In order to derive the physical parameters of the lens we also use the parallax measured by Gaia with the GAIA-DR3 release $\pi_{Gaia} = 0.45 \pm 0.13$ mas with a Re-normalised Unit Weight Error (RUWE) of 1.18 that is acceptable [177]. At this point we assume that the Gaia parallax is the flux-weighted average of the parallaxes of lens and source. The three parallaxes (π_{Gaia}, π_l and π_s) are related by the following equation:

$$\pi_s = \frac{\pi_{Gaia}(10^{-0.4G_s} + 10^{-0.4G_l}) - \pi_l 10^{-0.4G_l}}{10^{-0.4G_s}} \quad (5.1)$$

We make this hypothesis since the blending is high and probably the Gaia parallax does not correspond to the source or lens parallax only. With these two assumptions we can estimate separate information on lens and source and

5. MICROLENSING IN THE GAIA ERA: GAIA20BOF AND GAIA21BLX

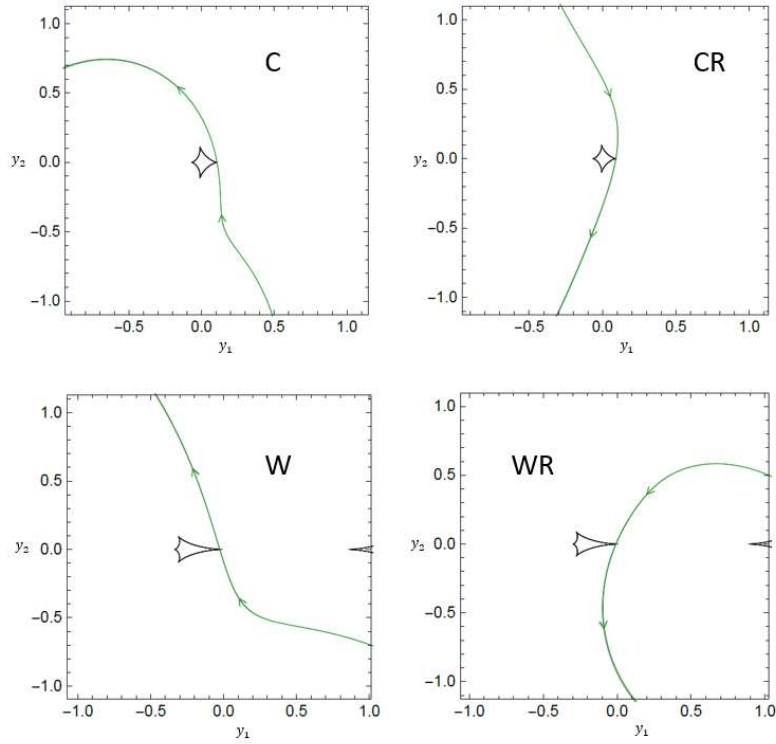


Figure 5.6: Caustic configuration for all the models. On the top we have the LOClose on the left (R) while on the right there is the LOCloseR (CR). On the bottom on the left we have the LOWide model (W) and then on the right the LOWideR model (WR). (Rota et al. 2023 in prep.)

restrict the physical range of the parameters.

The second step is to derive the magnitude in V band in order to derive a mass-luminosity relation for low-mass star. Using the relationship in Riello et al. [178] we derive the Gaia color $G_{BP} - G_{RP}$ from the color $g' - i'$ with the following equation:

$$G_{BP} - G_{RP} = 0.3971 + 0.777(g' - i') - 0.4164(g' - i')^2 + 0.008237(g' - i')^3 \quad (5.2)$$

Once we obtain the Gaia color from the equation (5.2) we take the equation that relates the G Gaia band with Johnson V band using the Gaia color in order to obtain the V magnitude for the lens:

5. MICROLENSING IN THE GAIA ERA: GAIA20BOF AND GAIA21BLX

Table 5.5: Magnitudes of baseline (source) and blend (lens flux for our assumption) of the best models for each telescope. Rota et al. 2023 in prep.

	Unit	LOcloseR	LOclose	LOWide	LOWideR
G_s	mag	19.544 ± 0.056	19.381 ± 0.101	18.354 ± 0.088	18.522 ± 0.103
G_l	mag	18.203 ± 0.016	18.257 ± 0.036	19.142 ± 0.183	18.859 ± 0.141
g_s	mag	21.259 ± 0.059	21.105 ± 0.106	20.099 ± 0.082	20.283 ± 0.102
g_l	mag	19.229 ± 0.009	19.261 ± 0.020	19.607 ± 0.052	19.501 ± 0.050
i_s	mag	19.119 ± 0.057	18.964 ± 0.104	17.961 ± 0.084	18.144 ± 0.106
i_l	mag	17.368 ± 0.012	17.413 ± 0.025	17.884 ± 0.078	17.733 ± 0.073

$$G-V = -0.02704 + 0.01424(G_{BP} - G_{RP}) - 0.2156(G_{BP} - G_{RP})^2 + 0.01426(G_{BP} - G_{RP})^3 \quad (5.3)$$

from which we obtain $V_{lens} = 18.84 \pm 0.05$. At this point we use the mass-luminosity relation of Xia et al. [179] where we include the extinction following the work of Capitanio et al. [180]. Since the lens is binary, we consider the two components separately using the following equations (in the end we sum the fluxes of the two lenses):

$$\text{Log}M = 0.213 - 0.0250M_V - 0.00275M_V^2 \text{ if } M \in (0.50, 1.086)M_\odot$$

$$\text{Log}M = 0.982 - 0.128M_V \text{ if } M \in [0.28, 0.50]M_\odot$$

$$\text{Log}M = 4.77 - 0.714M_V + 0.0224M_V^2 \text{ if } M \in (0.1, 0.28)M_\odot$$

In this way we construct a function of the mass depending on the distance with the inclusion of the extinction.

Another constraint arises from the source: following Boyajian et al. [181] we derive θ_* considering the color g'-i' that we use to derive the zero-magnitude angular diameter $\theta_{m_\lambda=0}$, that represents the angular diameter of a star when it is at a distance at which its apparent magnitude equals zero, using the following relation [181], [182]:

5. MICROLENSING IN THE GAIA ERA: GAIA20BOF AND GAIA21BLX

$$\log\theta_{m_\lambda=0} = \log\theta_{LD} + 0.2m_\lambda \quad (5.5)$$

where θ_{LD} is the angular diameter of the star (our θ_*) and m_λ is the apparent magnitude of a star in a certain filter λ . In this case we use the g' filter.

The parameter obtained, combined with ρ_* and the parallax gives us another relation between mass and distance explained in the following equation:

$$M = \left(\frac{\theta_*}{\rho_*}\right)^2 \frac{1}{\kappa(\pi_l - \pi_s)} \quad (5.6)$$

Finally we use a third constraint from microlensing where, using the parallax obtained from the Markov Chain we obtain again the mass as function of D_L :

$$M = \frac{\pi_l - \pi_s}{\kappa\pi_E^2} \quad (5.7)$$

The result is shown in Figure 5.7. With this approach we exclude the wide cases since there is no overlapping between the three bands allowed by the physical constraints. In this way we are able to obtain information about lens and source and list it in the Table 5.6.

A further reinforcement of this work is given to us by astrometry. Using the latest version of VBBinaryLensing of Bozza [21] we are able to simulate the astrometric microlensing of the event as shown in Figure 5.8. The fact that the baseline of Gaia data is very long compared to the microlensing duration and the absence of Gaia points during the amplification of the lightcurve strengthens the hypothesis that the parallax measured by Gaia is unaffected by microlensing and that can be considered the flux-weighted average of the parallaxes of lens and source. In conclusion we can say that with this approach we managed to extrapolate the information on the lens, discovering that it is a binary system distant 2.2 kpc with a total mass of $1.5 M_\odot$. The two lenses are probably a G-star of $0.95 M_\odot$ and a K-star of $0.52 M_\odot$. Using IAC-STAR with

5. MICROLENSING IN THE GAIA ERA: GAIA20BOF AND GAIA21BLX

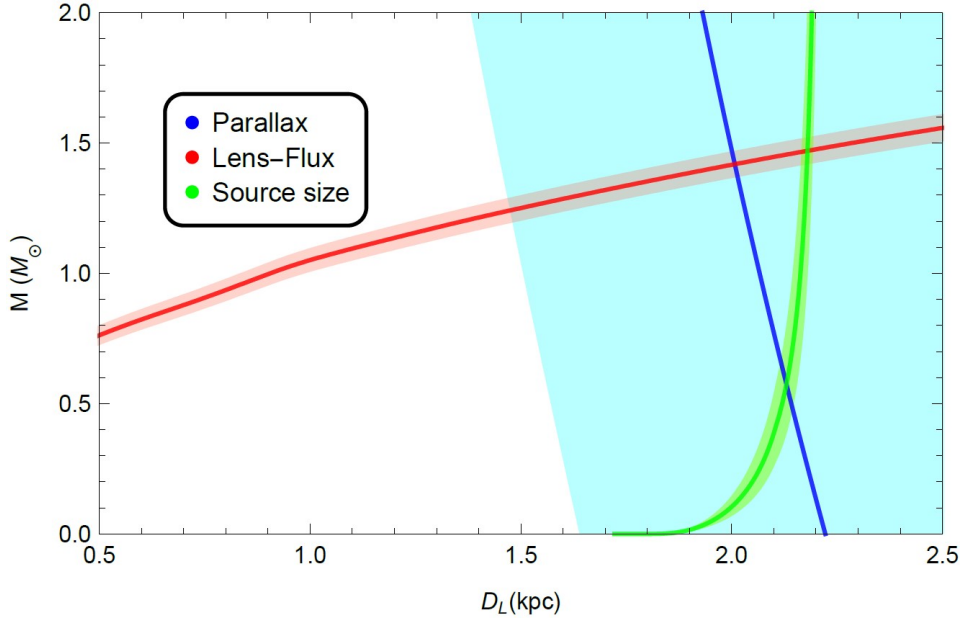


Figure 5.7: Plot of the three mass-distance functions for the LOCcloseR model. In blue we have the constraint from the microlensing and Gaia parallax. In red the constraint from the lens flux where mass-luminosity relations for low mass star are used. In green the constraint obtained from the finite source effects and the angular radius of the source. (Rota et al. 2023 in prep.)

the stellar evolution library of Girardi [183] we extrapolate the magnitude in the Johnson Cousin’s bands. In this way using the conversion from Johnson to SDSS band [184] we are able to obtain the g' and i' band for each lens and using the formulas present in [178] backwards, the magnitude is also obtained in the GAIA band. About the source we can assume that is distant about 2.4 kpc and probably it is a F-subgiant star. Spectroscopic observations should explicitly show the presence of lines from the source and at least the primary lens, which contributes most of the blending. Moreover, since the lens is bright we expect that with high resolution imaging we are able to separate, in future observations, the source and the lens making a further constraint on their physical properties.

5. MICROLENSING IN THE GAIA ERA: GAIA20BOF AND GAIA21BLX

Table 5.6: Physical parameters of lens and source for the best model. Rota et al. 2023 in prep.

	Distance (kpc)	Mass(M_{\odot})	g'	i'	G	Spectral class
Total lens	2.18 ± 0.02	1.47 ± 0.05	19.229 ± 0.009	17.368 ± 0.012	18.203 ± 0.016	-
Primary lens	2.18 ± 0.02	0.95 ± 0.06	20.373 ± 0.295	17.913 ± 0.295	18.217 ± 0.418	G star
Secondary lens	2.18 ± 0.02	0.52 ± 0.06	25.402 ± 0.278	20.765 ± 0.278	20.475 ± 0.394	K star
Source	2.38 ± 0.29	1.21 ± 0.43	21.259 ± 0.059	19.119 ± 0.057	19.544 ± 0.056	Subgiant F star

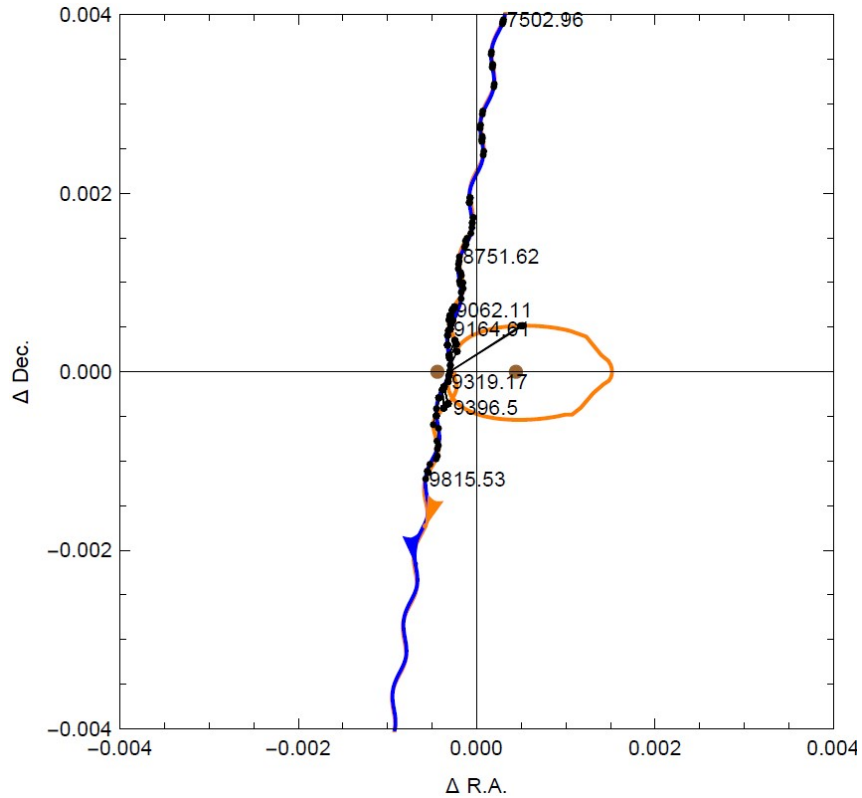


Figure 5.8: Astrometry simulation for the LOCcloseR model. (Rota et al. 2023 in prep.). The blue curve is the source trajectory in a frame in which the lenses are fixed. The orange curve shows the centroid trajectory. The two brown disk are the two lenses and the black points are the Gaia points. Rota et al. 2023 in prep.

CHAPTER 6

CONCLUSIONS

In this thesis I presented my work about the modeling of microlensing events. We started from the gravitational lensing theory introducing all the physical information needed to understand this physical scenario and we introduced all the techniques used to analyze a microlensing event in order to derive physical informations as the distance and the mass of the lens. After this we examined several microlensing event where for each of them, the usual procedure was used to obtain the final result: we start with RTModel to find the base models from which to start for the exploration of the parameter space to minimize the χ^2 with the Levenberg-Marquard algorithm and then find the best solutions with Markov Chains. The first event analyzed is MOA-2006-BLG-074: it was selected as a prominent exoplanetary event but after a detailed analysis we found that the lightcurve is better described by a binary source with orbital motion and a single lens whose properties are derived with a Bayesian analysis. The second event analyzed is OGLE-2019-BLG-033: in this case we have data from Spitzer satellite so from the beginning we have to consider satellite parallax and this allows us to find the physical parameters of the lens directly without having to resort to statistical analysis. In this case we find a binary system with a brown dwarf and the measurements are

6. CONCLUSIONS

so precise as to place this work among those with the greatest accuracy in determining the physical parameters of a binary system with brown dwarfs. In the end we analyzed two microlensing events detected by Gaia satellite: for the first, Gaia20bof, we find degenerate models, including even planetary solutions, which can be confirmed with high resolution imaging in order to detect separately lens and source and make a constraint on these. The second is Gaia21blx which turned out to be a binary system composed of one G-star and one K-star. The interesting aspect in this case was the fact that, given the presence of a high blending, which was assumed to be the lens flux, the solution of the system was obtained by considering the gaia parallax as the weighted average of the fluxes of the lens and source parallaxes. In this way, using the appropriate conversion formulas to pass into V band, for which mass-luminosity relationships are obtained for low mass stars we found several constraint for the lens coming from the parallax, the flux and from the finite source effects that are well measured in this event. Summing up we find that with microlensing we can have many different approaches that allow us to find the final solution of the event using an advanced modelling method. The importance of microlensing is also based on this and we remember that it is one of the few, if not the only method, capable of detecting faint or dark objects otherwise impossible to find with other techniques such as brown dwarfs, free floating planets, stellar black holes and more thus providing more precise and detailed information on the distribution of objects in the Milky Way and therefore providing information on the dynamics and evolution of our Galaxy. With the advent of telescopes such as the Roman telescope, microlensing will therefore become fundamental not only for the discovery of numerous exoplanets, in particular terrestrial ones, which are located beyond the snow line, but also for having more information on how our Galaxy is made, which despite the various surveys carried out in all this time, still remain hidden.

REFERENCES

- [1] B. Paczynski, “Gravitational Microlensing by the Galactic Halo,” vol. 304, p. 1, May 1986. DOI: 10.1086/164140.
- [2] C. Alcock, C. W. Akerlof, R. A. Allsman, *et al.*, “Possible gravitational microlensing of a star in the Large Magellanic Cloud,” vol. 365, no. 6447, pp. 621–623, Oct. 1993. DOI: 10.1038/365621a0. arXiv: astro-ph/9309052 [astro-ph].
- [3] E. Aubourg, P. Bareyre, S. Bréhin, *et al.*, “Evidence for gravitational microlensing by dark objects in the Galactic halo,” vol. 365, no. 6447, pp. 623–625, Oct. 1993. DOI: 10.1038/365623a0.
- [4] A. Udalski, M. Szymanski, J. Kaluzny, *et al.*, “The Optical Gravitational Lensing Experiment. Discovery of the First Candidate Microlensing Event in the Direction of the Galactic Bulge,” vol. 43, pp. 289–294, Jul. 1993.
- [5] S. Mao and B. Paczynski, “Gravitational Microlensing by Double Stars and Planetary Systems,” vol. 374, p. L37, Jun. 1991. DOI: 10.1086/186066.
- [6] A. Gould and A. Loeb, “Discovering Planetary Systems through Gravitational Microlenses,” vol. 396, p. 104, Sep. 1992. DOI: 10.1086/171700.

- [7] B. S. Gaudi, “Microlensing Surveys for Exoplanets,” vol. 50, pp. 411–453, Sep. 2012. DOI: 10.1146/annurev-astro-081811-125518.
- [8] S. Rahvar, “Gravitational microlensing I: A unique astrophysical tool,” *International Journal of Modern Physics D*, vol. 24, no. 7, 1530020, p. 1530020, Apr. 2015. DOI: 10.1142/S0218271815300207. arXiv: 1503.04271 [astro-ph.IM].
- [9] M. Meneghetti, *Introduction to Gravitational Lensing*. Springer International Publishing, 2021. DOI: 10.1007/978-3-030-73582-1. [Online]. Available: <https://doi.org/10.10072F978-3-030-73582-1>.
- [10] Y. Tsapras, “Microlensing Searches for Exoplanets,” *Geosciences*, vol. 8, no. 10, p. 365, Sep. 2018. DOI: 10.3390/geosciences8100365. arXiv: 1810.02691 [astro-ph.EP].
- [11] T. Sumi, D. P. Bennett, I. A. Bond, *et al.*, “The Microlensing Event Rate and Optical Depth toward the Galactic Bulge from MOA-II,” vol. 778, no. 2, 150, p. 150, Dec. 2013. DOI: 10.1088/0004-637X/778/2/150. arXiv: 1305.0186 [astro-ph.GA].
- [12] C. H. Lee, S. Seitz, A. Riffeser, and R. Bender, “Finite-source and finite-lens effects in astrometric microlensing,” vol. 407, no. 3, pp. 1597–1608, Sep. 2010. DOI: 10.1111/j.1365-2966.2010.17049.x. arXiv: 1005.3021 [astro-ph.CO].
- [13] C. Badenes, C. Mazzola, T. A. Thompson, *et al.*, “Stellar Multiplicity Meets Stellar Evolution and Metallicity: The APOGEE View,” vol. 854, no. 2, 147, p. 147, Feb. 2018. DOI: 10.3847/1538-4357/aaa765. arXiv: 1711.00660 [astro-ph.SR].
- [14] H. J. Witt, “Investigation of high amplification events in light curves of gravitationally lensed quasars.,” vol. 236, p. 311, Sep. 1990.

- [15] M. Dominik, “Ambiguities in FITS of observed binary lens galactic microlensing events,” , vol. 341, pp. 943–953, Jan. 1999. arXiv: astro-ph/9703003 [astro-ph].
- [16] A. Gould, “Extending the MACHO Search to approximately 10⁶ M sub sun,” , vol. 392, p. 442, Jun. 1992. DOI: 10.1086/171443.
- [17] A. Gould, “Resolution of the MACHO-LMC-5 Puzzle: The Jerk-Parallax Microlens Degeneracy,” , vol. 606, no. 1, pp. 319–325, May 2004. DOI: 10.1086/382782. arXiv: astro-ph/0311548 [astro-ph].
- [18] J. C. Yee, A. Udalski, S. Calchi Novati, *et al.*, “First Space-based Microlens Parallax Measurement of an Isolated Star: Spitzer Observations of OGLE-2014-BLG-0939,” , vol. 802, no. 2, 76, p. 76, Apr. 2015. DOI: 10.1088/0004-637X/802/2/76. arXiv: 1410.5429 [astro-ph.SR].
- [19] C. Han, A. Udalski, A. Gould, *et al.*, “OGLE-2015-BLG-0479LA,B: Binary Gravitational Microlens Characterized by Simultaneous Ground-based and Space-based Observations,” , vol. 828, no. 1, 53, p. 53, Sep. 2016. DOI: 10.3847/0004-637X/828/1/53. arXiv: 1606.09357 [astro-ph.SR].
- [20] J. Skowron, A. Udalski, A. Gould, *et al.*, “Binary Microlensing Event OGLE-2009-BLG-020 Gives Verifiable Mass, Distance, and Orbit Predictions,” , vol. 738, no. 1, 87, p. 87, Sep. 2011. DOI: 10.1088/0004-637X/738/1/87. arXiv: 1101.3312 [astro-ph.SR].
- [21] V. Bozza, E. Khalouei, and E. Bachelet, “A public code for astrometric microlensing with contour integration,” , vol. 505, no. 1, pp. 126–135, Jul. 2021. DOI: 10.1093/mnras/stab1376. arXiv: 2011.04780 [astro-ph.IM].
- [22] K. Griest and W. Hu, “Effect of Binary Sources on the Search for Massive Astrophysical Compact Halo Objects via Microlensing,” , vol. 397, p. 362, Oct. 1992. DOI: 10.1086/171793.

- [23] C. Alcock, R. A. Allsman, D. R. Alves, *et al.*, “MACHO 96-LMC-2: Lensing of a Binary Source in the Large Magellanic Cloud and Constraints on the Lensing Object,”, vol. 552, no. 1, pp. 259–267, May 2001. DOI: 10.1086/320457. arXiv: astro-ph/0012163 [astro-ph].
- [24] S. Rahvar and M. Dominik, “Detecting exoplanets with the xallarap microlensing effect,” in *Manchester Microlensing Conference*, E. Kerins, S. Mao, N. Rattenbury, and L. Wyrzykowski, Eds., Jan. 2008, 37, p. 37. DOI: 10.22323/1.054.0037.
- [25] C. Han, I. A. Bond, A. Gould, *et al.*, “Moa-2016-blg-319lb: Microlensing planet subject to rare minor-image perturbation degeneracy in determining planet parameters,” *The Astronomical Journal*, vol. 156, no. 5, p. 226, Oct. 2018. DOI: 10.3847/1538-3881/aae38e. [Online]. Available: <https://dx.doi.org/10.3847/1538-3881/aae38e>.
- [26] K. Zhang, B. S. Gaudi, and J. S. Bloom, “A ubiquitous unifying degeneracy in two-body microlensing systems,” *Nature Astronomy*, vol. 6, pp. 782–787, May 2022. DOI: 10.1038/s41550-022-01671-6. arXiv: 2111.13696 [astro-ph.EP].
- [27] B. S. Gaudi and A. Gould, “Planet Parameters in Microlensing Events,”, vol. 486, no. 1, pp. 85–99, Sep. 1997. DOI: 10.1086/304491. arXiv: astro-ph/9610123 [astro-ph].
- [28] A. Gould, “MACHO Velocities from Satellite-based Parallaxes,”, vol. 421, p. L75, Feb. 1994. DOI: 10.1086/187191.
- [29] S. Poindexter, C. Afonso, D. P. Bennett, *et al.*, “Systematic Analysis of 22 Microlensing Parallax Candidates,”, vol. 633, no. 2, pp. 914–930, Nov. 2005. DOI: 10.1086/468182. arXiv: astro-ph/0506183 [astro-ph].
- [30] *Methods of Detecting Exoplanets*, vol. 428, Astrophysics and Space Science Library, Jan. 2016. DOI: 10.1007/978-3-319-27458-4.

- [31] S. Calchi Novati, A. Gould, J. C. Yee, *et al.*, “Spitzer IRAC Photometry for Time Series in Crowded Fields,” vol. 814, no. 2, 92, p. 92, Dec. 2015. DOI: 10.1088/0004-637X/814/2/92. arXiv: 1509.00037 [astro-ph.EP].
- [32] P. H. Frampton, M. Kawasaki, F. Takahashi, and T. T. Yanagida, “Primordial black holes as all dark matter,” vol. 2010, no. 4, 023, p. 023, Apr. 2010. DOI: 10.1088/1475-7516/2010/04/023. arXiv: 1001.2308 [hep-ph].
- [33] A. Udalski and M. Szymanski, “Possible Microlensing in the Galactic Bulge,” vol. 6164, p. 1, Apr. 1995.
- [34] A. Udalski, M. K. Szymański, and G. Szymański, “OGLE-IV: Fourth Phase of the Optical Gravitational Lensing Experiment,” vol. 65, no. 1, pp. 1–38, Mar. 2015. arXiv: 1504.05966 [astro-ph.SR].
- [35] A. Udalski, M. Szymanski, J. Kaluzny, *et al.*, “The Optical Gravitational Lensing Experiment. The Early Warning System: Real Time Microlensing,” vol. 44, pp. 227–234, Jul. 1994. arXiv: astro-ph/9408026 [astro-ph].
- [36] I. A. Bond, A. Udalski, M. Jaroszyński, *et al.*, “OGLE 2003-BLG-235/MOA 2003-BLG-53: A Planetary Microlensing Event,” vol. 606, no. 2, pp. L155–L158, May 2004. DOI: 10.1086/420928. arXiv: astro-ph/0404309 [astro-ph].
- [37] K. C. Sahu, J. Anderson, S. Casertano, *et al.*, “An Isolated Stellar-mass Black Hole Detected through Astrometric Microlensing,” vol. 933, no. 1, 83, p. 83, Jul. 2022. DOI: 10.3847/1538-4357/ac739e. arXiv: 2201.13296 [astro-ph.SR].
- [38] S.-L. Kim, C.-U. Lee, B.-G. Park, *et al.*, “KMTNET: A Network of 1.6 m Wide-Field Optical Telescopes Installed at Three Southern Observatories,” *Journal of Korean Astronomical Society*, vol. 49, no. 1, pp. 37–44, Feb. 2016. DOI: 10.5303/JKAS.2016.49.1.37.

- [39] J. C. Yee, A. Gould, C. Beichman, *et al.*, “Criteria for Sample Selection to Maximize Planet Sensitivity and Yield from Space-Based Microlens Parallax Surveys,”, vol. 810, no. 2, 155, p. 155, Sep. 2015. DOI: 10.1088/0004-637X/810/2/155. arXiv: 1505.00014 [astro-ph.EP].
- [40] W. Zang, Y. Shvartzvald, T. Wang, *et al.*, “Spitzer Microlensing Parallax Reveals Two Isolated Stars in the Galactic Bulge,”, vol. 891, no. 1, 3, p. 3, Mar. 2020. DOI: 10.3847/1538-4357/ab6ff8. arXiv: 1904.11204 [astro-ph.SR].
- [41] W. Zhu, S. Calchi Novati, A. Gould, *et al.*, “Mass Measurements of Isolated Objects from Space-based Microlensing,”, vol. 825, no. 1, 60, p. 60, Jul. 2016. DOI: 10.3847/0004-637X/825/1/60. arXiv: 1510.02097 [astro-ph.SR].
- [42] S. -. Chung, W. Zhu, A. Udalski, *et al.*, “OGLE-2015-BLG-1482L: The First Isolated Low-mass Microlens in the Galactic Bulge,”, vol. 838, no. 2, 154, p. 154, Apr. 2017. DOI: 10.3847/1538-4357/aa67fa. arXiv: 1703.05887 [astro-ph.SR].
- [43] I. -. Shin, A. Udalski, J. C. Yee, *et al.*, “OGLE-2016-BLG-1045: A Test of Cheap Space-based Microlens Parallaxes,”, vol. 863, no. 1, 23, p. 23, Aug. 2018. DOI: 10.3847/1538-4357/aacdf4. arXiv: 1801.00169 [astro-ph.SR].
- [44] S. -. Li, W. Zang, A. Udalski, *et al.*, “OGLE-2017-BLG-1186: first application of asteroseismology and Gaussian processes to microlensing,”, vol. 488, no. 3, pp. 3308–3323, Sep. 2019. DOI: 10.1093/mnras/stz1873. arXiv: 1904.07718 [astro-ph.SR].
- [45] K. Griest, M. J. Lehner, A. M. Cieplak, and B. Jain, “Microlensing of Kepler Stars as a Method of Detecting Primordial Black Hole Dark Matter,”, vol. 107, no. 23, 231101, p. 231 101, Dec. 2011. DOI: 10.1103/PhysRevLett.107.231101. arXiv: 1109.4975 [astro-ph.CO].

- [46] C. B. Henderson, R. Poleski, M. Penny, *et al.*, “Campaign 9 of the K2 Mission: Observational Parameters, Scientific Drivers, and Community Involvement for a Simultaneous Space- and Ground-based Microlensing Survey,” , vol. 128, no. 970, p. 124 401, Dec. 2016. DOI: 10.1088/1538-3873/128/970/124401. arXiv: 1512.09142 [astro-ph.EP].
- [47] Gaia Collaboration, T. Prusti, J. H. J. de Bruijne, *et al.*, “The Gaia mission,” , vol. 595, A1, A1, Nov. 2016. DOI: 10.1051/0004-6361/201629272. arXiv: 1609.04153 [astro-ph.IM].
- [48] L. Wyrzykowski, P. Mróz, K. A. Rybicki, *et al.*, “Full orbital solution for the binary system in the northern Galactic disc microlensing event Gaia16aye,” , vol. 633, A98, A98, Jan. 2020. DOI: 10.1051/0004-6361/201935097. arXiv: 1901.07281 [astro-ph.SR].
- [49] L. Wyrzykowski, K. Kruszyńska, K. A. Rybicki, *et al.*, “Gaia Data Release 3: Microlensing Events from All Over the Sky,” *arXiv e-prints*, arXiv:2206.06121, arXiv:2206.06121, Jun. 2022. arXiv: 2206.06121 [astro-ph.SR].
- [50] V. A. Belokurov and N. W. Evans, “Astrometric microlensing with the GAIA satellite,” *Monthly Notices of the Royal Astronomical Society*, vol. 331, no. 3, pp. 649–665, Apr. 2002, ISSN: 0035-8711. DOI: 10.1046/j.1365-8711.2002.05222.x. eprint: <https://academic.oup.com/mnras/article-pdf/331/3/649/3362935/331-3-649.pdf>. [Online]. Available: <https://doi.org/10.1046/j.1365-8711.2002.05222.x>.
- [51] M. T. Penny, B. S. Gaudi, E. Kerins, *et al.*, “Predictions of the WFIRST Microlensing Survey. I. Bound Planet Detection Rates,” , vol. 241, no. 1, 3, p. 3, Mar. 2019. DOI: 10.3847/1538-4365/aafb69. arXiv: 1808.02490 [astro-ph.EP].
- [52] E. Bachelet, D. Specht, M. Penny, *et al.*, “Euclid-Roman joint microlensing survey: Early mass measurement, free floating planets, and exomoons,” , vol. 664, A136, A136, Aug. 2022. DOI: 10.1051/0004-6361/202140351. arXiv: 2202.09475 [astro-ph.EP].

- [53] A. Vandorou, D. P. Bennett, J.-P. Beaulieu, *et al.*, “Revisiting MOA 2013-BLG-220L: A Solar-type Star with a Cold Super-Jupiter Companion,” vol. 160, no. 3, p. 121, Sep. 2020. DOI: 10.3847/1538-3881/aba2d3. arXiv: 1909.04444 [astro-ph.EP].
- [54] M. Dominik, M. D. Albrow, J. -. Beaulieu, *et al.*, “The PLANET microlensing follow-up network: Results and prospects for the detection of extra-solar planets,” *arXiv e-prints*, astro-ph/9910465, astro-ph/9910465, Oct. 1999. DOI: 10.48550/arXiv.astro-ph/9910465. arXiv: astro-ph/9910465 [astro-ph].
- [55] A. Gould, “MicroFUN 2007,” in *Manchester Microlensing Conference*, E. Kerins, S. Mao, N. Rattenbury, and L. Wyrzykowski, Eds., Jan. 2008, 38, p. 38. DOI: 10.22323/1.054.0038.
- [56] R. Kayser, S. Refsdal, and R. Stabell, “Astrophysical applications of gravitational micro-lensing.,” vol. 166, pp. 36–52, Sep. 1986.
- [57] V. Bozza, “Microlensing with an advanced contour integration algorithm: Green’s theorem to third order, error control, optimal sampling and limb darkening,” *Monthly Notices of the Royal Astronomical Society*, vol. 408, no. 4, pp. 2188–2200, Oct. 2010, ISSN: 0035-8711. DOI: 10.1111/j.1365-2966.2010.17265.x. eprint: <https://academic.oup.com/mnras/article-pdf/408/4/2188/4222270/mnras0408-2188.pdf>. [Online]. Available: <https://doi.org/10.1111/j.1365-2966.2010.17265.x>.
- [58] E. A. Milne, “Radiative equilibrium in the outer layers of a star,” vol. 81, pp. 361–375, Mar. 1921. DOI: 10.1093/mnras/81.5.361.
- [59] V. Bozza, E. Bachelet, F. Bartolić, T. M. Heintz, A. R. Hoag, and M. Hundertmark, “VBBINARYLENSING: a public package for microlensing light-curve computation,” vol. 479, no. 4, pp. 5157–5167, Oct. 2018. DOI: 10.1093/mnras/sty179110.48550/arXiv.1805.05653. arXiv: 1805.05653 [astro-ph.IM].

- [60] O. Pejcha and D. Heyrovský, “Extended-Source Effect and Chromaticity in Two-Point-Mass Microlensing,” vol. 690, no. 2, pp. 1772–1796, Jan. 2009. DOI: 10.1088/0004-637X/690/2/177210. 48550/arXiv.0712.2217. arXiv: 0712.2217 [astro-ph].
- [61] V. Bozza, “Perturbative analysis in planetary gravitational lensing,” vol. 348, pp. 311–326, Aug. 1999. DOI: 10.48550/arXiv.astro-ph/9904297. arXiv: astro-ph/9904297 [astro-ph].
- [62] V. Bozza, “Caustics in special multiple lenses,” vol. 355, pp. 423–432, Mar. 2000. DOI: 10.48550/arXiv.astro-ph/9910535. arXiv: astro-ph/9910535 [astro-ph].
- [63] M. Dominik, K. Horne, A. Allan, *et al.*, “ARTEMiS (Automated Robotic Terrestrial Exoplanet Microlensing Search): A possible expert-system based cooperative effort to hunt for planets of Earth mass and below,” *Astronomische Nachrichten*, vol. 329, no. 3, p. 248, Mar. 2008. DOI: 10.1002/asna.200710928. arXiv: 0801.2162 [astro-ph].
- [64] H. P. Gavin, “The levenberg-marquardt algorithm for nonlinear least squares curve-fitting problems,” 2019.
- [65] B. Sericola, “Markov chains. theory, algorithms and applications,” 2013.
- [66] J. Besag, “Markov chain monte carlo methods for statistical inference,” 2004.
- [67] B. Paczynski, “Binary Source Parallactic Effect in Gravitational Micro-lensing,” *arXiv e-prints*, astro-ph/9711007, astro-ph/9711007, Nov. 1997. DOI: 10.48550/arXiv.astro-ph/9711007. arXiv: astro-ph/9711007 [astro-ph].
- [68] N. Palanque-Delabrouille, C. Afonso, J. N. Albert, *et al.*, “Microlensing towards the Small Magellanic Cloud EROS 2 first year survey,” vol. 332, pp. 1–9, Apr. 1998. DOI: 10.48550/arXiv.astro-ph/9710194. arXiv: astro-ph/9710194 [astro-ph].

- [69] EROS Collaboration, F. Derue, C. Afonso, *et al.*, “Observation of microlensing towards the galactic spiral arms. EROS II. 2 year survey,” , vol. 351, pp. 87–96, Nov. 1999. DOI: 10.48550/arXiv.astro-ph/9903209. arXiv: astro-ph/9903209 [astro-ph].
- [70] C. Alcock, R. A. Allsman, D. Alves, *et al.*, “First Observation of Parallax in a Gravitational Microlensing Event,” , vol. 454, p. L125, Dec. 1995. DOI: 10.1086/309783. arXiv: astro-ph/9506114 [astro-ph].
- [71] M. C. Smith, S. Mao, and B. Paczyński, “Acceleration and parallax effects in gravitational microlensing,” , vol. 339, no. 4, pp. 925–936, Mar. 2003. DOI: 10.1046/j.1365-8711.2003.06183.x. arXiv: astro-ph/0210370 [astro-ph].
- [72] H. Ghosh, D. L. DePoy, A. Gal-Yam, *et al.*, “Potential Direct Single-Star Mass Measurement,” , vol. 615, no. 1, pp. 450–459, Nov. 2004. DOI: 10.1086/423665. arXiv: astro-ph/0405500 [astro-ph].
- [73] D. P. Bennett, I. A. Bond, A. Udalski, *et al.*, “A Low-Mass Planet with a Possible Sub-Stellar-Mass Host in Microlensing Event MOA-2007-BLG-192,” , vol. 684, no. 1, pp. 663–683, Sep. 2008. DOI: 10.1086/589940. arXiv: 0806.0025 [astro-ph].
- [74] K. -. Hwang, C. Han, I. A. Bond, *et al.*, “Determining the Physical Lens Parameters of the Binary Gravitational Microlensing Event MOA-2009-BLG-016,” , vol. 717, no. 1, pp. 435–440, Jul. 2010. DOI: 10.1088/0004-637X/717/1/435. arXiv: 1006.1396 [astro-ph.SR].
- [75] N. Miyake, A. Udalski, T. Sumi, *et al.*, “A Possible Binary System of a Stellar Remnant in the High-magnification Gravitational Microlensing Event OGLE-2007-BLG-514,” , vol. 752, no. 2, 82, p. 82, Jun. 2012. DOI: 10.1088/0004-637X/752/2/82. arXiv: 1207.1244 [astro-ph.EP].
- [76] K. Furusawa, A. Udalski, T. Sumi, *et al.*, “MOA-2010-BLG-328Lb: A Sub-Neptune Orbiting very Late M Dwarf?” , vol. 779, no. 2, 91, p. 91, Dec. 2013. DOI: 10.1088/0004-637X/779/2/91. arXiv: 1309.7714 [astro-ph.EP].

- [77] N. Koshimoto, A. Udalski, J. P. Beaulieu, *et al.*, “OGLE-2012-BLG-0950Lb: The First Planet Mass Measurement from Only Microlens Parallax and Lens Flux,”, vol. 153, no. 1, 1, p. 1, Jan. 2017. DOI: 10.3847/1538-3881/153/1/1. arXiv: 1607.03267 [astro-ph.EP].
- [78] C. Han and A. Gould, “Einstein Radii from Binary-Source Lensing Events,”, vol. 480, no. 1, pp. 196–202, May 1997. DOI: 10.1086/303944. arXiv: astro-ph/9604031 [astro-ph].
- [79] C. Han, Y. K. Jung, A. Udalski, *et al.*, “Microlensing Discovery of a Tight, Low-mass-ratio Planetary-mass Object around an Old Field Brown Dwarf,”, vol. 778, no. 1, 38, p. 38, Nov. 2013. DOI: 10.1088/0004-637X/778/1/38. arXiv: 1307.6335 [astro-ph.EP].
- [80] N. Kains, R. A. Street, J. -. Choi, *et al.*, “A giant planet beyond the snow line in microlensing event OGLE-2011-BLG-0251,”, vol. 552, A70, A70, Apr. 2013. DOI: 10.1051/0004-6361/201220626. arXiv: 1303.1184 [astro-ph.EP].
- [81] Y. H. Kim, S.-J. Chung, A. Udalski, *et al.*, “OGLE-2018-BLG-1428Lb: a Jupiter-mass planet beyond the snow line of a dwarf star,”, vol. 503, no. 2, pp. 2706–2712, May 2021. DOI: 10.1093/mnras/stab534. arXiv: 2102.11463 [astro-ph.EP].
- [82] S. Dong, A. Gould, A. Udalski, *et al.*, “OGLE-2005-BLG-071Lb, the Most Massive M Dwarf Planetary Companion?,”, vol. 695, no. 2, pp. 970–987, Apr. 2009. DOI: 10.1088/0004-637X/695/2/970. arXiv: 0804.1354 [astro-ph].
- [83] K. -. Hwang, C. Han, A. Udalski, *et al.*, “OGLE-2009-BLG-023/MOA-2009-BLG-028: characterization of a binary microlensing event based on survey data,”, vol. 413, no. 2, pp. 1244–1250, May 2011. DOI: 10.1111/j.1365-2966.2011.18206.x. arXiv: 1104.5091 [astro-ph.SR].

- [84] C. J. Lada, “Stellar Multiplicity and the Initial Mass Function: Most Stars Are Single,”, vol. 640, no. 1, pp. L63–L66, Mar. 2006. DOI: 10.1086/503158. arXiv: astro-ph/0601375 [astro-ph].
- [85] T. Sumi, D. P. Bennett, I. A. Bond, *et al.*, “A Cold Neptune-Mass Planet OGLE-2007-BLG-368Lb: Cold Neptunes Are Common,”, vol. 710, no. 2, pp. 1641–1653, Feb. 2010. DOI: 10.1088/0004-637X/710/2/1641. arXiv: 0912.1171 [astro-ph.EP].
- [86] D. P. Bennett, A. Udalski, C. Han, *et al.*, “The First Planetary Microlensing Event with Two Microlensed Source Stars,”, vol. 155, no. 3, 141, p. 141, Mar. 2018. DOI: 10.3847/1538-3881/aaadfa. arXiv: 1707.09667 [astro-ph.EP].
- [87] S. Miyazaki, T. Sumi, D. P. Bennett, *et al.*, “OGLE-2013-BLG-0911Lb: A Secondary on the Brown-dwarf Planet Boundary around an M Dwarf,”, vol. 159, no. 2, 76, p. 76, Feb. 2020. DOI: 10.3847/1538-3881/ab64de. arXiv: 1912.09613 [astro-ph.EP].
- [88] W. Zhu, A. Udalski, S. C. Novati, *et al.*, “Toward a Galactic Distribution of Planets. I. Methodology and Planet Sensitivities of the 2015 High-cadence Spitzer Microlens Sample,”, vol. 154, no. 5, 210, p. 210, Nov. 2017. DOI: 10.3847/1538-3881/aa8ef1. arXiv: 1701.05191 [astro-ph.EP].
- [89] S. Rahvar and M. Dominik, “Planetary microlensing signals from the orbital motion of the source star around the common barycentre,”, vol. 392, no. 3, pp. 1193–1204, Jan. 2009. DOI: 10.1111/j.1365-2966.2008.14120.x. arXiv: 0810.3915 [astro-ph].
- [90] F. Bagheri, S. Sajadian, and S. Rahvar, “Detection of exoplanet as a binary source of microlensing events in WFIRST survey,”, vol. 490, no. 2, pp. 1581–1587, Dec. 2019. DOI: 10.1093/mnras/stz2682. arXiv: 1909.11559 [astro-ph.EP].

- [91] S. Miyazaki, S. A. Johnson, T. Sumi, M. T. Penny, N. Koshimoto, and T. Yamawaki, “Revealing Short-period Exoplanets and Brown Dwarfs in the Galactic Bulge Using the Microlensing Xallarap Effect with the Nancy Grace Roman Space Telescope,” , vol. 161, no. 2, 84, p. 84, Feb. 2021. DOI: 10 . 3847 / 1538 - 3881 / abcec2. arXiv: 2010 . 10315 [astro-ph.EP].
- [92] K. -. Hwang, A. Udalski, I. A. Bond, *et al.*, “OGLE-2015-BLG-1459L: The Challenges of Exo-moon Microlensing,” , vol. 155, no. 6, 259, p. 259, Jun. 2018. DOI: 10 . 3847 / 1538 - 3881 / aac2cb. arXiv: 1711 . 09651 [astro-ph.EP].
- [93] I. A. Bond, F. Abe, R. J. Dodd, *et al.*, “Real-time difference imaging analysis of MOA Galactic bulge observations during 2000,” , vol. 327, no. 3, pp. 868–880, Nov. 2001. DOI: 10 . 1046 / j . 1365 - 8711 . 2001 . 04776 . x. arXiv: astro-ph/0102181 [astro-ph].
- [94] T. Sumi, F. Abe, I. A. Bond, *et al.*, “Microlensing Optical Depth toward the Galactic Bulge from Microlensing Observations in Astrophysics Group Observations during 2000 with Difference Image Analysis,” , vol. 591, no. 1, pp. 204–227, Jul. 2003. DOI: 10 . 1086 / 375212. arXiv: astro-ph/0207604 [astro-ph].
- [95] A. Udalski, “The Optical Gravitational Lensing Experiment. Real Time Data Analysis Systems in the OGLE-III Survey,” , vol. 53, pp. 291–305, Dec. 2003. DOI: 10 . 48550 / arXiv . astro-ph / 0401123. arXiv: astro-ph/0401123 [astro-ph].
- [96] D. P. Bennett, “An Efficient Method for Modeling High-magnification Planetary Microlensing Events,” , vol. 716, no. 2, pp. 1408–1422, Jun. 2010. DOI: 10 . 1088 / 0004 - 637X / 716 / 2 / 1408. arXiv: 0911 . 2703 [astro-ph.EP].
- [97] S. Mao and R. Di Stefano, “Interpretation of Gravitational Microlensing by Binary Systems,” , vol. 440, p. 22, Feb. 1995. DOI: 10 . 1086 / 175244.

- [98] K. Griest and N. Safizadeh, “The Use of High-Magnification Microlensing Events in Discovering Extrasolar Planets,” , vol. 500, no. 1, pp. 37–50, Jun. 1998. DOI: 10.1086/305729. arXiv: astro-ph/9710342 [astro-ph].
- [99] M. Dominik, “The binary gravitational lens and its extreme cases,” , vol. 349, pp. 108–125, Sep. 1999. DOI: 10.48550/arXiv.astro-ph/9903014. arXiv: astro-ph/9903014 [astro-ph].
- [100] P. Rota, Y. Hirao, V. Bozza, *et al.*, “MOA-2006-BLG-074: Recognizing Xallarap Contaminants in Planetary Microlensing,” , vol. 162, no. 2, 59, p. 59, Aug. 2021. DOI: 10.3847/1538-3881/ac0155. arXiv: 2105.08386 [astro-ph.EP].
- [101] B. Carroll and D. Ostlie, *An Introduction to Modern Astrophysics* (Pearson custom library). Pearson, 2014, ISBN: 9781292022932. [Online]. Available: <https://books.google.it/books?id=RLwangEACAAJ>.
- [102] M. K. Szymański, A. Udalski, I. Soszyński, *et al.*, “The Optical Gravitational Lensing Experiment. OGLE-III Photometric Maps of the Galactic Bulge Fields,” , vol. 61, no. 2, pp. 83–102, Jun. 2011. DOI: 10.48550/arXiv.1107.4008. arXiv: 1107.4008 [astro-ph.SR].
- [103] T. Bensby, D. Adén, J. Meléndez, *et al.*, “Chemical evolution of the Galactic bulge as traced by microlensed dwarf and subgiant stars. IV. Two bulge populations,” , vol. 533, A134, A134, Sep. 2011. DOI: 10.1051/0004-6361/201117059. arXiv: 1107.5606 [astro-ph.GA].
- [104] D. M. Nataf, A. Gould, P. Fouqué, *et al.*, “Reddening and Extinction toward the Galactic Bulge from OGLE-III: The Inner Milky Way’s $R_V \sim 2.5$ Extinction Curve,” , vol. 769, no. 2, 88, p. 88, Jun. 2013. DOI: 10.1088/0004-637X/769/2/88. arXiv: 1208.1263 [astro-ph.GA].
- [105] M. S. Bessell and J. M. Brett, “JHKLM Photometry: Standard Systems, Passbands, and Intrinsic Colors,” , vol. 100, p. 1134, Sep. 1988. DOI: 10.1086/132281.

- [106] P. Kervella, F. Thévenin, E. Di Folco, and D. Ségransan, “The angular sizes of dwarf stars and subgiants. Surface brightness relations calibrated by interferometry,” vol. 426, pp. 297–307, Oct. 2004. DOI: 10 . 1051 / 0004 - 6361 : 20035930. arXiv: astro - ph / 0404180 [astro-ph].
- [107] A. Aparicio and C. Gallart, “IAC-STAR: A Code for Synthetic Color-Magnitude Diagram Computation,” vol. 128, no. 3, pp. 1465–1477, Sep. 2004. DOI: 10 . 1086 / 382836. arXiv: astro - ph/0407589 [astro-ph].
- [108] G. Bertelli, A. Bressan, C. Chiosi, F. Fagotto, and E. Nasi, “Theoretical isochrones from models with new radiative opacities,” vol. 106, pp. 275–302, Aug. 1994.
- [109] F. Castelli and R. L. Kurucz, “New Grids of ATLAS9 Model Atmospheres,” in *Modelling of Stellar Atmospheres*, N. Piskunov, W. W. Weiss, and D. F. Gray, Eds., vol. 210, Jan. 2003, A20. DOI: 10 . 48550 / arXiv . astro - ph / 0405087. arXiv: astro - ph / 0405087 [astro-ph].
- [110] M. Dominik, “Stochastic distributions of lens and source properties for observed galactic microlensing events,” vol. 367, no. 2, pp. 669–692, Apr. 2006. DOI: 10.1111/j.1365-2966.2006.10004.x. arXiv: astro-ph/0507540 [astro-ph].
- [111] J. Zhang, W. Zang, Y. K. Jung, *et al.*, “KMT-2022-BLG-0440Lb: A New $q < 10^{-4}$ Microlensing Planet with the Central-Resonant Caustic Degeneracy Broken,” *arXiv e-prints*, arXiv:2301.06779, arXiv:2301.06779, Jan. 2023. DOI: 10 . 48550 / arXiv . 2301 . 06779. arXiv: 2301.06779 [astro-ph.EP].
- [112] K.-H. Hwang, J.-Y. Choi, I. A. Bond, *et al.*, “Interpretation of a short-term anomaly in the gravitational microlensing event moa-2012-blg-486,” *The Astrophysical Journal*, vol. 778, no. 1, p. 55,

- Nov. 2013. DOI: 10.1088/0004-637X/778/1/55. [Online]. Available: <https://dx.doi.org/10.1088/0004-637X/778/1/55>.
- [113] Y. K. Jung, A. Udalski, J. C. Yee, *et al.*, “Binary source microlensing event ogle-2016-blg-0733: Interpretation of a long-term asymmetric perturbation,” *The Astronomical Journal*, vol. 153, no. 3, p. 129, Feb. 2017. DOI: 10.3847/1538-3881/aa5d07. [Online]. Available: <https://dx.doi.org/10.3847/1538-3881/aa5d07>.
- [114] S. Auddy, S. Basu, and S. R. Valluri, “Analytic Models of Brown Dwarfs and the Substellar Mass Limit,” *Advances in Astronomy*, vol. 2016, 574327, p. 574327, Jan. 2016. DOI: 10.1155/2016/5743272. arXiv: 1607.04338 [astro-ph.SR].
- [115] A. Burrows, M. Marley, W. B. Hubbard, *et al.*, “A Nongray Theory of Extrasolar Giant Planets and Brown Dwarfs,” vol. 491, no. 2, pp. 856–875, Dec. 1997. DOI: 10.1086/305002. arXiv: astro-ph/9705201 [astro-ph].
- [116] D. S. Spiegel, A. Burrows, and J. A. Milsom, “The Deuterium-burning Mass Limit for Brown Dwarfs and Giant Planets,” vol. 727, no. 1, 57, p. 57, Jan. 2011. DOI: 10.1088/0004-637X/727/1/57. arXiv: 1008.5150 [astro-ph.EP].
- [117] V. J. S. Béjar, E. L. Martín, M. R. Zapatero Osorio, *et al.*, “The Substellar Mass Function in σ Orionis,” vol. 556, no. 2, pp. 830–836, Aug. 2001. DOI: 10.1086/321621. arXiv: astro-ph/0104097 [astro-ph].
- [118] R. B. Larson, “Towards understanding the stellar initial mass function,” vol. 256, pp. 641–646, Jun. 1992. DOI: 10.1093/mnras/256.3.641.
- [119] B. G. Elmegreen, “The Initial Stellar Mass Function from Random Sampling in a Turbulent Fractal Cloud,” vol. 486, no. 2, pp. 944–954, Sep. 1997. DOI: 10.1086/304562.

- [120] P. Mollière and C. Mordasini, “Deuterium burning in objects forming via the core accretion scenario. Brown dwarfs or planets?”, vol. 547, A105, A105, Nov. 2012. DOI: 10.1051/0004-6361/201219844. arXiv: 1210.0538 [astro-ph.EP].
- [121] A. Whitworth, M. R. Bate, Å. Nordlund, B. Reipurth, and H. Zinnecker, “The Formation of Brown Dwarfs: Theory,” in *Protostars and Planets V*, B. Reipurth, D. Jewitt, and K. Keil, Eds., Jan. 2007, p. 459.
- [122] G. W. Marcy and R. P. Butler, “Planets Orbiting Other Suns,” vol. 112, no. 768, pp. 137–140, Feb. 2000. DOI: 10.1086/316516.
- [123] D. Grether and C. H. Lineweaver, “How Dry is the Brown Dwarf Desert? Quantifying the Relative Number of Planets, Brown Dwarfs, and Stellar Companions around Nearby Sun-like Stars,” vol. 640, no. 2, pp. 1051–1062, Apr. 2006. DOI: 10.1086/500161. arXiv: astro-ph/0412356 [astro-ph].
- [124] J. A. Johnson, K. Apps, J. Z. Gazak, *et al.*, “LHS 6343 C: A Transiting Field Brown Dwarf Discovered by the Kepler Mission,” vol. 730, no. 2, 79, p. 79, Apr. 2011. DOI: 10.1088/0004-637X/730/2/79. arXiv: 1008.4141 [astro-ph.EP].
- [125] L. M. Close, B. Zuckerman, I. Song, *et al.*, “The Wide Brown Dwarf Binary Oph 1622-2405 and Discovery of a Wide, Low-Mass Binary in Ophiuchus (Oph 1623-2402): A New Class of Young Evaporating Wide Binaries?”, vol. 660, no. 2, pp. 1492–1506, May 2007. DOI: 10.1086/513417. arXiv: astro-ph/0608574 [astro-ph].
- [126] D. Lafrenière, R. Doyon, C. Marois, *et al.*, “The Gemini Deep Planet Survey,” vol. 670, no. 2, pp. 1367–1390, Dec. 2007. DOI: 10.1086/522826. arXiv: 0705.4290 [astro-ph].
- [127] L. Spezzi, G. Beccari, G. De Marchi, *et al.*, “Detection of Brown Dwarf Like Objects in the Core of NGC 3603,” vol. 731, no. 1, 1, p. 1, Apr. 2011. DOI: 10.1088/0004-637X/731/1/1. arXiv: 1101.4521 [astro-ph.SR].

- [128] I. S. McLean, M. R. McGovern, A. J. Burgasser, J. D. Kirkpatrick, L. Prato, and S. S. Kim, “The NIRSPEC Brown Dwarf Spectroscopic Survey. I. Low-Resolution Near-Infrared Spectra,” vol. 596, no. 1, pp. 561–586, Oct. 2003. DOI: 10.1086/377636. arXiv: astro-ph/0309257 [astro-ph].
- [129] H. K. Vedantham, J. R. Callingham, T. W. Shimwell, *et al.*, “Direct Radio Discovery of a Cold Brown Dwarf,” vol. 903, no. 2, L33, p. L33, Nov. 2020. DOI: 10.3847/2041-8213/abc256. arXiv: 2010.01915 [astro-ph.EP].
- [130] J. Sahlmann, D. Ségransan, D. Queloz, *et al.*, “Search for brown-dwarf companions of stars,” vol. 525, A95, A95, Jan. 2011. DOI: 10.1051/0004-6361/201015427. arXiv: 1009.5991 [astro-ph.EP].
- [131] P. Mróz, A. Udalski, J. Skowron, *et al.*, “No large population of unbound or wide-orbit Jupiter-mass planets,” vol. 548, no. 7666, pp. 183–186, Aug. 2017. DOI: 10.1038/nature23276. arXiv: 1707.07634 [astro-ph.EP].
- [132] P. Mróz, A. Udalski, J. Skowron, *et al.*, “Microlensing Optical Depth and Event Rate toward the Galactic Bulge from 8 yr of OGLE-IV Observations,” vol. 244, no. 2, 29, p. 29, Oct. 2019. DOI: 10.3847/1538-4365/ab426b. arXiv: 1906.02210 [astro-ph.SR].
- [133] P. Mróz, R. Poleski, A. Gould, *et al.*, “A Terrestrial-mass Rogue Planet Candidate Detected in the Shortest-timescale Microlensing Event,” vol. 903, no. 1, L11, p. L11, Nov. 2020. DOI: 10.3847/2041-8213/abffad. arXiv: 2009.12377 [astro-ph.EP].
- [134] H.-W. Kim, K.-H. Hwang, A. Gould, *et al.*, “KMT-2019-BLG-2073: Fourth Free-floating Planet Candidate with $\theta_E \lesssim 10 \mu\text{as}$,” vol. 162, no. 1, 15, p. 15, Jul. 2021. DOI: 10.3847/1538-3881/abfc4a. arXiv: 2007.06870 [astro-ph.EP].

- [135] Y.-H. Ryu, K.-H. Hwang, A. Gould, *et al.*, “Shortest Microlensing Event with a Bound Planet: KMT-2016-BLG-2605,” , vol. 162, no. 3, 96, p. 96, Sep. 2021. DOI: 10 . 3847 / 1538 - 3881 / ac062a. arXiv: 2104 . 07906 [astro-ph.EP].
- [136] N. Koshimoto and D. P. Bennett, “Evidence of Systematic Errors in Spitzer Microlens Parallax Measurements,” , vol. 160, no. 4, 177, p. 177, Oct. 2020. DOI: 10 . 3847 / 1538 - 3881 / abaf4e. arXiv: 1905 . 05794 [astro-ph.EP].
- [137] J. H. An, M. D. Albrow, J. -. Beaulieu, *et al.*, “First Microlens Mass Measurement: PLANET Photometry of EROS BLG-2000-5,” , vol. 572, no. 1, pp. 521–539, Jun. 2002. DOI: 10 . 1086 / 340191. arXiv: astro-ph/0110095 [astro-ph].
- [138] Ł. Wyrzykowski and I. Mandel, “Constraining the masses of microlensing black holes and the mass gap with Gaia DR2,” , vol. 636, A20, A20, Apr. 2020. DOI: 10 . 1051 / 0004 - 6361 / 201935842. arXiv: 1904.07789 [astro-ph.SR].
- [139] A. Gould, A. Udalski, B. Monard, *et al.*, “The Extreme Microlensing Event OGLE-2007-BLG-224: Terrestrial Parallax Observation of a Thick-Disk Brown Dwarf,” , vol. 698, no. 2, pp. L147–L151, Jun. 2009. DOI: 10 . 1088 / 0004 - 637X / 698 / 2 / L147. arXiv: 0904 . 0249 [astro-ph.GA].
- [140] V. Bozza, M. Dominik, N. J. Rattenbury, *et al.*, “OGLE-2008-BLG-510: first automated real-time detection of a weak microlensing anomaly - brown dwarf or stellar binary?,” , vol. 424, no. 2, pp. 902–918, Aug. 2012. DOI: 10 . 1111 / j . 1365 - 2966 . 2012 . 21233 . x. arXiv: 1203 . 1291 [astro-ph.EP].
- [141] C. Ranc, A. Cassan, M. D. Albrow, *et al.*, “MOA-2007-BLG-197: Exploring the brown dwarf desert,” , vol. 580, A125, A125, Aug. 2015. DOI: 10 . 1051 / 0004 - 6361 / 201525791. arXiv: 1505 . 06037 [astro-ph.EP].

- [142] J. -. Choi, C. Han, A. Udalski, *et al.*, “Microlensing Discovery of a Population of Very Tight, Very Low Mass Binary Brown Dwarfs,”, vol. 768, no. 2, 129, p. 129, May 2013. DOI: 10.1088/0004-637X/768/2/129. arXiv: 1302.4169 [astro-ph.SR].
- [143] M. D. Albrow, J. C. Yee, A. Udalski, *et al.*, “OGLE-2016-BLG-1266: A Probable Brown Dwarf/Planet Binary at the Deuterium Fusion Limit,”, vol. 858, no. 2, 107, p. 107, May 2018. DOI: 10.3847/1538-4357/aabf3f. arXiv: 1802.09563 [astro-ph.SR].
- [144] P. R. Wozniak, “Difference Image Analysis of the OGLE-II Bulge Data. I. The Method,”, vol. 50, pp. 421–450, Dec. 2000. DOI: 10.48550/arXiv.astro-ph/0012143. arXiv: astro-ph/0012143 [astro-ph].
- [145] A. B. Tomaney and A. P. S. Crotts, “Expanding the Realm of Microlensing Surveys with Difference Image Photometry,”, vol. 112, p. 2872, Dec. 1996. DOI: 10.1086/118228. arXiv: astro-ph/9610066 [astro-ph].
- [146] C. Alard and R. H. Lupton, “A Method for Optimal Image Subtraction,”, vol. 503, no. 1, pp. 325–331, Aug. 1998. DOI: 10.1086/305984. arXiv: astro-ph/9712287 [astro-ph].
- [147] C. Alard, “Image subtraction using a space-varying kernel,”, vol. 144, pp. 363–370, Jun. 2000. DOI: 10.1051/aas:2000214.
- [148] I. A. Bond, D. P. Bennett, T. Sumi, *et al.*, “The lowest mass ratio planetary microlens: OGLE 2016-BLG-1195Lb,”, vol. 469, no. 2, pp. 2434–2440, Aug. 2017. DOI: 10.1093/mnras/stx1049. arXiv: 1703.08639 [astro-ph.EP].
- [149] A. Herald, A. Udalski, V. Bozza, *et al.*, “Precision measurement of a brown dwarf mass in a binary system in the microlensing event. OGLE-2019-BLG-0033/MOA-2019-BLG-035,”, vol. 663, A100, A100, Jul. 2022. DOI: 10.1051/0004-6361/202243490. arXiv: 2203.04034 [astro-ph.SR].

- [150] P. L. Schechter, M. Mateo, and A. Saha, “DoPHOT, A CCD Photometry Program: Description and Tests,” vol. 105, p. 1342, Nov. 1993. DOI: 10.1086/133316.
- [151] W. Zang, M. T. Penny, W. Zhu, *et al.*, “Measurement of Source Star Colors with the K2C9-CFHT Multi-color Microlensing Survey,” vol. 130, no. 992, p. 104401, Oct. 2018. DOI: 10.1088/1538-3873/aadcd3. arXiv: 1803.09184 [astro-ph.EP].
- [152] M. Dominik, U. G. Jørgensen, N. J. Rattenbury, *et al.*, “Realisation of a fully-deterministic microlensing observing strategy for inferring planet populations,” *Astronomische Nachrichten*, vol. 331, no. 7, p. 671, Jul. 2010. DOI: 10.1002/asna.201011400.
- [153] J. Skottfelt, D. M. Bramich, M. Hundertmark, *et al.*, “The two-colour EMCCD instrument for the Danish 1.54 m telescope and SONG,” vol. 574, A54, A54, Feb. 2015. DOI: 10.1051/0004-6361/201425260. arXiv: 1411.7401 [astro-ph.IM].
- [154] D. M. Bramich, “A new algorithm for difference image analysis,” vol. 386, no. 1, pp. L77–L81, May 2008. DOI: 10.1111/j.1745-3933.2008.00464.x. arXiv: 0802.1273 [astro-ph].
- [155] D. M. Bramich, K. Horne, M. D. Albrow, *et al.*, “Difference image analysis: extension to a spatially varying photometric scale factor and other considerations,” vol. 428, no. 3, pp. 2275–2289, Jan. 2013. DOI: 10.1093/mnras/sts184. arXiv: 1210.2926 [astro-ph.IM].
- [156] A. Gould and J. C. Yee, “Cheap Space-based Microlens Parallaxes for High-magnification Events,” vol. 755, no. 1, L17, p. L17, Aug. 2012. DOI: 10.1088/2041-8205/755/1/L17. arXiv: 1205.5801 [astro-ph.EP].
- [157] S. Refsdal, “On the possibility of determining the distances and masses of stars from the gravitational lens effect,” vol. 134, p. 315, Jan. 1966. DOI: 10.1093/mnras/134.3.315.

- [158] V. Batista, A. Gould, S. Dieters, *et al.*, “MOA-2009-BLG-387Lb: a massive planet orbiting an M dwarf,” vol. 529, A102, A102, May 2011. DOI: 10.1051/0004-6361/201016111. arXiv: 1102.0558 [astro-ph.EP].
- [159] N. Miyake, T. Sumi, S. Dong, *et al.*, “A Sub-Saturn Mass Planet, MOA-2009-BLG-319Lb,” vol. 728, no. 2, 120, p. 120, Feb. 2011. DOI: 10.1088/0004-637X/728/2/120. arXiv: 1010.1809 [astro-ph.EP].
- [160] I.-G. Shin, J. C. Yee, K.-H. Hwang, *et al.*, “OGLE-2016-BLG-1093Lb: A Sub-Jupiter-mass Spitzer Planet Located in the Galactic Bulge,” vol. 163, no. 6, 254, p. 254, Jun. 2022. DOI: 10.3847/1538-3881/ac6513. arXiv: 2201.04312 [astro-ph.EP].
- [161] J. C. Yee, L. -. Hung, I. A. Bond, *et al.*, “MOA-2010-BLG-311: A Planetary Candidate below the Threshold of Reliable Detection,” vol. 769, no. 1, 77, p. 77, May 2013. DOI: 10.1088/0004-637X/769/1/77. arXiv: 1210.6041 [astro-ph.EP].
- [162] Gaia Collaboration, A. G. A. Brown, A. Vallenari, *et al.*, “Gaia Early Data Release 3. Summary of the contents and survey properties,” vol. 649, A1, A1, May 2021. DOI: 10.1051/0004-6361/202039657. arXiv: 2012.01533 [astro-ph.GA].
- [163] A. Claret and S. Bloemen, “Gravity and limb-darkening coefficients for the Kepler, CoRoT, Spitzer, uvby, UBVRIJHK, and Sloan photometric systems,” vol. 529, A75, A75, May 2011. DOI: 10.1051/0004-6361/201116451.
- [164] G. F. Benedict, T. J. Henry, O. G. Franz, *et al.*, “The Solar Neighborhood. XXXVII: The Mass-Luminosity Relation for Main-sequence M Dwarfs,” vol. 152, no. 5, 141, p. 141, Nov. 2016. DOI: 10.3847/0004-6256/152/5/141. arXiv: 1608.04775 [astro-ph.SR].
- [165] O. Golubov, A. Just, O. Bienaymé, *et al.*, “The asymmetric drift, the local standard of rest, and implications from RAVE data,” vol. 557,

- A92, A92, Sep. 2013. DOI: 10.1051/0004-6361/201321559. arXiv: 1307.6073 [astro-ph.GA].
- [166] I. -. Shin, C. Han, A. Gould, *et al.*, “Microlensing Binaries with Candidate Brown Dwarf Companions,” vol. 760, no. 2, 116, p. 116, Dec. 2012. DOI: 10.1088/0004-637X/760/2/116. arXiv: 1208.2323 [astro-ph.SR].
- [167] Y. Shvartzvald, Z. Li, A. Udalski, *et al.*, “The First Simultaneous Microlensing Observations by Two Space Telescopes: Spitzer and Swift Reveal a Brown Dwarf in Event OGLE-2015-BLG-1319,” vol. 831, no. 2, 183, p. 183, Nov. 2016. DOI: 10.3847/0004-637X/831/2/183. arXiv: 1606.02292 [astro-ph.EP].
- [168] T. Bensby, S. Feltzing, J. A. Johnson, *et al.*, “Chemical evolution of the Galactic bulge as traced by microlensed dwarf and subgiant stars. II. Ages, metallicities, detailed elemental abundances, and connections to the Galactic thick disc,” vol. 512, A41, A41, Mar. 2010. DOI: 10.1051/0004-6361/200913744. arXiv: 0911.5076 [astro-ph.GA].
- [169] T. Bensby, A. Gould, M. Asplund, *et al.*, “Chemical evolution of the Galactic bulge as traced by microlensed dwarf and subgiant stars. VIII. Carbon and oxygen,” vol. 655, A117, A117, Nov. 2021. DOI: 10.1051/0004-6361/202141592. arXiv: 2106.11314 [astro-ph.GA].
- [170] A. Bhattacharya, J. -. Beaulieu, D. P. Bennett, *et al.*, “WFIRST Exoplanet Mass-measurement Method Finds a Planetary Mass of $39 \pm 8 M_{\oplus}$ for OGLE-2012-BLG-0950Lb,” vol. 156, no. 6, 289, p. 289, Dec. 2018. DOI: 10.3847/1538-3881/aaed46. arXiv: 1809.02654 [astro-ph.EP].
- [171] A. M. Meisner, J. K. Faherty, J. D. Kirkpatrick, *et al.*, “Spitzer Follow-up of Extremely Cold Brown Dwarfs Discovered by the Backyard Worlds: Planet 9 Citizen Science Project,” vol. 899, no. 2, 123, p. 123, Aug. 2020. DOI: 10.3847/1538-4357/aba633. arXiv: 2008.06396 [astro-ph.SR].

- [172] N. Miret-Roig, H. Bouy, S. N. Raymond, *et al.*, “A rich population of free-floating planets in the Upper Scorpius young stellar association,” *Nature Astronomy*, vol. 6, pp. 89–97, Feb. 2022. DOI: 10.1038/s41550-021-01513-x. arXiv: 2112.11999 [astro-ph.EP].
- [173] J. Ryan R. E. and I. N. Reid, “The Surface Densities of Disk Brown Dwarfs in JWST Surveys,” , vol. 151, no. 4, 92, p. 92, Apr. 2016. DOI: 10.3847/0004-6256/151/4/92. arXiv: 1510.05019 [astro-ph.GA].
- [174] S. Trippe, R. Davies, F. Eisenhauer, N. M. Förster Schreiber, T. K. Fritz, and R. Genzel, “High-precision astrometry with MICADO at the European Extremely Large Telescope,” , vol. 402, no. 2, pp. 1126–1140, Feb. 2010. DOI: 10.1111/j.1365-2966.2009.15940.x. arXiv: 0910.5114 [astro-ph.IM].
- [175] J. Klüter, U. Bastian, and J. Wambsganss, “Expectations on mass determination using astrometric microlensing by Gaia,” , vol. 640, A83, A83, Aug. 2020. DOI: 10.1051/0004-6361/201937061. arXiv: 1911.02584 [astro-ph.IM].
- [176] N. Ihanec, M. Gromadzki, L. Wyrzykowski, and D. A. H. Buckley, “SALT spectroscopic classification of microlensing event candidate Gaia20bof,” *The Astronomer’s Telegram*, vol. 13797, p. 1, Jun. 2020.
- [177] L. Lindegren, “Re-normalising the astrometric chi-square in Gaia DR2,” Technical Note, GAIA-C3-TN-LU-LL-124, Aug. 2018. [Online]. Available: http://www.rssd.esa.int/doc_fetch.php?id=3757412.
- [178] M. Riello, F. De Angeli, D. W. Evans, *et al.*, “Gaia Early Data Release 3. Photometric content and validation,” , vol. 649, A3, A3, May 2021. DOI: 10.1051/0004-6361/202039587. arXiv: 2012.01916 [astro-ph.IM].
- [179] F. Xia, S. Ren, and Y. Fu, “The empirical mass-luminosity relation for low mass stars,” *Astrophysics and Space Science*, vol. 314, pp. 51–58, 2008.

- [180] L. Capitanio, R. Lallement, J. L. Vergely, M. Elyajouri, and A. Monreal-Ibero, “Three-dimensional mapping of the local interstellar medium with composite data,” vol. 606, A65, A65, Oct. 2017. DOI: 10.1051/0004-6361/201730831. arXiv: 1706.07711 [astro-ph.GA].
- [181] T. S. Boyajian, G. Van Belle, and K. Von Braun, “Stellar diameters and temperatures. iv. predicting stellar angular diameters,” *The Astronomical Journal*, vol. 147, no. 3, p. 47, 2014.
- [182] T. G. Barnes, D. S. Evans, and T. J. Moffett, “Stellar angular diameters and visual surface brightnesses - III. An improved definition of the relationship.,” vol. 183, pp. 285–304, May 1978. DOI: 10.1093/mnras/183.3.285.
- [183] L. Girardi, A. Bressan, G. Bertelli, and C. Chiosi, “Evolutionary tracks and isochrones for low- and intermediate-mass stars: From 0.15 to 7 M_{sun} , and from $Z=0.0004$ to 0.03,” vol. 141, pp. 371–383, Feb. 2000. DOI: 10.1051/aas:2000126. arXiv: astro-ph/9910164 [astro-ph].
- [184] J. R. A. Davenport, A. A. West, C. K. Matthiesen, M. Schmieding, and A. Kobelski, “Sloan/Johnson-Cousins/2MASS Color Transformations for Cool Stars,” vol. 118, no. 850, pp. 1679–1684, Dec. 2006. DOI: 10.1086/510501. arXiv: astro-ph/0611087 [astro-ph].

LIST OF TABLES

3.1	Parameters for all models considered for MOA-2006-BLG-074, Credits [100]	61
3.2	Physical parameters for model 1 <i>L2SX</i> , Credits [100]	72
4.1	Parameters of the best microlensing models found with ground-only data. Credits [149]	82
4.2	Comparison of parallax π_E and χ^2 for our four models if Spitzer data are included or excluded. Credits [149]	88
4.3	Microlensing parameters for model A including Spitzer data. Credits [149]	89
4.4	Parameters of the binary lens system. Credits [149]	91
4.5	Binary microlensing events with relative error less than 10% for the BD mass. The suffixes A and B in the names indicate that the BD is the primary or the secondary component in the lens. No suffix means that the BD lens was isolated. Credits [149]	94
5.1	Summary of photometric observations. Due to the low number of observations, the LSC datasets were not used in the modeling. This is mainly due to the COVID-19 pandemic and the LCO site at La Silla remains closed longer than other sites. Courtesy of Etienne Bachelet, (Bachelet et al. 2023, in prep.)	99

5.2	Best models from the modeling of the lightcurves. Courtesy of Etienne Bachelet, (Bachelet et al. 2023, in prep.)	101
5.3	Parameters of the source from spectroscopic analysis. Courtesy of Etienne Bachelet, (Bachelet et al. 2023, in prep.)	104
5.4	Parameters of the best models. Rota et al. 2023 in prep.	106
5.5	Magnitudes of baseline (source) and blend (lens flux for our assumption) of the best models for each telescope. Rota et al. 2023 in prep.	109
5.6	Physical parameters of lens and source for the best model. Rota et al. 2023 in prep.	112

LIST OF FIGURES

1.1	Image of the lensed quasar 0957 +561. The Twin Quasar, as renamed later, was the first proof of gravitational lensing applied to distant galaxies. The lens is the galaxy YGKOW G1 with a distance of 4 billion light-years from Earth. The quasar is distant 9 billion light-years. Credit image: ESA/Hubble & NASA	8
1.2	Picture of a gravitational microlensing event with a distant source (the star) whose signal directed to an observer (the Earth) is amplified by a lens. Credit image: Enciclopedia Britannica, Inc	9
1.3	Geometric configuration of a gravitational lensing event with a point-lens. Credit image: Principles of Gravitational Lensing, Keeton, [9]	11
1.4	Geometric configuration of a single lens event. The black circle is the Einstein ring. Considering a frame in which the lens is fixed at the center of the plot with a black dot, the source trajectory is represented in five different configuration. Credit image: Microlensing Searches for Exoplanets, Tsapras, [10] . . .	12
1.5	Magnification as a function of time for different values of u_0 . The lower the value of u_0 the higher the peak will be. Credit image: Microlensing Surveys for Exoplanets, Gaudi, [7]	14

1.6	Lightcurve computation with finite source effect $\rho_* = 0.1$ (in blue) and without (in red). Credit image: Introduction to Gravitational Lensing, Meneghetti, [9]	17
1.7	Boundaries between the three different topologies of caustics in the binary lens in the parameter space (s, q) . Also shown are three examples: the close configuration is obtained with $s = 0.75$, the intermediate with $s = 1$, the wide with $s = 1.5$. For all the cases $q = 10^{-2}$. Credit image: Microlensing Searches for Exoplanets, Tsapras, [10]	20
1.8	Schematization of three different planetary microlensing events: on the top (a,b,c) a wide configuration, with $s = 1.3$ and $q = 0.003$ where the source trajectory crosses the planetary caustic. In the middle we have (d,e,f) a resonant configuration with $s = 1.0$ and $q = 0.003$. In the bottom (g,h,i) another wide configuration where the source crosses the central caustic (also in this case $s = 1.3$ and $q = 0.003$) Credit image: Microlensing Surveys for Exoplanets, Gaudi, [7]	22
1.9	Lightcurve of a microlensing event with parallax effect. The dashed curve represents the static configuration while the fitted curve includes the parallax. Credit image: Rhavar, 2015, [8]	23
1.10	Lightcurve of a microlensing event detected by satellite (Spitzer) and Earth telescope (OGLE): the two lightcurve are different since u_0 and t_0 are not the same. The difference yields the parallax vector π_E . Credit image: Yee et al, 2015 [18]	24
1.11	Caustic configuration of microlensing event OGLE-2015-BLG-0479. The temporal evolution of the resonant caustic due to the orbital motion of the binary system can be noted. The blue and red line indicate the source trajectory seen by ground telescope and satellite respectively. Credit image: Han et al, 2016 [19]	25

1.12	Lightcurve of microlensing event MACHO 96-LMC-2 described by a Xallarap model (continuous line) Credit image: Alcock et al, 2001, [23]	27
1.13	The four combinations of the source trajectory seen from satellite and Earth Credit image: Methods of detecting exoplanets, Bozza et al.[30]	30
1.14	Mass versus semi-major axis of all exoplanets detected up to the 17 December 2022. We can see how all the techniques to discover exoplanets are complementary each other. We can note how most exoplanets detected by microlensing lie beyond the snow line, represented by the blue vertical line. Credit image: Nasa Exoplanet Archive	31
2.1	Las Campanas Observatory, Chile Credit image: OGLE collaboration	34
2.2	OGLE fields in the sky map. Credit image: OGLE collaboration	35
2.3	MOA telescope at the top of Mount John Credit image: MOA collaboration	36
2.4	The 22 target fields observed by MOA surveys with the discovery of approximately 6000 microlensing events. Credit image: MOA collaboration	37
2.5	The 1.6 m telescope located in South Africa for the KMTNet collaboration. Credit image: KMTNet collaboration	38
2.6	Fields observed by KMTNet in 2016, color-coded by cadence. Credit image: KMTNet collaboration, Matthew Penny	39
2.7	(Left) The Spitzer telescope in the Jet Propulsion Laboratory. (Center) Artistic representation of Kepler satellite. (Right) Artistic representation of Gaia satellite. Credit images: NASA/ESA	40

2.8	Prediction of exoplanets discovered by Roman telescope compared with the Kepler satellite Credit image: NASA's Goddard Space Flight Center, adapted from Penny et al. (2019) [51]	41
2.9	1.54 m Danish Telescope at La Silla in Chile. Credit image: Paolo Rota	43
3.1	Light curve of MOA-2006-BLG-074 with the best model 1L2SX. We also show the residuals for the single-lens model 1L, the static binary lens model 2L, the binary lens model including orbital motion 2LO, the single lens binary source model 1L2SX, Credits [100]	62
3.2	Zoom of the light curve of MOA-2006-BLG-074 with the best model. We also show the residuals for the single-lens model 1L, the static binary lens model 2L, the binary lens model including orbital motion 2LO, the single lens binary source model 1L2SX, Credits [100]	63
3.3	Caustic configuration for the binary orbital model $2LO$ presented in Table 3.1, with the source moving along the straight line from left to right. The green color refers to time t_0 , while other colors represent the source and caustics in time-steps of 5 days, Credits [100]	65
3.4	Trajectory of the primary source (black) and secondary source(blue) for the best model with one lens and two sources in Table 3.1 with a choice of the mass ratio $q_s = 0.33$. We have marked the positions of the sources at $t_0 - t_E, t_0, t_0 + t_E$, Credits [100]	65

3.5	Color magnitude diagram (CMD) of the stars in the field of MOA-2006-BLG-074. The red dot shows the position of the red clump. The green dot represents the source star and the blue dot shows the blend position for model <i>1L2SX</i> . The empty circles represent the same objects for the <i>2LO</i> case, Credits [100]	67
3.6	Allowed regions (in blue) in the plane $D_L(\text{kpc}) - \text{Log } M/M_\odot$ at 68% and 95% CL for the <i>2LO</i> model. In red, the regions allowed by the Keplerian constraint, Credits [100]	69
3.7	Allowed region in the plane $D_L(\text{kpc}) - \text{Log } M/M_\odot$ at 68% and 95% CL for model <i>1L2SX</i> , Credits [100]	70
3.8	Distributions of the parameter $\log q_s$. The red histogram is obtained with a flat prior, while the blue one is the same distribution where each point in the Markov chain is weighted by the prior $P(q_s, \xi, \omega)$ in Eq. (3.7), Credits [100]	71
4.1	Light curve of the event OGLE-2019-BLG-0033 showing all observations from different telescopes as described in the text. The black curve is the best microlensing model for ground observers, and the red curve is the best model for Spitzer observations, as described in Section 3. In the bottom panel, we show the residuals from several models: best model including the parallax and orbital motion, best model with parallax without orbital motion, and best static model without parallax., Credits [149]	77
4.2	Zoom on the double-peak region of the light curve. The color coding for the observations is the same as in Figure 4.1, Credits [149]	79
4.3	Caustics of the four binary lens models examined in our analysis, with the best model labeled as A. The source trajectories are also shown as seen from Earth observatories (black) and from Spitzer (red), Credits [149]	80

4.4	Zoom-in on the caustic of the best binary lens model with the source trajectory. The size of the source is shown by the gray disk, Credits [149]	81
4.5	Color-magnitude diagrams using different resources. Top panel: CMD of stars in the 2' field of the event OGLE-2019-BLG 0033 built from MOA observations. The red dot corresponds to the center of the red clump and the green dot shows the position of the source. Bottom panel: CMD built from I-band observations from OGLE and L-band measurements from Spitzer. Credits [149]	86
4.6	Components of the parallax vector as found by the fit excluding Spitzer (in gray) or including Spitzer data (in cyan). Confidence levels at 68% and 95% are given. Credits [149]	87
5.1	Lightcurve with residuals of the best model (Wide+) for Gaia20bof100	
5.2	The two spectra from SALT (black) and XShooter (red), as well as several models from the MCMC exploration, are visible. The gray vertical lines indicates absorption bands, where the data were not used for the modeling. Courtesy of Etienne Bachelet, (Bachelet et al. 2023, in prep.)	102
5.3	(Left) PARSEC stellar isochrones for 9, 9.5 and 10 Gyr with a fix metallicity of -0.75. The source is most likely an old subgiant. (Middle) Source angular radius based on the spectral models as a function of the source distance and age (color-coded). (Right) Source distance based on the Gaia source measurements from the model ($G_s \sim 16$ mag) and the extinction estimated from the spectral modeling. Black dash lines indicates the 1- σ confidence region from the parallax measurement of Gaia. Courtesy of Etienne Bachelet, (Bachelet et al. 2023, in prep.)	103

5.4	(Left) The source trajectories (blue), caustics (red) and critical curves (black) for the eight models for Gaia20bof. Note that the center of mass of the lenses is kept fixed at (0,0). The microlensing astrometric deflections in right ascension (Middle) and in declination (Right) versus time are also displayed. The color indicates the observed Gaia G magnitude. Courtesy of Etienne Bachelet, (Bachelet et al. 2023, in prep.)	104
5.5	Lightcurve with residuals of the best model (called LOCcloseR) for the microlensing event Gaia21blx. (Rota et al. 2023 in prep.)	107
5.6	Caustic configuration for all the models. On the top we have the LOCclose on the left (R) while on the right there is the LOCcloseR (CR). On the bottom on the left we have the LOWide model (W) and then on the right the LOWideR model (WR). (Rota et al. 2023 in prep.)	108
5.7	Plot of the three mass-distance functions for the LOCcloseR model. In blue we have the constraint from the microlensing and Gaia parallax. In red the constraint from the lens flux where mass-luminosity relations for low mass star are used. In green the constraint obtained from the finite source effects and the angular radius of the source. (Rota et al. 2023 in prep.) . . .	111
5.8	Astrometry simulation for the LOCcloseR model. (Rota et al. 2023 in prep.). The blue curve is the source trajectory in a frame in which the lenses are fixed. The orange curve shows the centroid trajectory. The two brown disk are the two lenses and the black points are the Gaia points. Rota et al. 2023 in prep. . .	112

RINGRAZIAMENTI

Siamo arrivati alla parte più letta della tesi, quella dei ringraziamenti. Come sapranno coloro che hanno letto i ringraziamenti della mia laurea triennale e magistrale non sono bravo a scriverli, per cui perdonatemi se non sono un granchè.

Tante sono le persone che in un modo o nell'altro mi hanno aiutato, supportato e mi sono state vicine durante questi anni di dottorato e mi sento in dovere di ringraziarle, sperando di non dimenticare nessuno.

Non posso che iniziare i ringraziamenti partendo dalla mia famiglia, i miei genitori e mio fratello, che mi hanno sempre supportato in ogni modo e mi sono sempre stati vicini.

Ovviamente persona fondamentale per la mia crescita e formazione è il prof. Valerio Bozza che mi ha permesso di rendere la mia passione anche un lavoro aiutandomi e fornendomi tutto il supporto necessario. E' soprattutto grazie a lui se ho avuto la possibilità di andare a La Silla a lavorare con un telescopio sulle Ande e realizzare così uno dei miei sogni più grandi. Grazie Valerio.

Grazie a Giuseppe D'Ago, senza di te sarei stato completamente sperduto durante le mie due settimane passate in Cile, hai avuto la pazienza di togliermi tutti i dubbi e risolvere molti dei problemi che ho avuto prima e durante il viaggio, per me ha significato tanto. Ti aspetto ancora per una birra da

prendere insieme!

Durante questi tre anni di dottorato ho avuto modo di conoscere persone nuove con cui ho instaurato bellissime amicizie. Tra queste quella con Silvia è tra le più significative, amica e collega di dottorato con cui ho trascorso questi tre anni. Grazie Silvia =) Grazie al Centro Astronomico Neil Armstrong Salerno, associazione di astrofili con cui da oltre 10 anni condivido la mia passione per il cielo. Trovare tante persone unite dalla stessa passione con cui è nata una splendida amicizia come Peppino, Nando, Giovanni, Vito, Vincenzo, Alberto, Vincenzo, Lucio è qualcosa di meraviglioso e di unico. Le serate astronomiche passate ad osservare le meraviglie del cielo, le trasferte nei posti più assurdi, i bellissimi eventi fatti e tanto altro ancora hanno dato e continueranno a darmi tanto in questo percorso che sto facendo.

In particolare un grazie va a Biagio, da anni mia spalla imprescindibile, amico e fratello, una persona che vorrei sempre avere con me e con cui condivido da tanti anni studio, passione e tanto altro ancora. Sei una persona splendida e sono sempre più felice di essere tuo amico. Ricordati che abbiamo un albero di Natale da fare insieme.

Ad Umberto e Raffaele, le grigliate con voi hanno un altro sapore, e a Marco, i tuoi consigli e suggerimenti mi hanno aiutato tanto in questo percorso. Grazie di cuore a voi.

Grazie ai ragazzi della scuola estiva, Enver, Sara, Loredana, Vincenzo, Michele, Aniello e Gianluca, è stata una bellissima esperienza. Ma grazie anche agli amici dell'università e del laboratorio Alfonso, Marta (auguri Marta), Enzo, Enrico, Luciano, Raoul, Vito, Fabio, Marianna, Kimberly, Matteo, Lidia, Pascal, Antonio, Debora, Daniele, Vito, Luciana, Piero, Pia. Sapere che venendo all'università trovo qualcuno di voi è sempre un piacere. E se ho dimenticato qualcuno mi perdoni, siete tanti, ma mai abbastanza!

A Mario e Sara, due persone splendide a cui voglio un bene incredibile, grazie anche a voi. Ai compagni di calcetto, grigliate e karaoke, Ramses, Tony, Salvatore, Valerio ed Alberto. Grazie per i bellissimi momenti di goliardia passati insieme in questi anni, e so già che la vostra risposta sarà "grazie a

lei!". Grazie al mio omonimo Paolo, compagno di bevute e di avventure che mi ha insegnato un metodo alternativo per caricare l'acqua nel radiatore se non hai acqua a disposizione.

Anche se la nostra amicizia era un qualcosa di assodato negli ultimi tempi ho scoperto in te una persona su cui posso sempre contare e su cui posso fare cieco affidamento. Grazie Ludovico, sei un amico fantastico e sono contento di averti conosciuto.

Grazie a Marta, che ormai è come una sorella per me e che nonostante non la veda quotidianamente come prima non fa sentire pesante questa distanza. Abbiamo passato tantissimi bei momenti insieme e sono sicuro che tanti altri ancora ne vivremo. Oltretutto senza di te perdono anche di entusiasmo :D Grazie ad Ines, condividiamo insieme tanti anni di università ma soprattutto la passione per l'astrofisica che mi ha fornito la possibilità di farti anche da "co-relatore" per la tua tesi di laurea e che ci farà pubblicare il nostro primo ma, spero, non unico lavoro insieme. Sarà strano non vederti più come prima all'università ma è giusto che tu percorra la tua strada: la cosa importante è far sì che le nostre strade continuino ad incrociarsi sempre =)

Grazie a Cristina, insieme abbiamo fatto triennale, magistrale ed anche il dottorato. Siamo cresciuti insieme e ci siamo sempre supportati in ogni modo senza mai darci per vinti. Sono felice di aver fatto questo percorso insieme a te, e spero che tu possa sopportarmi in dipartimento ancora per un pò. La tua è una di quelle amicizie rare e preziose che custodisco gelosamente.

Durante questi anni ho imparato anche a vivere da fuorisede qui a Fisciano. Per puro caso ho trovato una stanza che un ragazzo, stava lasciando e così ne ho approfittato subito. All'inizio avevo il timore di trovare persone terribili ma col tempo mi sono reso conto di aver condiviso la casa con ragazzi fantastici e se dovessi tornare indietro sceglierei esattamente la stessa casa. Tramite i miei coinquilini ho conosciuto tantissime belle persone con cui condividiamo ancora oggi tante esperienze. Tra questi in particolare c'è Elpidio, che è anche il ragazzo a cui ho preso il posto in questa casa a cui va un doppio grazie! Ma tra tutti loro una menzione speciale va ad Egidio che

nel giro di pochi anni è diventata una persona fondamentale per me con cui ho condiviso tante bellissime esperienze (e soprattutto mangiate!) e con cui sono sicuro vivrò tantissime avventure. Grazie Egidio, non vedo l'ora di incontrare persone strambe e assurde insieme a te.

Agli amici di sempre, che conosco da una vita intera, non servono le parole per descrivere quanto vi voglio bene e qualunque sia la distanza so che ci sarete sempre. Grazie a Luigi (Kaaaaaaaaaaaaarlllll), Lorenzo, Alfredo, Francesco, Michele, Francesca, Valdemiro, Gianmario.

Menzione speciale per Mimmo, mio migliore amico da sempre e fratello da una vita. Mi hai sempre sostenuto, supportato, aiutato nonostante la grande distanza. E ogni volta che c'è occasione riusciamo sempre a vederci e ciò mi rende felicissimo. Grazie di esserci sempre.

Grazie di cuore alla mia colonna, spalla, fidanzata Ylenia. A te devo tanto, mi hai sostenuto nei miei momenti più bui e cazziato quando necessario (ogni tanto ci vogliono). Quando pensavo di non riuscire ad andare avanti mi hai sempre aiutato. Il completamento di questo percorso lo devo soprattutto a te e l'aver coronato il nostro piccolo sogno di andare a vivere insieme durante il dottorato è stato qualcosa di meraviglioso. Sono felicissimo di poterti avere al mio fianco e di poter contare sempre su di te.

E infine voglio ringraziare il me bambino, senza di lui ora non sarei qui e non avrei realizzato due dei miei più grandi sogni, ossia quello di poter ammirare il cielo più bello visibile dalla Terra, lavorando ad un telescopio e lavorare nel campo dell'astrofisica. L'esperienza avuta a La Silla è qualcosa di difficilmente descrivibile che porterò con me per tutta la vita.

Grazie piccolo Paolo!